

**SYNTHESIS AND CONTROL OF EXCITON
DYNAMICS IN CdTe, CdTe/CdS AND $Zn_xCd_{1-x}Te$
COLLOIDAL NANOCRYSTALS**

**A Thesis Submitted to
the Graduate School of Engineering and Sciences of
İzmir Institute of Technology
in Partial Fulfillment of the Requirements for the Degree of**

DOCTOR OF PHILOSOPHY

in Chemistry

**by
Leyla ERAL DOĞAN**

**December 2012
İZMİR**

We approve the thesis of **Leyla ERAL DOĞAN**

Examining Committee Members:

Prof. Dr. Serdar ÖZÇELİK
Department of Chemistry, İzmir Institute of Technology

Prof. Dr. Muhsin ÇİFTÇİOĞLU
Department of Chemical Engineering, İzmir Institute of Technology

Assoc. Prof. Dr. Mustafa M. DEMİR
Department of Chemistry, İzmir Institute of Technology

Assoc. Prof. Dr. Yusuf SELAMET
Department of Physics, İzmir Institute of Technology

Assoc. Prof. Dr. Canan VARLIKLI
Institute of Solar Energy, Ege University

20 December 2012

Prof. Dr. Serdar ÖZÇELİK
Supervisor, Department of Chemistry
İzmir Institute of Technology

Prof. Dr. Durmuş ÖZDEMİR
Head of the Department of Chemistry

Prof. Dr. R. Tuğrul SENGER
Dean of the Graduate School of
Engineering and Sciences

ACKNOWLEDGEMENTS

It is my great pleasure to have chance to express my gratitude to all people who have helped me or encouraged me through my PhD studies.

I am grateful to my supervisor Prof. Dr. Serdar Özçelik, for his invaluable guidance, thoughtful advice, encouragement and support through my PhD program.

Sincere appreciations are given to Prof. Dr. Muhsin Çiftçiöđlu and Assoc. Dr. Mustafa M. Demir for their insightful guidance, discussions and contributions to my research study.

I am also grateful to my lab mates for their care, their kind helps and friendships during the whole period of my study. My sincere gratitude also goes to my special friends in İYTE who have helped me through the years.

I would also thank İYTE Research Foundation and İYTE MAM Researchers for their help in analysis.

Finally, I would like to thank my parents, my husband, my brother as well as my relatives for their unconditional love, support, patience, encouragement, understanding and sacrifice during this study.

ABSTRACT

SYNTHESIS AND CONTROL OF EXCITON DYNAMICS IN CdTe, CdTe/CdS AND $Zn_xCd_{1-x}Te$ COLLOIDAL NANOCRYSTALS

The aim of this study is to synthesize cadmium-based semiconductor colloidal nanocrystals and to control their exciton dynamics by tuning the size and composition of the nanocrystals (NCs). CdTe, CdTe/CdS binary, and $Zn_xCd_{1-x}Te$ ternary semiconductor NCs are prepared by wet chemistry. The reactions are thoroughly optimized to enhance the optical properties. The optical properties of CdTe and CdTe/CdS are tuned by the size of the NCs by adjusting the reaction (the growth) time. Coating CdTe NCs with CdS layer enhances the photoluminescence quantum yields up to 45%. $Zn_xCd_{1-x}Te$ ternary nanoalloys were synthesized by varying the initial mole ratios of metals ($Zn/Zn+Cd$) and the growth time. The size and the composition-tunable $Zn_xCd_{1-x}Te$ nanoalloys exhibit highly luminescent optical properties. When the amount of initial Zn precursor is low, the nanoalloys have Cd-rich and Zn-poor internal crystal structure. However, at higher amount of Zn precursor, the nanoalloys have Zn-rich and Cd-poor core exhibiting gradient composition.

The exciton interactions and dynamics are investigated as a function of the size of CdTe/CdS, and the composition and the size of $Zn_xCd_{1-x}Te$ nanoalloys. The exciton interaction yields amplification in the output signal at the threshold of 10^{15} photon/cm²s per laser pulse. The exciton lifetimes are in the range of picoseconds to nanoseconds. The decay associated spectra are affected by the laser power, size and composition of the NCs. As the laser power increases new excitonic states are created especially in $Zn_xCd_{1-x}Te$ nanoalloys. Multiexcitons were created in the NCs depending on the laser power. Small NCs exhibit stronger exciton-exciton interactions under high laser power compared to larger NCs. However larger NCs have lesser exciton density, therefore reducing the exciton-exciton interactions.

ÖZET

CdTe, CdTe/CdS VE $Zn_xCd_{1-x}Te$ KOLLOİDAL NANOKRİSTALLERİNİN SENTEZİ VE EKŞİTON DİNAMİKLERİNİN KONTROLÜ

Bu çalışmanın amacı kadmiyum bazlı yarıiletken kolloidal nanokristaller sentezlemek ve nanokristallerin büyüklük ve kompozisyonunun ayarlanması suretiyle eksiton dinamiğini kontrol etmektir.

CdTe, CdTe/CdS ikili ve $Zn_xCd_{1-x}Te$ üçlü yarıiletken nanokristaller ıslak kimya yöntemi ile sentezlenmiştir ve nanokristallerin optik özelliklerini artırmak için reaksiyon koşulları optimize edilmiştir. CdTe ve CdTe/CdS nanokristallerinin büyüklükleri reaksiyon zamanı ayarlanarak kontrol edilmiş ve parçacık büyüklüğüne bağlı olarak optik özellikleri düzenlenmiştir. CdTe nanoparçacıklarının CdS kabuğu ile çevrelenmesi sonucu parçacıkların fotoluminesan kuantum verimleri %45'lere kadar çıkmaktadır. Başlangıçta kullanılan metal ($Zn/Zn+Cd$) mol oranlarının ve büyüme zamanlarının değiştirilmesi ile $Zn_xCd_{1-x}Te$ üçlü nanoalaşımalar sentezlenmiştir. Büyüklüğü ve kompozisyonu ayarlanabilir $Zn_xCd_{1-x}Te$ üçlü nanoalaşımaları luminesan özellik göstermektedir. Düşük Zn miktarı ile başlayan reaksiyonlar sonucunda elde kristaller Cd açısından zengin, Zn açısından fakir kristal içyapısına sahiptirler. Ancak yüksek Zn miktarı ile başlayan tepkimeler sonucu oluşan nanoalaşımaların Zn açısından zengin ve Cd bakımından fakir kristal içyapıları vardır.

CdTe/CdS nanokristallerinin büyüklüğünün, $Zn_xCd_{1-x}Te$ üçlü nanoalaşımaların büyüklüklerinin ve kompozisyonlarının eksiton etkileşimleri ve dinamikleri üzerine etkisi incelenmiştir. Lazer atımı 10^{15} foton/cm² olduğunda eksiton etkileşimleri, çıkış sinyalinde amplifikasyon doğurmaktadır. Eksiton yarı ömürleri piko-saniye ile nano-saniye aralığındadır. Bozunma spektrumları lazer gücünden, nanokristal boyut ve kompozisyonundan etkilenmektedir.

Lazer gücü arttıkça, özellikle $Zn_xCd_{1-x}Te$ üçlü alaşım sistemlerinde yeni eksitonik haller oluşmaktadır. Nanokristallerde lazer gücüne bağlı olarak çoklu-eksitonlar yaratılmıştır. Küçük nanokristaller büyük nanokristallere kıyasla yüksek lazer gücü altında güçlü eksiton-eksiton etkileşimleri sergilemektedir. Büyük nanokristallerde ise daha düşük eksiton yoğunluğundan dolayı eksiton-eksiton etkileşimi azalmaktadır.

TABLE OF CONTENTS

LIST OF FIGURES	viii
LIST OF TABLES.....	xv
CHAPTER 1. INTRODUCTION	1
1.1. Aim of This Study	1
1.2. Nanotechnology and Nanoscience.....	1
1.3. Semiconductor Nanoparticles.....	2
1.4. Synthesis of Semiconductor Nanocrystals	9
1.5. Types of Semiconductors	12
1.6. The Effects of Nanocrystal Size and Composition on Excited State Properties of Exciton.....	14
1.7. Characterization of Nanocrystals.....	20
1.7.1. Optical Characterization	20
1.7.2. Structural Characterization	22
CHAPTER 2. SYNTHESIS AND CHARACTERIZATION OF WATER- DISPERSIBLE CdTe AND CdTe/CdS SEMICONDUCTOR COLLOIDAL NANOCRYSTALS	26
2.1. Introduction	26
2.2. Experimental.....	27
2.3. Synthesis	28
2.3.1. Preparation of Te Precursor	28
2.3.2. Synthesis of CdTe Nanocrystals.....	29
2.4. Synthesis of CdTe/CdS Core Nanoparticles.....	30
2.5. Results and Discussions.....	31

2.6. Conclusion	46
CHAPTER 3. DEVELOPMENT OF COLLOIDAL $Zn_xCd_{1-x}Te$ TERNARY NANOALLOYS: TUNING SPECTRAL PROPERTIES OF THE NANOALLOYS BY SIZE AND COMPOSITION	47
3.1. Introduction	47
3.2. Experimental.....	50
3.2.1. Synthesis	50
3.2.1.1. Synthesis of NaHTe as Te Precursor.....	50
3.2.1.2. Synthesis of $Zn_xCd_{1-x}Te$ Ternary Nanoalloys	51
3.3. Results and Discussion	53
3.4. Conclusion	75
CHAPTER 4. EXCITON DYNAMICS OF COLLOIDAL $Zn_xCd_{1-x}Te$ NANOALLOYS	77
4.1. Introduction	77
4.2. Experimental Setup	79
4.3. Time-Resolved Measurements of $Zn_xCd_{1-x}Te$ Colloidal Nanoalloys	82
4.4. Results of Time-Resolved Measurements of $Zn_xCd_{1-x}Te$ Nanoalloys	84
4.5. Conclusion.....	101
CHAPTER 5. EXCITON DYNAMICS OF CdTe AND CdTe/CdS COLLOIDAL NANAOCRYSTALS	103
5.1. Introduction	103
5.2. Time-Resolved Measurements of CdTe Core and CdTe/CdS Core/Shell Nanocrystals.....	104
5.3. Conclusion	113

CHAPTER 6. CONCLUSION	115
REFERENCES	120

LIST OF FIGURES

<u>Figure</u>	<u>Page</u>
Figure 1.1. (a) Nanocrystals (middle) bridge the gap between cluster molecules (right) and bulk materials (left). (b) A bulk semiconductor (left) has continuous conduction and valence energy bands separated by a fixed energy gap, E_g , while a semiconductor nanocrystal (right) is characterized by discrete atomic-like states and a nanocrystal-size dependent energy gap.	3
Figure 1.2. Exciton Bohr diameters and band gap energies of some semiconductors. This is the relevant length scale for confinement. Clearly it is material dependent.	5
Figure 1.3. The continuous absorption spectrum of a bulk semiconductor, in black, compared with a discrete absorption spectrum of a quantum dot.....	6
Figure 1.4. Emission maxima and sizes of nanocrystals of different composition	9
Figure 1.5. Photoluminescence spectra of CdSe nanocrystals before and after passivation with different types of inorganic semiconductor shells	13
Figure 1.6. Tuning the quantum dot emission wavelength by changing the nanoparticle size. The emission of a CdSe quantum dot may be adjusted to anywhere within the visible spectrum (450–650 nm) by selecting a nanoparticle diameter between 2 and 7.5 nm.....	15
Figure 1.7. Tuning the quantum dot emission wavelength by changing the nanoparticle composition. While keeping the nanoparticle size constant (5nm diameter) and varying the composition of the ternary alloy $CdSe_xTe_{1-x}$, the emission maximum may be tuned to any wavelength between 610 and 800 nm.....	16
Figure 1.8. Internal structures and optical properties of core-shell and alloyed $CdSe_{1-x}Te_x$ QDs: (a) schematic drawings of four different types of QDs; (b) their corresponding fluorescence emission spectra. (1) Traditional core-shell CdTe-CdSe dots; (2) reversed core-shell dots; (3) homogeneous alloyed dots; and (4) gradient alloyed dots	18
Figure 1.9. Comparison of the emission spectra among CdSe, CdTe, and $CdSe_{0.34}Te_{0.66}$ QDs at three particle sizes	19

Figure 1.10. (a) Schematic path for absorption of light, vibrational relaxation and fluorescence emission or relaxation through trap states, (b) Simple representation of Jablonski diagram	21
Figure 2.1. Structures of (a) 3 – Mercaptopropionic acid and (b) Thioglycolic acid	27
Figure 2.2. Photograph of experimental set up (two neck round bottom borosilicate reaction flask).....	29
Figure 2.3. Structure of Thiourea.....	30
Figure 2.4. PL emission spectrum of CdTe NCs synthesized with different amount of TGA.	32
Figure 2.5. PL emission and UV-Vis spectra of TGA capped CdTe synthesized in concentrated medium 280 min (left) and dilute (right) medium within 370 min. The insert on the right figure shows the size of CdTe NCs measured by DLS.....	33
Figure 2.6. PL emission spectra of TGA capped CdTe purified with different solvents	34
Figure 2.7. UV-Vis and PL emission spectra of TGA-capped CdTe. Insert: Schematic of TGA-capped NCs.....	35
Figure 2.8. Normalized (a) absorption and the corresponding (b) emission spectra of CdTe NCs during growth. The reaction time is indicated in the figure. The excitation wavelength for PL measurement was 400 nm.....	35
Figure 2.9. PL emission maximum as a function of reaction time	36
Figure 2.10. XRD pattern of TGA stabilized larger size CdTe NCs (PL emissions wavelength 635 nm).....	37
Figure 2.11. Growth kinetics of CdTe/CdS core shell NPs.....	38
Figure 2.12. Schematic illustration of synthesis of CdTe/CdS core shell nanocrystals.....	38
Figure 2.13. Normalized (a) UV-Vis and the (b) PL emission spectra of CdTe/CdS core shell NCs obtained after optimization. (Te: S 1:10)	39
Figure 2.14. Luminescence image of CdTe / CdS NCs under day and UV light.	40
Figure 2.15. XRD pattern of different sized CdTe/CdS NCs, the lines representing blue lines show 2 theta of face centered cubic bulk CdTe (bottom), the dot red lines represent the 2 theta of face centered cubic bulk CdS (top). NCs have zinc blend structure.....	41

Figure 2.16. AFM picture of TGA-capped CdTe/CdS NCs (Te:S 1:10).....	42
Figure 2.17. EDX map of TGA-capped CdTe/CdS NCs (Te:S 1:10). Insert: the table shows ICP-MS results of TGA-capped CdTe/CdS NCs.....	42
Figure 2.18. TEM images of CdTe/CdS core shell NCs (a) 20 nm, (b) 10 nm, and (c-d) 5nm scale.....	43
Figure 2.19. PL decay curves of exciton emission of (a) CdTe NCs of increasing size, (b) CdTe/CdS NCs of increasing size, (c) CdTe and CdTe/CdS NCs emitted at 535 nm wavelength, and (d) CdTe and CdTe/CdS NCs emitted at 555 nm wavelengths.....	44
Figure 3.1. Schematic representation of having a (a) homogeneous, (b) gradient, and (c) core-shell structure of spherical NCs.....	48
Figure 3.2. Schematic illustration of synthesis of $Zn_xCd_{1-x}Te$ ternary nanoalloys.....	52
Figure 3.3. Images of $Zn_xCd_{1-x}Te$ nanoalloys with different Cd:Zn ratio under day (above) and under UV light(below).....	53
Figure 3.4. Change in the respective mole ratios of Zn and Cd in colloidal nanoalloys synthesized under different metal precursor concentration with various growth times to keep the time to keep the size constant. $Zn/Zn+Cd$ were changed from 0.04 to 0.92.....	56
Figure 3.5. (a-d) Change in the respective mole ratios of Zn and Cd in colloidal nanoalloys synthesized under different mole ratio of metal precursors through reflux time. The change is followed by ICP-AES. (e) Schematic representation of homogeneous and heterogeneous nanoalloy structures.	57
Figure 3.6. X-ray powder diffraction pattern of the crystals formed when $Zn/Zn+Cd$ mole ratio in precursor solution is 1. Insert: (upper) The mismatched lines represents the characteristic XRD peaks of ZnTe, (lower). Matched lines belongs to the characteristic XRD peaks of Te crystals.....	60
Figure 3.7. Change in $Zn/Zn+Cd$ mole fractions in nanoalloy structure with $Zn/Zn+Cd$ mole ratio in precursor solutions. ICP-AES is used to measure the relative amount of Zn in nanoalloys. Insert: Change in $Zn:Cd$ mole ratio in the nanoalloy with the initial Zn:Cd ratio.	61

Figure 3.8. The temporal evolution of peak position of PL emission peaks of TGA-capped $Zn_xCd_{1-x}Te$ nanoalloys. The initial Zn/Zn+Cd mole ratio in precursor mixture was varied.....	62
Figure 3.9. Size distributions of the nanoalloys obtained from different initial Zn/Zn+Cd mole ratio.	63
Figure 3.10. STEM images of $Zn_{0.18}Cd_{0.82}Te$ nanoalloys at 1 μ m scale (a) redispersed in pure water (b) redispersed in pH-adjusted water (c-d) HRTEM images of $Zn_{0.21}Cd_{0.79}Te$ and $Zn_{0.46}Cd_{0.54}Te$ nanoalloys at 5nm scale. The inserts illustrate an electron diffraction pattern taken in the same area.....	65
Figure 3.11. X-Ray powder diffraction patterns of (a) homogeneous $Zn_xCd_{1-x}Te$ nanoalloys (b) heterogeneous $Zn_xCd_{1-x}Te$ nanoalloys synthesized by using different amount of Zn/Zn+Cd precursor ratio.	66
Figure 3.12. FTIR spectrum of TGA and TGA capped $Zn_xCd_{1-x}Te$ nanoalloys	68
Figure 3.13. (a)Normalized UV-Vis and PL spectra of the $Zn_{0.12}Cd_{0.88}Te$ nanoalloys through growth. The nanoalloys were grown for 200 min. Insert: Change in respective mole ratios of Zn and Cd in the NCs by ICP-AES and DLS measurements (b)Normalized UV-Vis and PL spectra of the 9.5 \pm 2.4 nm sized $Zn_{0.18}Cd_{0.82}Te$, $Zn_{0.46}Cd_{0.54}Te$, and $Zn_{0.56}Cd_{0.44}Te$ nanoalloys. Insert: Size distributions of the nanoalloys obtained from different Zn/Zn+Cd mole ratio in precursor.....	69
Figure 3.14. Graphical representation of (a) the change in PL peak position (b) the change in QY with the fraction of Zn in the nanoalloys (Table 3.4).	72
Figure 3.15. The typical UV-Vis spectra (left) and PL (right) spectra of the $Zn_xCd_{1-x}Te$ nanoalloys solution with particle concentration of 37 mg/L from room temperature and 0 to 210 min at 343K. (Insert: picture of the annealed nanoalloys under UV light).....	73
Figure 3.16. Experimental data of variation in the sizes of $Zn_xCd_{1-x}Te$ nanoalloys as a function of time for three different primary concentrations	74
Figure 3.17. Average diameters, d, of the TGA-capped $Zn_xCd_{1-x}Te$ nanoalloys (a)at 10 min of the initial heating stage, and (b)at 150 min of the latter heating stage vs primary particle concentrations at different temperatures (343,353, and 363K).....	74

Figure 4.1. Schematic representation of (a) a streak camera and (b) the synchroscan streak-camera setup in Laboratory of Biophysics, Wageningen University, Wageningen, The Netherlands.....	80
Figure 4.2. Streak images of $Zn_xCd_{1-x}Te$ ternary colloidal nanoalloys (above). Fluorescence intensity of nanoalloys is represented by colors from red (high) to blue (low). The time resolved emission spectra of the nanoalloys obtained from a picoseconds resolved Streak camera (below). Position resolved decays of the nanoalloys from shorter to longer time windows (Right).	82
Figure 4.3. Hot carrier relaxation/cooling dynamics in semiconductor	84
Figure 4.4. Schematic illustration of charge carrier relaxation in semiconductor nanocrystals.....	84
Figure 4.5. Streak camera images of (a) 4.5 ± 1.4 nm sized (b) 9.5 ± 2.4 nm sized $Zn_xCd_{1-x}Te$ colloidal nanoalloys (from up to down) excited with different laser power: 1mW, 10 mW, 100 mW, from left to right, respectively. Fluorescence intensity of the nanoalloys is represented by colors from red (high) to blue (low).	86
Figure 4.6. The emission intensity spectra of 4.5 ± 1.4 nm and 9.5 ± 2.4 nm sized $Zn_xCd_{1-x}Te$ colloidal nanoalloys at initiation time obtained under different laser power, correspondingly from low to high, of 1 to 100mW. Blue arrows represent the one exciton state in nanoalloys and shows extent of increase in PL intensity with laser power. Red arrows show the multiexciton states and the contribution of the state with laser power.....	88
Figure 4.7. Schematic representation of Auger recombination in terms of energy bands. Two electrons and a hole (left) recombine to form a “hot” electron (right), with time constant τ_e	89
Figure 4.8. The dependence of emission intensity of 4.5 ± 1.4 nm and 9.5 ± 2.4 nm sized $Zn_xCd_{1-x}Te$ colloidal nanoalloys on the laser power.	89
Figure 4.9. Different localization regimes supported by inverted ZnSe/CdSe hetero-NCs in the case of a fixed core radius and different shell widths.....	91
Figure 4.10. (a) ASE spectra of type-I CdSe NCs excited by 100-fs pulses at 3 eV. Insert, transient-absorption dynamics measured for the NCs. (b) the	

<p>pump-intensity-dependent photoluminescence spectra of the type-II sample show the development of a narrow ASE peak near the centre of the single-exciton emission band. The second ASE band, which develops at higher fluences, is located near the XX photoluminescence feature</p>	91
<p>Figure 4.11. The change in the photoluminescence peak position of 4.5 ± 1.4 nm and 9.5 ± 2.4 nm sized $Zn_xCd_{1-x}Te$ colloidal nanoalloys with the laser power correspondingly from low to high, of 1 to 100mW at initiation time ($t=0$ ps).....</p>	92
<p>Figure 4.12. The time resolved emission spectra of $Zn_{0.12}Cd_{0.88}Te$ and $Zn_{0.21}Cd_{0.79}Te$ colloidal nanoalloys obtained from ps resolved Streak camera images. Size of nanoalloys is 4.5 ± 1.4 nm.</p>	93
<p>Figure 4.13. The time resolved emission spectra of $Zn_{0.18}Cd_{0.46}Te$ and $Zn_{0.46}Cd_{0.54}Te$ nanoalloys obtained from a ps resolved Streak camera images. Size of nanoalloys is 9.5 ± 2.4 nm.....</p>	94
<p>Figure 4.14. Schematic representation of one-exciton state and two-exciton state in the the colloidal $Zn_xCd_{1-x}Te$ nanoalloys</p>	95
<p>Figure 4.15 Decay associated spectra of $Zn_{0.13}Cd_{0.87}Te$ colloidal nanoalloys obtained by global analysis of their streak camera images. The size of nanoalloys is 4.5 ± 1.4 nm. The laser power was changed from 1mW to 100mW.....</p>	96
<p>Figure 4.16. Decay associated spectra of $Zn_{0.12}Cd_{0.88}Te$ and $Zn_{0.35}Cd_{0.65}Te$ colloidal nanoalloys obtained by global analysis of their streak camera images. The size of particles is 4.5 ± 1.4 nm. The laser power changed from 1mW to 100 mW.....</p>	98
<p>Figure 4.17. Decay associated spectra of $Zn_{0.18}Cd_{0.82}Te$ and $Zn_{0.46}Cd_{0.54}Te$ colloidal nanoalloys obtained by global analysis of their streak camera images. The size of particles is 9.5 ± 2.4 nm.....</p>	98
<p>Figure 5.1. Streak camera images of CdTe (PL λ_{max}: 554 nm) nanocrystals excited with different laser power: 1mW to 100 mW, from upper left to lower right respectively. Fluorescence intensity of nanocrystals is represented by colors from red (high) to blue (low). Size of the nanocrystals is 4.1 nm.....</p>	106

Figure 5.2. Streak camera images of CdTe/CdS (PL λ_{max} : 557 nm) nanocrystals excited with different laser power: 1mW to100 mW, from upper left to lower right, respectively. Fluorescence intensity of nanocrystals is represented by colors from red (high) to blue (low).	106
Figure 5.3. The dependence of emission intensity of (a) CdTe and (b) CdTe/CdS nanocrystals on the laser power.	108
Figure 5.4. The PL emission spectra of different size CdTe core and CdTe/CdS core/shell NCs at initiation time obtained under different laser power, correspondingly from low to high, of 1 to 100mW.	109
Figure 5.5. The change in PL peak position of CdTe core and CdTe/CdS core/shell NCs with the power of laser correspondingly from low to high, of 1 to 100mW at initiation time (t=0 ps)	110
Figure 5.6. Decay associated spectra of 2.2 nm sized CdTe nanocrystals under excitation of different laser power obtained by global analysis.	111
Figure 5.7. Normalized decay associated spectra of CdTe nanocrystals obtained by global analysis.....	111
Figure 5.8. Normalized decay associated spectra of CdTe/CdS nanocrystals obtained by global analysis.....	112

LIST OF TABLES

<u>Table</u>	<u>Page</u>
Table 2.1. Fluorescence lifetime values for CdTe and CdTe/CdS NCs. χ^2 values are between 0.960 and 1.120. CdTe/CdS NCs have longer lifetime values.....	45
Table 3.1. The mole numbers of CdCl ₂ , ZnCl ₂ and NaHTe	51
Table 3.2. Chemical formula of the nanoalloys obtained by different analysis techniques.....	54
Table 3.3. Total amount of Cd and Zn in the supernatant and the aged nanoalloys measured by ICP-AES with errors.....	55
Table 3.4. Photophysical parameters of the nanoalloys with different Cd: Zn ratio (300 μ l samples diluted to 1ml with water).....	71
Table 4.1. Photophysical parameters of analyzed Zn _x Cd _{1-x} Te colloidal nanoalloys and their size (this information was reached in chapter 3).....	85
Table 4.2. Decay rate constants, corresponding lifetime with their respective amplitude of the nanoalloys	100
Table 5.1. Photophysical parameters of analyzed CdTe core and CdTe/CdS core shell nanocrystals and their size	105
Table 5.2. Average decay lifetime with their respective amplitude of nanocrystals	113

CHAPTER 1

INTRODUCTION

1.1. Aim of This Study

Aim of this study was to synthesize CdTe core, CdTe/CdS core shell, $Zn_xCd_{1-x}Te$ ternary semiconductor nanocrystals in a controlled way and to study;

- the size effects on exciton dynamics,
- the composition effect on exciton dynamics,
- on multiple excitons generation and interaction dynamics.

1.2. Nanotechnology and Nanoscience

Nanotechnology is the manipulation of matter on an atomic and molecular scale and it is one of the most popular fields in both science and industry. The lecture called “Plenty room in the bottom” by Richard Feynman is the most accepted origin about birth of the nanotechnology. According to the lecture it is claimed that scalable materials could be replicated itself in miniature to molecular scale (Feynman 1960).

Nanoscience is a new way of thinking about building up complex materials and devices by exquisite control of the functionality of matter and its assembly at the nanometer-length scale. The vision of nanoscience ultimately combines the science and engineering of man-made and biological entities, controlled at the nanometer scale, and assembled into complex, engineered structures that can interact with their surroundings at dimensions ranging from those of molecules to those of humans and beyond. In nanoscience, great attention has been received to develop nanomaterials having highly controlled and unique optical properties that depend on their size and shape, which is termed as the “quantum confinement effect” (Bae et al. 2008, Zhong et al. 2009).

Nanotechnology and nanoscience deal with nanoscale objects and systems. Nanoscale objects are smaller molecules than structures that are used in micro technologies which provide some useful physical behavior like quantum confinement

effect. Nanochemistry is an important field in the development of nanoscience and by chemistry nanostructures like nanospheres, nanorods, nanowires etc. with different compositions like metals, oxides, organics and semiconductors can be synthesized (Love et al. 2005, Bae et al. 2008).

1.3. Semiconductor Nanoparticles

Nanocrystals (NCs), the backbone in nanotechnology, are semiconductor nanoparticles (NPs) which are tiny, light emitting nanometer scale particles with unique optical and electronic properties. Colloidal semiconductors NCs are single crystals which have diameter size of a few nanometers. Many physical phenomena in both organic and inorganic materials have natural lengths between 1 and 100 nm (10^2 to 10^7 atoms). Controlling the physical size of materials can be used to tune the material properties. Nanomaterials, studied extensively during the past two decades, represent a class of materials with at least one relevant dimension on the length scale of a few dots whose radii are smaller than the bulk exciton Bohr radius constitute a class of a few hundred nanometers (Wu F. and Zhang Z. 2009).

In nanoscience, great attention has been received to develop nanomaterials having highly controlled and unique optical properties that depend on their size and shape. This dependency is called the “quantum confinement effect (QCE)” (Bae et al. 2008). Quantum dots (QDs) are defined as nanometer-scale semiconductor crystals comprised of groups II–VI or III–V elements and their size-dependent quantum confinement effects have been an area of particular focus (Jamieson et al. 2007).

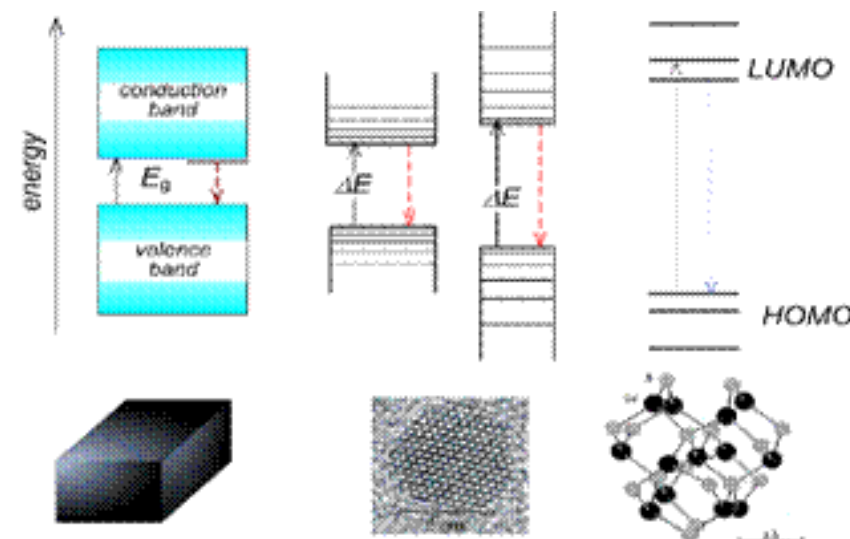


Figure 1.1. (a) NCs (middle) bridge the gap between cluster molecules (right) and bulk materials (left). (b) A bulk semiconductor (left) has continuous conduction and valence energy bands separated by a fixed energy gap, E_g , while a semiconductor NC (right) is characterized by discrete atomic-like states and a NC-size dependent energy gap. The discrete levels inhibit phonon emission (Source: Klimov et al. 2008).

Semiconductor nanocrystallites (quantum materials) form an intermediate regime between molecular and bulk forms of matter as shown in Figure 1.1. In the nanometer size regime, new mesoscopic phenomena characteristic of this intermediate state of matter can be found in neither bulk nor molecular systems. Although nanocrystallites have not yet completed their evolution into bulk solids, structural studies indicate that they retain the bulk crystal structure and lattice parameter (Dabbousi et al. 1997). A fascinating feature of NPs is that their small size results in spatial confinement of the wave function of charge carriers (Alivisatos 1996, Kagan et al. 1996).

Quantum confinement of both the electron and hole in all three dimensions affects the energy levels in semiconductor NCs that are physically smaller than the exciton Bohr radius of the constituent material and leads to an increase in the effective band gap of the material with decreasing crystallite size. Quantum confinement yields discrete energy states rather than bands. Consequently, both the optical absorption and emission of QDs shift to blue region (higher energies) as the size of dots gets smaller (Dabbousi et al. 1997). The confinement of excitations, electronic and vibrational, dominates the physical properties of semiconductor NCs (Murray, Norris, and Bawendi 1993). When a bulk semiconductor crystals' size is reduced the surface area/volume

ratio increases and the surface structure affects both optical and electronic properties strongly (Zhang 1997). The decrease in size results in increase in energy level spacing and leads impacts on the rates of dissipation of excess electronic energy of the carriers. The crystal's electronic properties stop behaving as bulk structure. This behavior is a result of quantum confinement effects, the behavior of electrons in a particle due to spatial restrictions.

Semiconductor NPs offer possibility to study a state of matter intermediate between bulk and isolated atoms or molecules as well as the effect of spatial confinement on electron behavior and also an opportunity is provided to investigate problems related to surfaces or interfaces because of their interfacial nature (Zhang 1997).

The size and surface characteristics of NPs are the key factor during confinement. Both size and surface are interrelated since the S/V ratio increases as the size decreases. For a spherical particle, the *surface/volume* ratio is inversely proportional to its radius, R , i.e., $S/V = 3/R$. This confinement effect becomes significant especially when the size is smaller than the Bohr exciton radius, which is around 24 Å for CdS (Gratzel, M. 1989).

NCs keep the structural features of the bulk solid but particularly different electronic properties as a function of their size. Quantum size effect occurs when the nanostructures themselves becomes smaller than a fundamental scale. Such a fundamental scale is determined by the exciton Bohr radius.

In a semiconductor NC, optical excitation should require a minimum energy equal to the band gap energy (E_g). The transfer of electron from lower band to upper band is accepted as moving through a "hole", and this electron-hole pair becomes electrostatically bound. This excitation is a bound electron-hole pair. This is because the pair bound and therefore it requires less energy to excite it. An exciton is a bound state of an electron and an imaginary particle called a hole in an insulator or semiconductor, and such is a Coulomb-correlated *electron-hole pair*. This pair -called as an exciton- has a lot of properties similar to the hydrogen atom and like the hydrogen atom the exciton has a Bohr diameter. This length is material-dependent and when the size of the material becomes comparable to that of the exciton Bohr diameter confinement effects become important. If the size of the dot is 3-10 times the exciton Bohr diameter the dot is said to be in the weak confinement regime, but if it is smaller the dot is in the strong confinement regime (Huffaker et al. 1998). Exciton formation is an elementary

excitation or a quasiparticle of a solid (Dagott 2009). Exciton Bohr diameters and band gap energies are material dependent and Figure 1.2 shows exciton Bohr radius and band gap energies of some semiconductors.

The bound electron and hole pairs (excitons) provide a means to transport energy without transporting net charge. Since an exciton is a bound state of an electron and a hole, the overall charge for this quasiparticle is zero. Hence it carries no electric current (Liang W.Y. 1970).

Semiconductor	Exciton Bohr Diameter	Band gap Energy
CuCl	13Å	3.4 eV
ZnSe	84Å	2.58 eV
CdS	56Å	2.53 eV
CdSe	106Å	1.74 eV
CdTe	150Å	1.50 eV
GaAs	280Å	1.43 eV
Si	37Å(longitudinal) 90Å(transverse)	1.11 eV
Ge	50Å(longitudinal) 200Å(transverse)	0.67 eV
PbS	400Å	0.41 eV

Figure 1.2. Exciton Bohr diameters and band gap energies of some semiconductors. This is the relevant length scale for confinement. Clearly it is material-dependent (Source: Dagott 2009).

When an electron is confined to a volume in space, it acquires kinetic energy (referred to as confinement energy), and its energy spectrum becomes discrete. In a bulk semiconductor, the conduction electrons are free to move around in the solid, so their energy spectrum is almost continuous. The density of allowed electron states-per-unit energy increases with the square root of the energy (Figure 1.3). If one can synthesize a piece of the semiconductor that is so small the electron “feels” confined, the continuous spectrum will become discrete, and the energy gap will increase.

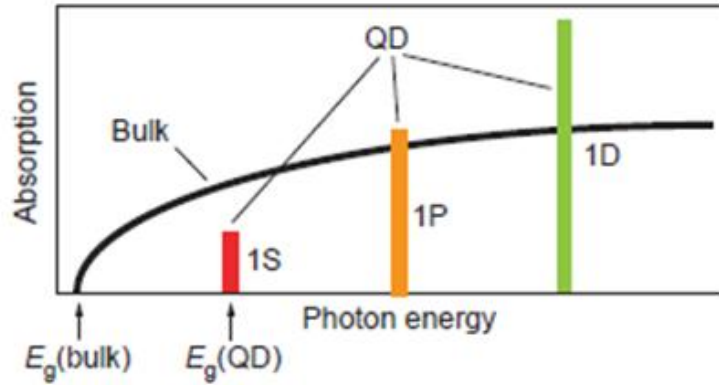


Figure 1.3. The continuous absorption spectrum of a bulk semiconductor, in black, compared with a discrete absorption spectrum of a quantum dot, in the bars of color (Source: Klimov et al. 2000).

The quantum confinement enhances the electron-hole Coulomb interactions, thus amplifying signatures of the exciton such as its fine structure. When the excited electron loses its excess energy radiatively or non-radiatively in the conduction band, it returns to valance band and reemerges with the hole (Zhong et al. 2009).

As an exciton forms in a spatially confined box smaller than the Bohr radius, to confine the exciton, much more energy is needed. The band gap (E_g) between valence and conduction bands increases. As QD size decreases, the absorption and emission wavelengths decrease, and the emitted light shifts to blue region. In other words blue shift happens in light that occurred due to energy loss of electron-hole pair, which means light occurs in a shorter wavelength (higher energy).

For the quantum-confined systems such as QDs, the energy structure calculation can be carried out using two alternative approaches. In one approach the band structure of a bulk solid can be studied and by (quantized) shrinking the bulk materials to QDs the energy of the systems can be calculated. In another approach, which is the complicated one, the calculation of energy can start from the individual electronic states of a single isolated atom, than the calculation can be done to understand how the energy levels evolve as atoms come closer and start interacting with each other.

As an exciton forms in a spatially confined box smaller than the Bohr radius, to confine the exciton, much more energy is needed. The minimum energy required to form an exciton in a confined region can be ascribed to the bulk band gap energy and the confinement energy for the electron carriers in a potential well. The whole confinement energy for the exciton can be described by “particle in a box” system in

which the electron motion is restricted in all three dimensions by an impenetrable wall (Efros and Efros 1982):

$$E_{well} = \frac{h^2}{2m^*d^2} \quad \frac{1}{m^*} = \frac{1}{m_e} + \frac{1}{m_h} \quad (1.1)$$

In which h is Planck's constant, d is diameter, m^* is reduced mass of exciton.

Coulombic interactions have also effect on exciton energy and the coulomb energy is described as:

$$E_{Coul} = \frac{-1.8e^2}{2\pi\epsilon\epsilon_0d} \quad (1.2)$$

where e = electron charge (C), ϵ = permittivity constant and ϵ_0 = dielectric constant

The band gap energy of a quantum dot can be calculated by combining these two energy equations. This is known as effective mass approximation. Both E_{Coul} and E_{Well} include diameter term. For a spherical QD with diameter (d), this model predicts that a size dependent contribution to the energy gap is simply proportional to $1/d^2$, implying that the gap increases as the QD size decreases and the (E_{well}) confinement term determines the energy level (Franceschetti and Zunger 1997, Efros and Efros 1982).

$$E(\text{dot}) = E_g(\text{bulk}) + E_{well} + E_{Coul} \quad (1.3)$$

$$E = E_g + \frac{h^2}{2m^*d^2} - \frac{1.8e^2}{2\pi\epsilon\epsilon_0d} \quad (1.4)$$

The confinement leads to a collapse of the continuous energy bands of a bulk material into discrete, atomic-like energy levels and the discrete energy states leads to a discrete absorption spectrum of QDs which is in contrast to the continuous absorption spectrum of a bulk semiconductor (Klimov et al. 2000).

Semiconductor and metal particles occupy the center of scientific interest due to their unique electronic nature. They follow quantum mechanical rules instead of the laws of classical physics governing bulk materials. Both equilibrium and dynamic properties of nanomaterials can be very different from those of their corresponding bulk materials or isolated atoms and molecules. Their properties are often strongly dependent on the particle size, shape, and surface properties (Ekimov et al. 1989, Henglein 1989) .

Because of their superb optical and electronic properties, NCs are (potential) building blocks for new electronic and optical nanodevices such as quantum computers, light-emitting diodes, solar cells, or lasers (Bae et al. 2008). Recently, QDs also have been used in biotechnology as fluorescent biological labels (Bruchez et al. 1998, Alivisatos 1999, Nie et al. 2007, Jamieson et al. 2007). The physics of nanodisperse semiconductors have been investigated in some depth and devices incorporating quantum material have been realized (Green and O'Brien 2004, Erokhin et al. 1998, Colvin, Schlamp, and Alivisatos 1994). For example, the wavelength of an NC laser can be tuned by choosing the NC size in the gain medium CdTe NCs are of particular interest for their applications in optical switches, light emission diodes, solar cells, chemical sensors, and *in vivo* biomedical imaging (Zhong et al. 2009).

In the nanosize regime, properties of nanomaterials include brightness, emission color, color purity, quantum yield, and emission temperature stability become strongly dependent on surface characteristics, shape, and size. Since the emission color of semiconductor NCs is strongly dependent on morphology, the color purity of emission is dependent on the distribution of size of colloidal NCs. It is, in principle, possible to adjust the properties such as the color and redox potentials of nanomaterials by changing the particle size or shape, without any change of chemical composition (Zhang 1997, Alivisatos 1996, Nonoguchi, Nakashima, and Kawai 2007). Semiconductor NC samples must be monodisperse in terms of size, shape, internal structure, and surface chemistry. Shape control in the synthesis of colloidal semiconductor nanostructures offers an unprecedented ability to tune the interaction of solid state quantum structures with the environment, opening up the possibility of performing truly nanoscale manipulations of the optical and electronic properties (Sarkar et al. 2007, Cheng et al. 2006, Li et al. 2005).

The optical materials with nanoscale sizes are also sensitive to the surrounding environment. During the last decade, considerable theoretical and experimental efforts have been made in the fundamental aspects of quantum confinement effects, and optical properties of nanoscale materials. As it is well known, a decrease of particle size will influence the most important contributions to the optical properties of nanoscale materials, which are quantum size effects, surface effects, and surrounding environments (Wu et al. 1997, Zhang et al. 2003).

The size, surface and the shape of the NCs are controlled by changing reaction parameters such as amount-type of reactants, stabilizers and reaction temperature used

in the synthesis, etc. Synthesis and optical spectroscopy of many types of semiconductor NCs are proposed to develop high quality optical NCs. The high quality optical NCs are considered to have high luminescence efficiency, temperature-stable emission, high color purity, and environmental stability without reduction in performance due to high temperature, or by exposure to oxygen, nitrogen, and moisture.

There are many types of QDs in literature and Figure 1.4 shows some examples. Their emission maxima are size- and composition-tunable, ranging from UV to IR region. Generally, they could be synthesized by the semiconductor materials from periodic table group II-VI as CdS, CdSe, group III-V as InP, InAs, group IV-VI as PbSe.

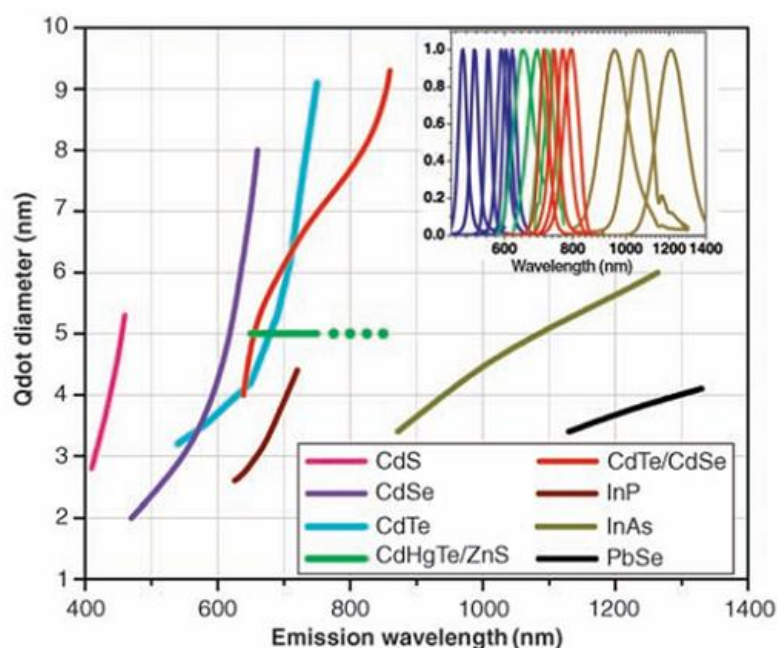


Figure 1.4. Emission maxima and sizes of nanocrystals of different composition (Source : Michalet et al. 2005).

1.4. Synthesis of Semiconductor Nanocrystals

Researchers have studied on various methods to synthesize semiconductor QDs recently. QDs were developed by many different synthesis methods, which are high temperature organometallic routes (Steigerwald and Sprinkle 1987), high temperature greener synthesis (Jang, Jun, and Pu 2003), single source precursors, micellar methods, catalytic growth, two phase approach, solvo(hydro)thermal method and one-pot approach, etc. (Donega 2011, Khatei, Pendyala, and Rao 2011, Lee, Holloway, and

Yang 2006, Lesnyak et al. 2009, Murray, Norris, and Bawendi 1993, Kortan et al. 1990, Murray, Kagan, and Bawendi 1994). Choosing the proper synthesis method is important to obtain QDs with desirable optical and compositional properties.

The synthesis can be considered as growth of a crystal structure, it is very important to control temperature during synthesis. The average size and the size distribution are dependent on the growth temperature. Generally growth of NCs appeared consistent with Ostwald ripening. In this solution-crystallizer phenomenon small crystals more soluble than large ones dissolve and re-precipitate onto larger particles.

Monodisperse growth is very important to have QDs with high optical properties. By controlling temperature and pressure of the medium, it is extremely difficult to synthesize monodisperse QDs, because QDs can accumulate in an instant, and thus bulk crystal structures form. However, organic surfactants may help to synthesize monodisperse QDs. Semiconductor NCs (NCs) constitute particularly complex and challenging nanoscale systems due to their hybrid nature combining a single crystalline nanoscale solid surrounded by organic ligands (Kraus et al. 2007).

Moreover to prevent agglomeration and to obtain monodisperse semiconductor NCs, the surfactants are used. Besides, the surfactants (capping agents) are helpful to meet specific aims such as water-solubility, chemical reactivity. Also they can be used as solvent in high temperature organometallic route. The most commonly used capping agents are trioctylphosphine oxide (TOPO) (Pan et al. 2004), oleic acid (Bullen et al. 2004), 3-Mercaptopropionic acid (MPA) and Thioglycolic acid (TGA) (Gu et al. 2008).

In one study, the effects of temperature and oleic acid on the growth kinetics of CdSe NCs in octadecene have been investigated. It was observed that increasing stabilizer concentrations led to lower nuclei concentrations, smaller nuclei size and larger final particle size. It was also observed that at higher temperatures, particles nucleated with smaller radii than those present at lower temperatures. This, according to Bullen *et al.*, indicates that the nucleation is faster as temperature increases and that growth kinetics are less strongly dependent on temperature. Consequently, higher temperatures produce more nuclei (Bullen et al. 2004).

In another study, Dabbousi *et al.* synthesized monodisperse QDs by high temperature organometallic routes under airless media. Cadmium precursor and selenium, tellurium or sulfur precursors are dissolved in surfactant (TOPO or TOP generally) under nitrogen or argon atmosphere, at around 300 °C. At high temperature,

nucleation occurs and lowering temperature a little from 300 °C to 280 °C initiates the growth of QDs within monodisperse size (Dabbousi et al. 1997).

It is apparent that traditional experimental parameters can and do affect growth dynamics but, not surprisingly, the variability of surface atoms had a greater influence on the optical properties. For example during CdSe NCl synthesis, an increase in the Cd:Se molar ratio and Cd:stabilizer molar ratio had a profound effect on the NC's quantum yield. QDs have a higher surface area-to-volume ratio than their bulk analogues. Surface reconstruction and composition are expected to have a large influence on the optical properties of semiconductor NCs. Literature recognizes the role of the surface in determining the quantum yields of semiconductor NCs (Donega et al. 2003 and Dabbousi et al. 1997). To better understand how growth conditions determine the surface structure of CdSe NCs prepared under high-temperature, more comprehensive studies of each contribution of individual parameters including ratio of precursors, reaction volume, reaction time, temperature, pressure and the effect of their combination must be studied.

The two-phase approach is more preferable method due to its low toxicity, easy-performing and lower temperature requirement. The method was firstly used to synthesize 1 - 3 nm gold NCs in which thiol-capped gold NCs were formed by the reduction of AuCl₄ by sodium borohydride in the presence of an alkanethiol solution (Brust et al. 1994). Some noble NCs were synthesized by this method successfully. Pan *et al.* were the first group who synthesized highly luminescent, monodisperse CdS NCs in the toluene–water interface (Pan et al. 2004).

During solvo/hydro-thermal synthesis, stainless steel autoclave is used as reaction flask. A simple and general one-step surfactant-assisted solvothermal synthesis method was developed to synthesize metal tellurides which are CoTe, Ag₂Te/Ag and CdTe by Jiang and Zhu and to synthesize CdTe, CdSe NCs in a controlled shape and size by Wang et al. (Jiang and Zhu 2010, Wang et al. 2006).

One-pot aqueous synthesis is an alternative way to organometallic synthesis routes. This method is the most commonly used method because it is less toxic and less expensive. Reaction can occur in aqueous medium and different groups like amine, mercapto-groups can be used as capping agents. Many types of water dispersible semiconductor NCs have been synthesized by means of the method (Lesnyak et al. 2009).

1.5. Types of Semiconductors

A quantum dot (QD) is a semiconductor whose excitons are confined in all three spatial dimensions. As a result of 3-D confinement, the semiconductors have properties that are between those of bulk semiconductors and those of discrete molecules. Also quantum confined semiconductors include (a) quantum wires, which confine electrons or holes in two spatial dimensions and allow free propagation in the third and (b) quantum wells, which confine electrons or holes in one dimension and allow free propagation in two dimensions.

QDs differ in many ways and there are some distinct terms that QDs are grouped in. QDs can be classified in two groups according to their atomic arrangement in crystal structure such as core types and core/shell types.

There are different kinds of core and core/shell type including alloy type QDs depending on atom type; CdS, CdSe, CdTe, ZnS, PbS, PbSe, GaInP₂, CdHgTe, CdSe_xS_{1-x}, CdSe / ZnS, CdSe / CdS, CdTe / CdS, CdTe/CdSe, Cd_xZn_{1-x}Te, Cd_xZn_{1-x}Te/CdS, CdSe/CdS/ZnS and CdSe/ZnSe/ZnS, CdS/ZnSe ... (Pan et al. 2007, Jang, Jun, and Pu 2003, Talapin et al. 2004, Peng et al. 2007, Chin et al. 2007, Qian et al. 2007, Xu et al. 2010, Li et al. 2010, Song, Duan, and Zhan 2010).

A core type quantum dot consists of atoms of two or three different types. However, coating the core of quantum dot, which means surrounding core with a shell consisting of different kind of atoms, causes a great enhancement in optical properties, such as quantum yield and photo stability. This type of QDs is called core/shell type QDs. By surrounding a core with a shell or two shells, the band gap profile, charge carrier properties and luminescence properties of crystal can be modified. With a shell the nature of carrier confinement in the core can be manipulated and so the optical properties of core structure will change.

Detailed study on core QDs have showed that core type semiconductors loses their luminescent properties by time. Since atoms on large surface area could not be fully coordinated, dangling bonds of NC surface generated non-radiative decay energy levels to reduce quantum yield. By coating with growing a thin inorganic shell on the surface of the core, the loss can be decreased by surface passivation and the coating makes crystal structure less defective. The semiconductors may be toxic and may easily oxidize. The coating also reduces their toxicity and oxidation. The basic rationale in

core/shell synthesis is, first to grow a kind of core NC, then to grow a different kind of inorganic layer around core which has a close crystal structure of core material. This thin shell around core, improves optical properties of core structure dramatically as seen in Figure 1.5.

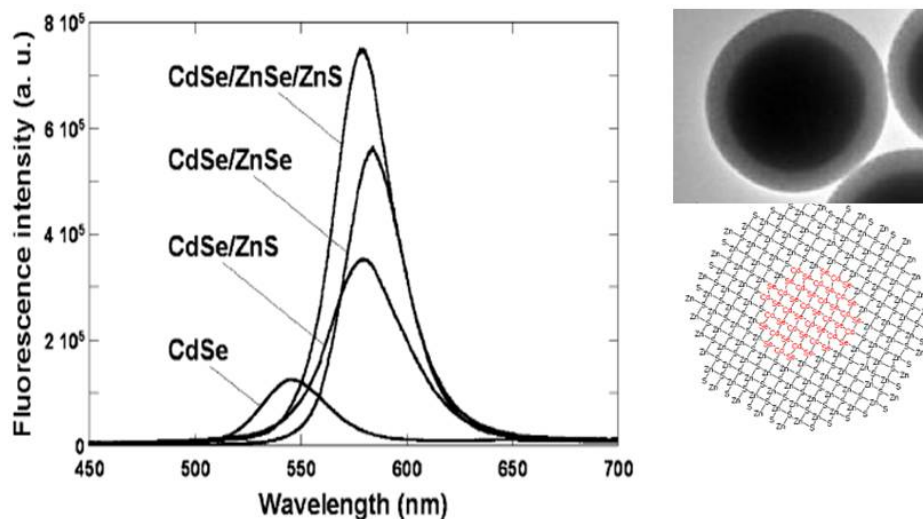


Figure 1.5. Photoluminescence spectra of CdSe nanocrystals before and after passivation with different types of inorganic semiconductor shells (Source: Reiss et al. 2003).

In literature there are some studies on core – shell – shell and core – shell – shell – . . . – shell QDs. Core/shell/shell structure is preferred because of high quantum yield, and stable optical properties of the new semiconductor. The main reason for coating surface with more shell structures is basically to get more advanced QDs. Addition of new shell increases the confinement of electron and hole inside the NC as well as high photochemical stability and PL efficiency (Figure 1.5). But sometimes during coating, the structure of core and thereby its chemical properties will be destroyed and more layers will introduce some defects in cores. It is not easy to control the shell thickness of middle and outer shell, so studies cannot be interpreted easily. Also, adding more shell does not always improve photophysical properties of core structures (Pan et al. 2006).

1.6. The Effects of Nanocrystal Size and Composition on Excited State Properties of Exciton

The size and composition of semiconductor NC have profound effects on the excited state properties of exciton. It is clear that the transition from the microcrystalline to the nanocrystalline state of the semiconductor opens up new possibilities for controlling the characteristics of these substances by size modification.

Size effects are observed in semiconductor crystals measuring 10-100 nm, whereas quantum size effects are usually characteristic of nanocrystallites measuring less than 10 nm. The semiconductor QDs show a quantum-size dependent color emission due to quantum confinement effects, which covers almost the whole visible range. The most remarkable characteristic of a semiconductor NC is the ability to tune its optical and electronic properties by controlling its size. As it is mentioned in the previous chapter the surface area/volume ratio increases with the reduction of the size of semiconductors. From bulk-size to nano-size there is a huge difference between surface areas to volume ratio. The electronic structure of the NCs became completely different from that of bulk. By this increase in the ratio and so by nanosized surface, both the optical and electronic properties are strongly influenced. This phenomenon is a result of destruction as a result of radiative and nonradiative recombination, and reactions at the interface with reagents present in the solution, i.e., on the photophysical and photochemical processes, which together form the subject of photonics (Beard and Ellingson 2008).

The change of characteristics with change of size has a particularly strong effect on the interaction of the semiconductor NCs with the light wave. Its consequences on the absorption of light, the dynamics of photogenerated nonequilibrium charge carriers, the processes lead to a change in their heat capacity, the energy of the vibrations of atoms in the crystal lattice. Another consequence is a decrease in the temperature and entropy of fusion of the crystals on the range of $R < \text{exciton radius}$, and a change in magnetic characteristics, such as Curie temperature, the coercive force of the semiconductor (Stroyuk et al. 2005).

The absorption of light by semiconductor NPs with non-degenerate energy bands depends on the size of the gap between the permitted bands and the density of defect levels in the forbidden band. The first factor determines the position of the long-

wave edge of the absorption band of the semiconductor NP (λ_{tr}), and the second determines the form of the absorption band and its edge and the intensity of absorption in the region of energy of light ($h\nu$) $< E_g$. If $h\nu > E_g$ the absorption of light becomes continuous, forming one spectral band, the intensity of which increases regularly with increase in the quantum energy. Weakly doped semiconductors, characterized by structural perfection and low concentration of surface defects, hardly absorb light with $h\nu < E_g$ at all during direct band-band transitions. The absorption in this region may be due to the polydisperse nature of the semiconductor NPs or to the presence of structural defects capable of being ionized by light quanta with energy less than E_g on their surface (Ramsden and Grätzel 1984).

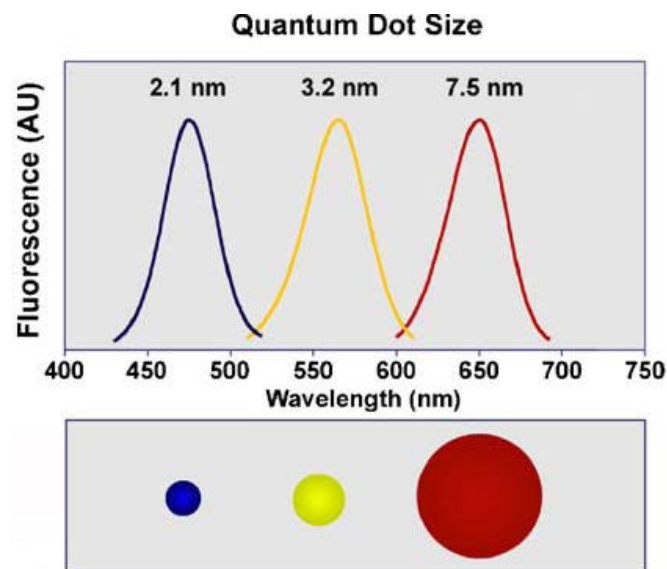


Figure 1.6. Tuning the QD emission wavelength by changing the nanoparticle size. The emission of a CdSe QD may be adjusted to anywhere within the visible spectrum (450–650 nm) by selecting a NP diameter between 2 and 7.5 nm. The relative sizes of these particles of constant composition are shown schematically below the fluorescence spectrum (Source: Bailey et al. 2004).

Emission requires that both an electron and a hole be present in the lowest excited state for radiative recombination. The excited electrons and holes generated directly within the core can immediately contribute to the emission process without needing to undergo interfacial charge transfer. The formed exciton is the energy entity and the size of exciton determines the color of the emission. The emission color shifts to red due to decreasing band gap of the crystal (Bailey et al. 2004). The emission of a CdSe QD may be adjusted to anywhere within the visible spectrum (450–650 nm) by selecting a NP diameter between 2 and 7.5 nm. The relative sizes of these particles of

constant composition are shown schematically in Figure 1.6. Semiconductor NCs exhibit composition dependent electronic and optical properties. By altering the chemical composition, fluorescence emission may be tuned from the near ultraviolet, throughout the visible, and into the near-infrared spectrum, spanning a broad wavelength range of 400–2000 nm in Figure 1.7 (Bailey et al. 2004, Zhong et al. 2003, Klimov et al.2004).

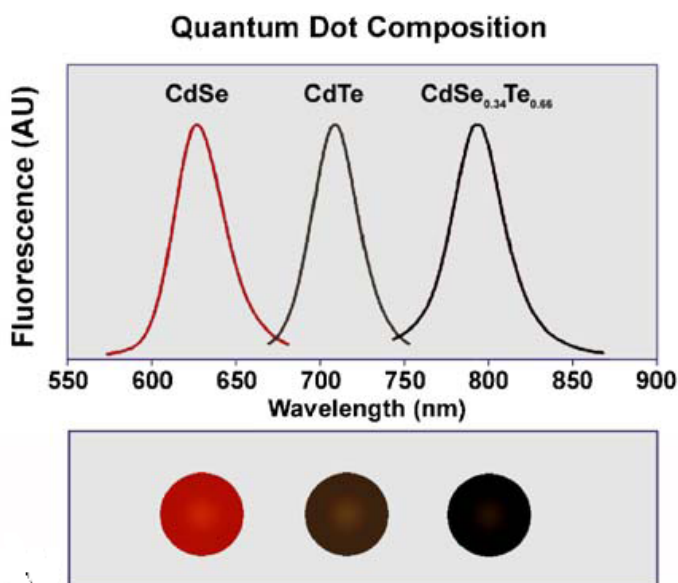


Figure 1.7. Tuning the QD emission wavelength by changing the NP composition. While keeping the NP size constant (5nm diameter) and varying the composition of the ternary alloy $\text{CdSe}_x\text{Te}_{1-x}$, the emission maximum may be tuned to any wavelength between 610 and 800 nm. (Source: Bailey et al. 2004).

The size-dependent band gap of semiconductor NCs is well-known and has been widely studied. Composition control of NCs is essential for band gap control for solar cell applications. Zhong et al. synthesized ternary $\text{Zn}_x\text{Cd}_{1-x}\text{Se}$ and $\text{Zn}_x\text{Cd}_{1-x}\text{S}$ alloyed NCs with luminescent properties comparable to or even better than the best-reported binary CdSe and CdS based NCs, respectively. The composition-tunable emission across the visible spectrum has been systematically demonstrated over the composition of the $\text{Zn}_x\text{Cd}_{1-x}\text{Se}$ NCs (the emission wavelength blue-shifts gradually with the increase of Zn content). The high luminescence efficiency and stability of the resulting alloy NCs are attributed to the larger particle size, higher crystallinity, higher covalency, lower inter-diffusion, and spatial composition fluctuation throughout the crystal structure (Zhong et al. 2003).

Type I NCs have a shell made of a wider band gap material over a smaller band gap core. In such QDs, the exciton is trapped within the core because the electron prefers to populate the lowest energy conduction band and the hole prefers the highest energy valence band available. The type design reduces *energy transfer* between QDs because the electron and hole are not near the surface. Type II NCs have two materials with similar band gaps and the electron-hole is separated into the core and shell individually. Type II design allow for a greater tuning of the band gap because both *the core diameter* and *the shell thickness* affect the electronic structure of the particle core/shell NCs with Type II may be a solution to the Auger recombination (Kemling 2007, Ivanov et al 2004 and Klimov et al. 2004).

For both type II (S/C) and type I (S/S) localization regimes electron resides in the shell. Energy band-edge transition and emission wavelength are determined by shell thickness and weakly depends on core diameter. Auger decay rates depend on overall extent of electronic wavefunction which is determined by total volume of hetero-NCs in the case of shell localized electron. The inverted core/shell NCs with large core and thick shell can be used to control the Auger recombination process will be highly suppressed (Klimov V. I. 2006). Auger recombination is inactive in Type-II hetero NCs that produce exciton exciton repulsion (Ivanov et al. 2004).

Efros A. L. explained that for for QDs the composition effect arises from a strong dependence of the electronic energies on the effective exciton mass (reduced mass of a coupled hole/electron pair) (Efros 1992).

In one study Bailey and Nie demonstrated that composition and internal structure are two important parameters that can be used to tune the optical and electronic properties of multicomponent, alloyed QDs by varying the relative amounts of the starting materials and nucleation temperature. All dots were synthesized to have a mean diameter of 5.9 nm (core plus shell).

As shown in Figure 1.8 the core-shell CdTe-CdSe NCs are intensely fluorescent (emission peak at 702 nm), but the reversed core-shell CdSe-CdTe QDs show little band-edge luminescence. This is because of that CdTe has a lower band gap than CdSe and does not provide an effective shell (leading to exciton recombination at surface trap sites). In comparison, both types of alloyed QDs are highly fluorescent, but their emission spectra are shifted to 741 nm for the gradient structure and to 757 nm for the homogeneous structure. Remarkably, the alloyed QDs exhibit similar fluorescence quantum yields ((QE) 30-60%) and spectral widths (full width at half-maximum or

fwhm = 35 nm) as the traditional core-shell dots (fwhm) 30-35 nm). The high quantum yields and narrow spectral widths indicate that the alloyed QDs do not contain a heterogeneous population of amorphous clusters but are highly crystalline in structure and monodisperse in size (Bailey and Nie 2003).

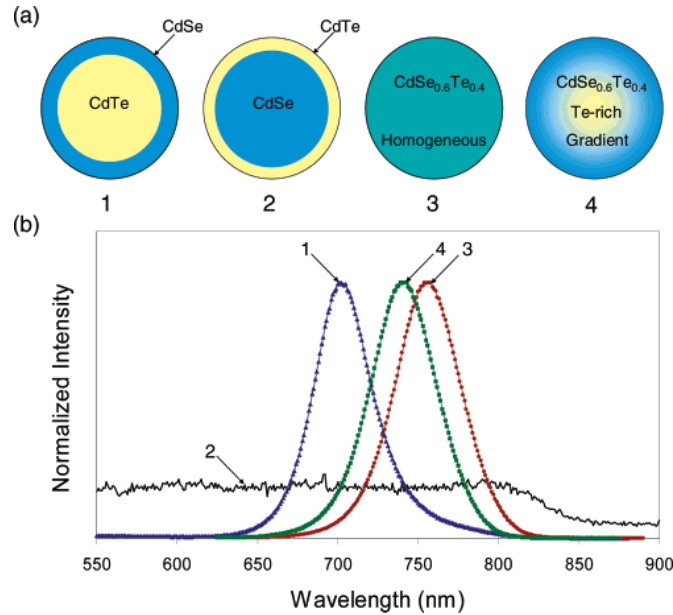


Figure 1.8. Internal structures and optical properties of core-shell and alloyed $\text{CdSe}_{1-x}\text{Te}_x$ QDs: (a) schematic drawings of four different types of QDs; (b) their corresponding fluorescence emission spectra. (1) Traditional core-shell CdTe-CdSe dots; (2) reversed core-shell dots; (3) homogeneous alloyed dots; and (4) gradient alloyed dots (Source: Bailey and Nie 2003).

In the same study Bailey and Nie synthesized 3 different series dots (a)-(c) (Figure 1.9) the binary dots and the alloyed dots (either homogeneous or gradient), having the same overall diameter. The fluorescence spectra obtained from three size series of CdSe, CdTe, and $\text{CdSe}_{1-x}\text{Te}_x$ QDs are shown in Figure 1.8. In the 3.5-nm size series, the gradient alloyed dots emit fluorescent light 145 nm longer than the binary CdSe dots and 50 nm longer than the binary CdTe dots. In the 5.0-nm and 6.5-nm size series, the emission spectra of the homogeneous alloyed dots are red-shifted to ca. 800 and 825 nm, respectively. The emission wavelength of the largest CdTe dots (5.5 nm) is expected to be 730 nm, still shorter than the emission peak (780 nm) of the smallest $\text{CdSe}_{0.34}\text{Te}_{0.66}$ dots (4.5 nm) (Bailey and Nie 2003). The differences between emission wavelength of such kind of alloys and that of the binary alloys are due to a nonlinear relationship between the bandgap energy and the composition.

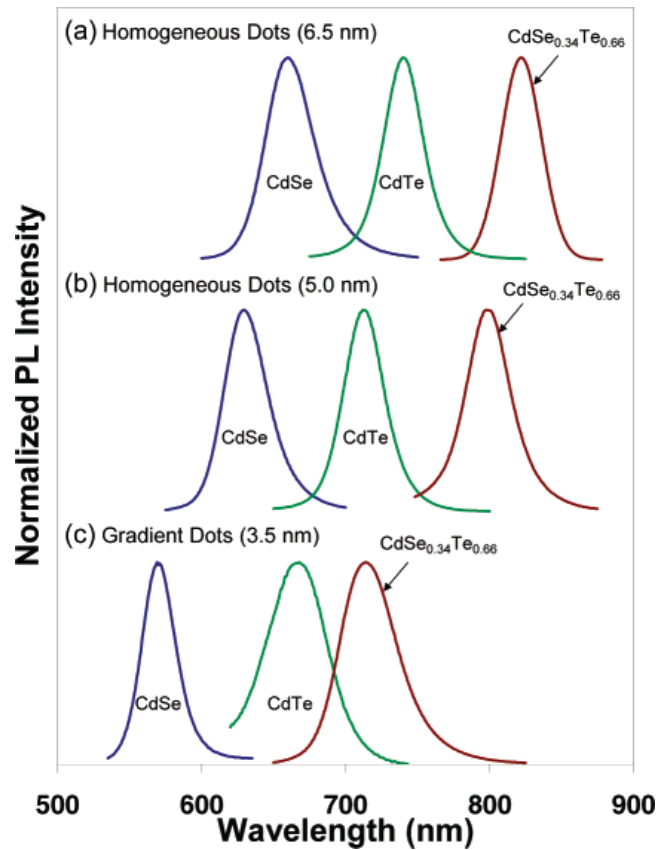


Figure 1.9. Comparison of the emission spectra among CdSe, CdTe, and CdSe_{0.34}Te_{0.66} QDs at three particle sizes (Source: Bailey and Nie 2003).

The composition, type of core-shell materials and thickness of the shell material are important parameters that affect the Auger life time. They affect confinement regime. Klimov studied on hetero-NCs, in which a core of a wide gap semiconductor, ZnSe, was over-coated with a shell of a narrower gap material, CdSe. The inverted NC provides new capabilities for controlling functionalities by direct control of the distribution of electron and hole wave functions and the e-h overlap integral compared to monocomponent NCs or traditional “noninverted” hetero-nanostructures, CdSe(core)/ZnS(shell) or CdSe(core)/CdS(shell), (Kim et al. 2003). Klimov explained that by increasing the thickness of the NC shell (for a fixed NC core size), one can continuously tune the carrier localization regime from type-I for thin shells to type-II for intermediate shells and finally back to type-I for thick shells (electron and hole co-localize in the shell) (Klimov I.V. 2006).

1.7. Characterization of Nanocrystals

Characterization of nanoparticles can be divided into two as optical characterization and structural characterization.

1.7.1. Optical Characterization

The spectral properties of the nanoalloys were measured at room temperature by using Varian Cary 50 UV-Vis, and Varian Cary Eclipse fluorescence spectrometers. Photophysical characterization of the NPs will be done by UV-Vis Absorption and Fluorescence Spectrophotometer. Absorbance or optical density is basically a logarithmic ratio of initial radiation to transmitted radiation through the material and absorbance of NPs directly proportional with their concentration, their extinction coefficient and length of the light path. NPs arise as Gaussian shaped peaks both in Fluorescence and UV-Vis Spectrophotometer. NPs that have absorbed light emit photons (fluorescence) at different wavelengths. Generally, the fluorescence emission wavelength shifts to longer wavelength compared to the absorption wavelength.

Under absorption of light, an electron is excited from valence band (ground state) to energy levels of conduction band (excited state) and the absorption is followed by a very fast nonradiative vibrational relaxation process, which brings the electron to the lowest excited state in conduction band. This process can be followed by fluorescence emission—the system emits photon and relaxes to the ground state in valence band. The trap states within band gaps of NCs can be alternative pathways of exciton relaxation. Figure 1.10a represents pathway of absorption, relaxation and emission process.

Absorption and fluorescence spectroscopic analysis are non-destructive and much information could be obtained from the techniques. Gaussian shaped peaks both in Fluorescence and UV-Vis spectra can be used to follow size, size distribution which is related with defective states in crystals and growth of the crystals. As NCs grow, peaks in the spectra corresponding to the crystal are red-shifted. By reducing the particle size, absorption shifts to higher energies and different allowed possible transitions results in different discrete bands due to the size dependent quantum confinement. At longer wavelength, broadening in the peaks can be observed for

particles consisting of surface defect states, and this leads to quenching of the band gap emission and appearance of weak deep trap long-wavelength emission.

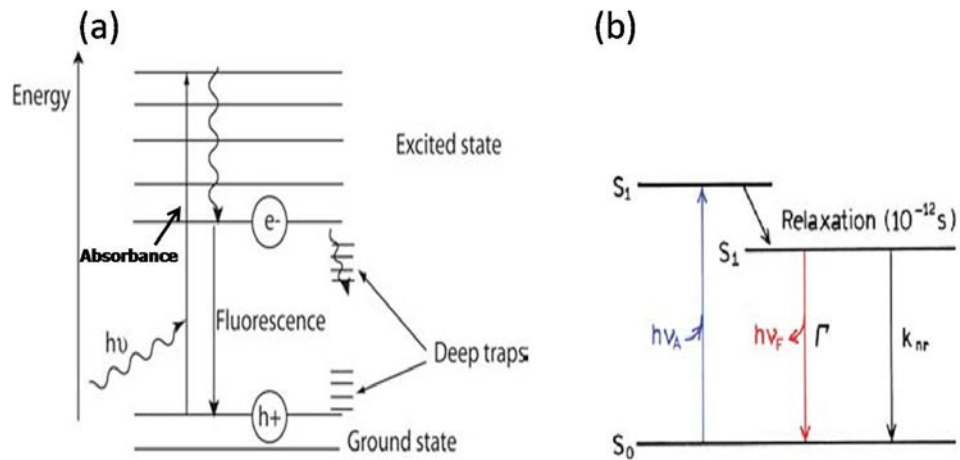


Figure 1.10. (a) Schematic path for absorption of light, vibrational relaxation and fluorescence emission or relaxation through trap states (Source: Klimov et al. 2000), (b) Simple representation of Jablonski diagram (Source: Lakowicz 2006).

The spectra provides information about stokes shift which is the difference between band maxima of fluorescence and absorbance of the same electronic transition. This difference is the result of a combination of relaxation into deep trap states and the size distribution which is related with defect and size of particles. Stokes shift ($\Delta\nu$) can be found with the formula;

$$\Delta\nu = \nu_{\text{absorbance}} - \nu_{\text{fluorescence}} \quad (1.5)$$

The width of the emission peak, typically reported as the full-width-at-half-maximum, is generally used to appraise the particle size distribution and so the emission spectra represent size distributions of individual emissions.

The excitation of an electron in a semiconductor nanocrystal by a photon eventually results in a loss of energy as the electron returns to the ground state from an excited state. This loss of energy (deactivation) can either be manifested as fluorescence (emission of light) non-radiative heat to the surroundings, or some other deactivation process. The ability for a NC to emit the photons it has absorbed is described as quantum efficiency. Basically, photoluminescence quantum efficiency (PLQE) is the

ratio of the number of emitted photons to the number of absorbed photons (Fery-Forgues and Lavabre 1999).

PLQE–fluorescence quantum yield - can be calculated by absorption spectra and fluorescence emission spectra. Experimentally, fluorescence quantum yield of an unknown sample can be determined by comparing fluorescence of both unknown substance and a dye of known quantum yield. Generally fluorophore is used as a standard dye with a well known quantum yield for comparison. It is important to choose the proper dye for the calculation. Absorption and PL spectra of the standard dye should overlap with absorption and PL spectra of the NCs. The quantum yield is then calculated by

$$\Phi = \Phi_R \times \frac{Int}{Int_R} \frac{A_R}{A} \frac{n^2}{n_R^2} \quad (1.6)$$

where Φ is the quantum yield, Int is the area under the emission peak (on a wavelength scale), A is absorbance at the excitation wavelength, and n is the refractive index of the sample. Φ_R , A_R and n_R are quantum yield, absorbance at the excitation wavelength and refractive index of reference, respectively.

Quantum yield can also be defined as the ratio of radiative and non-radiative processes as shown in equation below. The k_r and k_{nr} are the rate constants of radiative and non-radiative processes of the sample, respectively (Fery-Forgues and Lavabre 1999) and the processes are schematically represented in Figure 1.10b.

$$QY = \frac{k_r}{k_r + \sum k_{nr}} \quad (1.7)$$

1.7.2. Structural Characterization

Structural characterization of synthesized semiconductor QDs can be carried out by using X-Ray Diffraction (XRD), Dynamic Light Scattering (DLS) technique, Inductively Coupled Plasma-Mass Spectroscopy (ICP-MS), Inductively Coupled Plasma-Atomic Emission Spectroscopy (ICP-AES) Scanning Transmission Electron Microscopy (STEM), Scanning Electron Microscopy-Energy Dispersive X-Ray

Spectroscopy (SEM-EDS), and Transmission Electron Microscopy (TEM). X-ray diffraction (XRD) technique is one of the non destructive techniques and is used to reveal information about the chemical composition and crystal structure of the NCs. The technique is based on observing the intensity of scattered X-Ray beam which hits the sample. The lattice constants and geometry of crystal structure will be obtained. By comparing hkl indexes of bulk and nano structures, unknown crystal structure and size can be determined.

X-rays are produced by collision of a high speed electron with a metal target under a high voltage system. Produced X-ray beams fall on a specimen, and then they are diffracted by the crystalline phases in the specimen according to the Bragg's law shown in equation 1.8.

$$n\lambda = 2d \sin \theta \quad (1.8)$$

where n is the order, λ is the wavelength of X-rays, d is the inter-planar spacing between planes in the atomic lattices and θ is the angle between the incident beam and the scattering plane. Average crystallite size of the particles can be calculated by using X-ray diffraction pattern with applying Debye Scherer's equation shown below (Equation 1.9)

$$D = \frac{0.9\lambda}{B \cos \theta_B} \quad (1.9)$$

where D is the diameter of the crystals, λ the wavelength of the incident X-rays, B is the full-width at the half-maximum of the Bragg peak, and θ_B is the diffraction angle.

The compositions of alloy type crystals having homogeneous inner structure can be estimated from XRD-pattern by applying Vegard's law (Equation 1.10);

$$a_{Zn_xCd_{1-x}Te} = x.a_{ZnTe} + (1-x).a_{CdTe} \quad (1.10)$$

where $a_{Zn_xCd_{1-x}Te}$ is unitcell parameter of $Zn_xCd_{1-x}Te$ NCs, x is mole fraction of Zn inside the alloy NC, a_{CdTe} and a_{ZnTe} are the unitcell parameter of bulk CdTe and bulk ZnTe NCs, respectively.

The unit cell parameter, $a_{Zn_xCd_{1-x}Te}$, can be calculated by using the most intense peak in XRD diffraction pattern, with the help of equation (1.11), where n is 1, λ is 1.54

nm (CuK α radiation); θ is the angle of most intense diffraction peak, and h, k, l are the Miller indices of the diffracted plane.

$$a = \frac{n\lambda}{2 \sin \theta} \sqrt{h^2 + k^2 + l^2} \quad (1.11)$$

X-ray powder diffraction patterns of the NCs were obtained by using a Philips X'pert Pro Materials Research Diffractometer. The grounded samples were placed on a zero-background silicon sample holder. Data was collected by using CuK α ($\lambda = 1.5406$ Å) radiation at settings of -45 kV and 40 mA for 45 minutes. The scan rate was 0.1°/sec and the data was collected for 2θ values of 5 to 70°.

Electron Microscopy is a very useful technique capable of providing structural information over a wide range of modification. The Scanning Electron Microscope (SEM) gives information about the texture topography and surface features of powders or solid pieces by using electrons rather than light to form an image. Features up to tens of micrometers in size can be seen because of the depth of focus of SEM instruments. The resulting pictures have a definite 3-D quality. The resolution of SEM is approximately between 100 Å and 10 μ m. On the other hand Scanning Electron Transmission Microscope (STEM) can be used to get information about the size and the shape of the NCs due to its higher resolution compared to SEM.

The most common accessory equipped with a SEM is the energy dispersive X-ray detector, EDX. This type of detector allows a user to analyze a sample molecular composition. The ideal specimen for EDX microanalysis is perfectly flat and polished. Elemental composition of the NCs can be analyzed by SEM-EDX. The results of EDX analysis are usually presented as a spectrum. In this graphical representation the x -axis represents the energy level—and therefore identifies the elements, and the y -axis provides the number of counts for each element detected. Philips XL 30S FEG Scanning Electron Microscope and Scanning Transmission Electron Microscopy at IYTE-MAM were used for the elemental analysis.

Transmission Electron Microscope (TEM) is most commonly used technique to analyze the NCs morphology, because objects can be seen in the order of a few angstroms. In TEM, electrons are used as light source, because their lower wavelength makes it possible to get a better resolution than a light microscope. TEM uses a beam of electrons to pass through the crystalline sample. A light source emits electrons then they

travel through vacuum in the column of the microscope. Electromagnetic lenses are used in TEM to focus the electrons into a very thin beam; this beam then travels through the specimen. The unscattered electrons hit a fluorescent screen at the bottom of the microscope and depend on the density; different parts of the specimen can be displayed in varied darkness. A detector collects the electrons and an image is formed, magnified and viewed on a phosphor screen which is coupled to a digital camera for viewing. The observed image can be photographed with a camera. Transmission Electron Microscopy (TEM) at UNAM / Bilkent University was used to analyze the NCs. TEM images were obtained with a Zeiss 912 Omega microscope working at a voltage of 120 kV and a Technai F20 microscope working at a voltage of 200 kV SFEG.

Dynamic Light Scattering (DLS) measurements are also another technique to measure the size of NCs. Generally, the sizes measured from DLS were bigger than the results obtained from TEM or STEM. It is expectable because TEM measures the hard core of the NCs but DLS measures both the hard core and the hydrodynamic diameter of the NCs (Qian et al. 2007). DLS measurements were performed by Malvern Zetasizer Nano ZS.

Compositional analysis can be carried out by Inductively Coupled Plasma-Mass Spectrometry (ICP-MS) which is a kind of mass spectrometry and Inductively Coupled Plasma- Atomic Emission Spectroscopy (ICP-AES). Difference of ICP-MS from ICP-AES is that in ICP-MS metals at the lowest concentrations could be separated by mass spectrometer whereas in ICP-AES separation of the ionized sample is done by Atomic Emission Spectroscopy. Compositional analysis was done by Agilent 7500ce Inductively Coupled Plasma/Mass Spectrometer and Varian ICP 96 model Inductively Coupled Plasma Atomic Emission Spectrometer.

PTI-QM1 fluorescence spectrophotometer equipped with Pico quant time-correlated single photon counting board-card was used for fluorescence decay measurements.

CHAPTER 2

SYNTHESIS AND CHARACTERIZATION OF WATER DISPERSIBLE CdTe AND CdTe/CdS SEMICONDUCTOR COLLOIDAL NANOCRYSTALS

2.1. Introduction

Semiconductor nanocrystals (NCs) are widely used in technological applications because of their unusual and tunable optical properties. Various types of NCs were prepared with different synthesis methods as mentioned in Section 1.6. Depending on their size and composition, NCs emit light at different wavelengths in the electromagnetic spectrum. The CdTe and CdTe/CdS semiconductor NCs have been subject of numerous investigations due to high quantum efficiency, multicolor availability and easy to control of synthesis. CdTe and CdTe/CdS NCs have applications in solid-state emitting, displays, solar cells, communications, sensors, and in biological imaging areas.

Although synthesis of core shell NCs via hot injection organometallic approach based on the high-temperature thermolysis of the precursors is very common and successful, this method has high costs and requires rigorous experimental conditions (Allen and Bawendi 2008, Kim, Park, and Jang 2010). The NCs synthesized by organometallic approach have high quantum efficiencies, but applications of the NCs are restricted because the NCs are unstable in the air. Recently, direct synthesis of CdTe core and CdTe/CdS core/shell NCs in water by using short chain thiols, for example 3-MPA or TGA (Figure 2.1) as stabilizing agent provides useful, easy and environment-friendly synthetic route compared to organometallic route (Mekis et al. 2003). Direct synthesis in water is reproducible, less expensive and less toxic. By using of thiols it is possible to control the kinetics of the nanocrystal synthesis, passivate surface dangling bonds resulting in reduction of nonradiative Auger processes, and provides stability, solubility, and surface functionality of the NCs (Rogach et al. 2007). CdTe NCs are preferred because of easy fabrication and high quantum yield in aqueous media (around

40%) (Gaponik et al. 2002). By coating CdTe core with CdS shell, it is possible to obtain even higher QYs (around 70%) (Gu et al. 2008). In this chapter the synthesis and characterization of TGA (thioglycolic acid) -capped CdTe core and CdTe/CdS NCs are presented. Due to lack of stereo-hindrance effect of TGA, this will cause less passivation of the NC surface, so we select TGA as the stabilizer. Using thioglycolic acid (TGA) -like stabilizers is a best choice for our experiments.

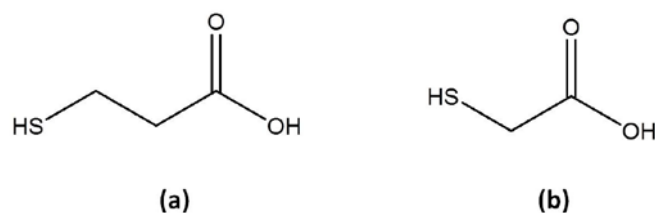


Figure 2.1. Structures of (a) 3 – Mercaptopropionic acid and (b) Thioglycolic acid

Room temperature photoluminescence measurements showed that the NCs gave emission between 520 to 630 nm in electromagnetic spectrum according to their sizes. In our study, we tried to optimize reaction conditions to synthesize CdTe and CdTe/CdS NCs having high QY. Thioglycolic acid that is capping agent non polar solvent was preferred because of its advantage in controlling the growth process of NCs with narrow size distribution and high crystallinity.

2.2. Experimental

The CdTe NCs were synthesized by one-pot approach and were grown to certain size. Then S precursor was added to coat CdTe core NCs by shell of CdS in order to increase the photostability of core/shell NCs.

All chemicals used were of the highest purity available. As a metal source Cadmium chloride (CdCl_2 , Fluka 99%) was used throughout the study. Thioglycolic acid; TGA ($\text{HSCH}_2\text{CO}_2\text{H}$, Merck 98%) was used as capping and distilled water used as solvent. Sodium borohydride (NaBH_4 , Riedel 95%), and Tellurium powder (Te, Fluka 99.9%) were used to synthesize Te precursor. Thiourea ($\text{CH}_4\text{N}_2\text{S}$, Aldrich 99.5%) were the S source for CdS shell formation. 2 propanol ($\text{C}_3\text{H}_8\text{O}$, Riedel 99.5%) was used to purify the NCs. All solutions were prepared using ultra pure water as a solvent.

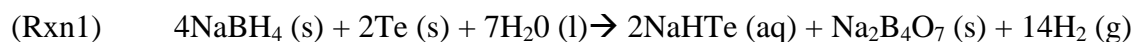
The synthesized NCs were characterized by UV-Vis Spectrometer and Fluorescence Spectrometer in terms of linear optical properties. Structural characterization of the NCs was done by X-Ray Diffractometer (XRD), Transmission Electron Microscopy (TEM), FT-IR and Atomic Force Microscopy (AFM). AFM can be used to determine size and size distribution of NCs. Sensitivity of AFM for size characterization is limited by the tip size. AFM can measure limited size and this leads to errors in analysis. Dynamic Light Scattering (DLS) instrument were used to follow the growth of NCs.

2.3. Synthesis

In a typical synthesis of CdTe nanocrystals, cadmium and tellurium precursors were prepared individually.

2.3.1. Preparation of Te Precursor

Sodium hydrogen telluride (NaHTe) was the Te precursor and it was prepared by the reaction where sodium borohydrate (NaBH₄) is oxidized by tellurium powder. Te powder (0.0918 g) and NaBH₄ (0.06 g) were put into 25 ml reaction flask and it was purged with N₂ for 30 min. Then 10 ml of distilled water was added to the reaction flask and the system was heated at 60 °C for 2 h under N₂ atmosphere to obtain a solution with a purple color. No other purification was performed. In all experiments, freshly synthesized NaHTe was used because NaHTe could be easily oxidized with air (Gu et al. 2008). The charge of Te changes from 0 to -2 as in the proposed reaction shown below;



2.3.2. Synthesis of CdTe Nanocrystals

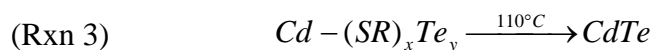
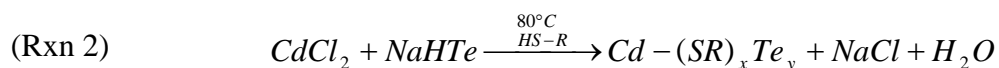
CdTe QDs are prepared by slightly changing the synthetic procedures reported in literature (Rogach et al. 2007 and Gu et al. 2008). 3.12 mmol CdCl₂ and 0.42 ml thioglycolic acid were dissolved in 110 mL of ultra pure water in two-necked flask with a septum. pH of the solution was adjusted to 11-11.5 by dropwise addition of 1 M of NaOH solution. Then the flask was attached to the condenser and the solution was deaerated by N₂ bubbling for an hour at 80 °C to purge oxygen in the medium (Figure 2.2).

While N₂ bubbling solution, temperature was set to 80 °C. The reflux time was one hour. Further reflux before the addition of Te²⁻ precursor may cause decomposition of thioglycolic acid to give S²⁻ (Rogach et al. 2007). Then 2.5 ml of freshly synthesized NaHTe (Te²⁻ precursor) was added to the solution and the reaction temperature was increased to 110 °C.



Figure 2.2. Photograph of experimental set up (two neck round bottom borosilicate reaction flask)

Formation and growth steps are proceeding upon reflux. As soon as the temperature reaches to 110 °C, aliquots are taken to observe the growth of the NPs by DLS. After 10 minutes, the color of solution was green under UV irradiation. The supposed mechanism for the NC growth is as follows:



CdTe NCs precursors are formed according to reaction 2 where $-(\text{SR})$ is $-\text{S}(\text{CH}_2\text{COOH})$. The formation and growths of the NCs are proceeding upon refluxing at 110°C under N_2 atmosphere. Growth of the NCs was followed by sampling aliquots at different time intervals. After reaching determined size, NC's growth was stopped by cooling the solution to the room temperature.

In order to get NCs of high quality, some optimization studies were performed. During the optimization the ratio of reactants, amount of solvent, reaction temperature, and reflux time were changed. The mole ratio of Cd:Te:TGA was varied from 2:1:10 to 33:1:67.

2.4. Synthesis of CdTe/CdS Core Nanoparticles

Drop wise addition of proper amount of S^{2-} into the solution of CdTe NCs as synthesized in water allows CdS shell to be grown in core and increases the photostability of the CdTe core structure. Thiourea (Figure 2.3) was used as S^{2-} source. It was dissolved in water under sonication and then added to the CdTe NC solution at 110°C under N_2 atmosphere. The shell structure started to grow in a few minutes. Aliquots of sample were taken at different time intervals and their optical properties were monitored by UV-Vis and fluorescence spectra. The reaction was stopped at desired time by cooling the solution. Formed NCs were precipitated by adding 2-propanol into the solution. Precipitation procedure was repeated several times to remove impurities from the crude solution (Gu et al. 2008).

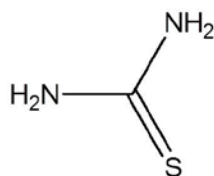


Figure 2.3. Structure of Thiourea

2.5. Results and Discussions

There are several techniques to control the morphology and the size of a semiconductor nanoparticle. The reactivity of Cd ions towards Te ions and the presence of TGA is the most significant effects to make nanometer-size cadmium based NCs. In the case of CdTe, loosely binding ligands such as thiols result in highly reactive Cd precursor and are known to grown in spherical zinc blende morphologies (Gu et al. 2008, Kim et al. 2003). Temperature and monomer concentration are among the important factors that can control the size. Upon injection of reactants, a certain initial concentration of monomers is formed, which will further react with each other to form nuclei. The nuclei react with the remainder of monomers to grow into particles. In order to obtain a specific crystal structure, the chemical potential (μ) of monomers has to be higher in energy than the potential of the nuclei's crystal structure. The chemical potential is a function of two variables, temperature and concentration: $\mu = \mu_0 + RT \ln(\text{activity})$. Thus, at any given time during the reaction, the monomer concentration determines the chemical potential of monomers and the nucleation type. Monomer concentration is governed by the reactivity of the precursors. The temperature of the reaction determines the equilibrium concentration of monomers. Changing the temperature has both thermodynamic and kinetic effects. It affects the relative chemical potential of the monomers and the already formed nuclei and particles. Many different temperature conditions have been studied in the literature (Chin et al. 2007, Kim et al. 2003, and Nonoguchi et al. 2007). Generally increasing the reaction temperature leads to the formation of more nuclei centers that run out of reactants faster, and therefore don't grow as large. Decreasing the temperature initiates formation of a smaller number of nuclei that have the chance to grow much larger before the reactants run out. To obtain the right monomer concentration for nucleation of a specific crystal structure concentration of precursors were varied and we worked between 80-110 °C.

Several parameters effective in the synthesis of CdTe were studied in detail systematically. The major tunable parameter in the synthesis is Cd:TGA. It was found that the relative amount of TGA to Cd precursor plays a pivotal role in the quality of synthesis. A TGA:Cd ratio of 6.05 mmol: 3.12 mmol is the optimum ratio for synthesizing monodisperse spherical core particles. The decrease in TGA amount from 2.4 ml (34.5 mmol) to 0.4 ml (6.05 mmol) leads to profound increases of the PL

intensity of the CdTe NCs (Figure 2.4). The quantum yield calculations also showed that PL quantum yield was increased approximately 50%. Upon further decrease in TGA amount it was seen that the PL intensity and PL QY of the CdTe NCs decreases.

The increase in the PL QY of CdTe NCs with the decrease in TGA amount was attributed to the increase in the relative concentration of Cd-S(CH₂COOH) complex formed at the stage of reaction 1. On the contrary, the decrease in PL QY of CdTe NCs with further decrease in TGA amount was because of lack of stabilizing agent to stabilize NCs from agglomeration. Rogach *et al.* also gave a plausible explanation for the competition of TGA and Cd amount (Rogach et al. 2007). They showed that upon decrease in TGA amount surface quality of NCs were improved due to decreasing possibility of formation of complexes between Cd and TGA. The decrease should have a limit because there should be enough TGA-stabilizer in solution to provide surface passivation of the growing NCs.

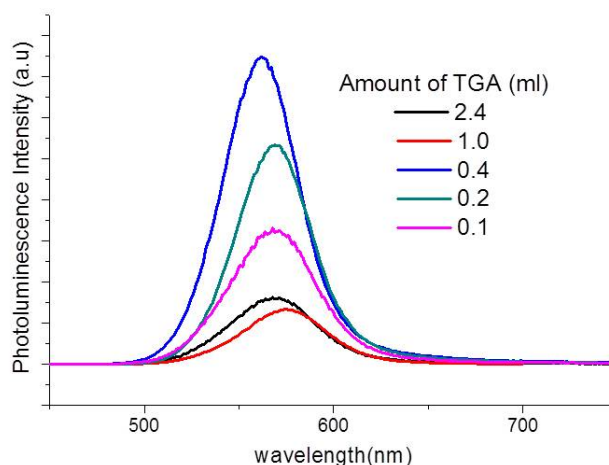


Figure 2.4. PL emission spectrum of CdTe NCs synthesized with different amount of TGA.

The pH of the solution was another factor that affects the PL QY of the TGA-capped NCs. The pH of the solution was adjusted between 11.0-11.5. In literature the pH was generally about 11.0 when TGA is stabilizer because at high pH the growth of the NCs was very fast. The result of the fast growth led to the formation of NCs with low QY. The relatively fast growth results in low crystallinity of the forming NCs, large amount of defects and trap states. When CdCl₂ and TGA are mixed in 110 ml of water, the solution was turbid. The turbidity was due to the domination of uncharged Cd-OH complexes. The turbidity of solution was removed by the addition of 1.0 M NaOH up to

reaching pH 11.0. At low pH, thiols have no ability to attach the NC surface. In the pH range between 7-10 $M(OH)_2$ is the metal species (M: Cd) and the complex have adsorption site to NCs, so NCs will easily precipitate. At $pH > 10$, $M(OH)^{3-}$ and $M(OH)_4^{2-}$ are the most possible species and they have no / less adsorption site to NCs (Zhang et al. 2003, Mandal and Tamai 2008, Xu et al. 2010). We worked at pH 9, 10 and 11. At low pH the particles grow faster and quantum yield of the particles are less than 10%.

The effect of concentration on reaction kinetics is significant. The core and core/shell NCs were synthesized in 110 ml of water. The reaction volume was reduced to half (110 ml to 55ml) in one of the syntheses. In the concentrated medium, the growth was very fast and the particles were finished growing into the reaction. Increasing the concentration by only a factor of two shortens the reaction time. The concentration affects the ion diffusion, and in concentrated medium; the diffusion of ions was restricted. Huge difference in Stokes shifts was the indication of the quality of NCs. Figure 2.5 compares UV-Vis and PL emission spectra of CdTe synthesized in concentrated (left) and diluted (right) water. 4.9 nm-sized NCs synthesized in 110 ml distilled water have PL maximum at ca. 576 nm and possesses a full width half maximum (FWHM) of the PL band of 50 nm. PL QY of the NCs is about to 23% and Stokes shift was about 30 nm.

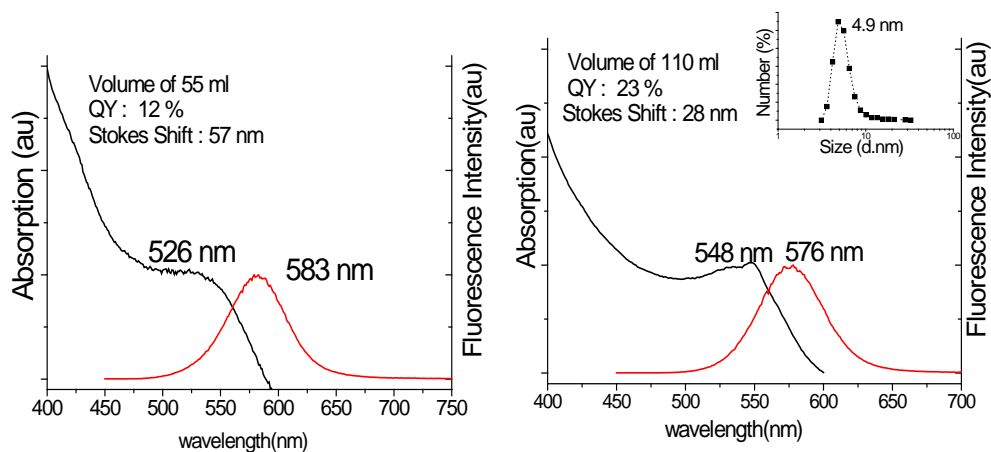


Figure 2.5. PL emission and UV-Vis spectra of TGA-capped CdTe synthesized in concentrated medium 280 min (left) and dilute (right) medium within 370 min. The insert on the right figure shows the size of CdTe NCs measured by DLS.

CdTe NCs synthesized in water can be isolated by the precipitation of the colloidal solution with proper solvents. For this process, precipitation was performed with four different solvent in centrifuge. After centrifugation, supernatants are extracted and resulted precipitates were left to dry at room temperature. The dried NCs can be stored after saturation with an inert gas at refrigerator for months. During purification process, the used solvent affects the surface properties of the particles. In the study 2-propanol was chosen as purifying solvent. In literature, generally ethanol was used for purification but with our crystals ethanol showed general solvent effect in which PL peak position show shifting (Gaponik et al. 2002 and Rogach et al. 2007).

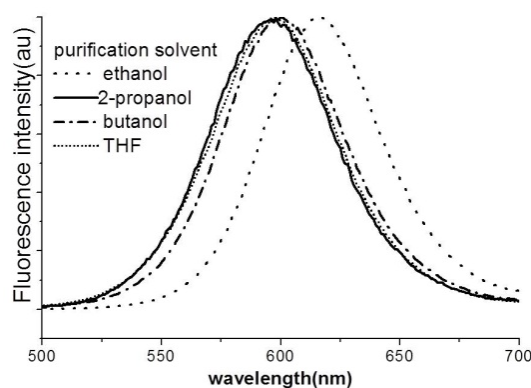


Figure 2.6. PL emission spectra of TGA-capped CdTe purified with different solvents.

Figure 2.7 shows PL emission and UV-Vis spectra of green and orange light emitting TGA-capped CdTe NCs synthesized under optimized condition. At the nucleation stage after the injection of the NaHTe to the colorless Cd precursor solution at 80 ° C, no luminescence was observed. Upon heating to 110 °C, about 15 min, the color of the colloidal solution becomes light brown under day light and the solution emits weak green PL under UV light. The emission shows the growth of CdTe NCs. The particles may grow if reaction is allowed to continue. Growth of CdTe NCs having PL emission continued for more than 10 hours and it is time dependent. Further reflux more than 10 hours leads to formation of NCs having no PL emission.

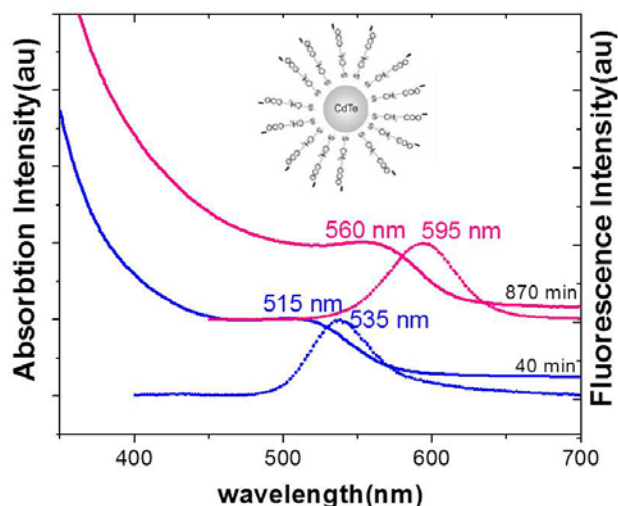


Figure 2.7. UV-Vis and PL emission spectra of TGA-capped CdTe. Insert: Scheme of TGA-capped NCs

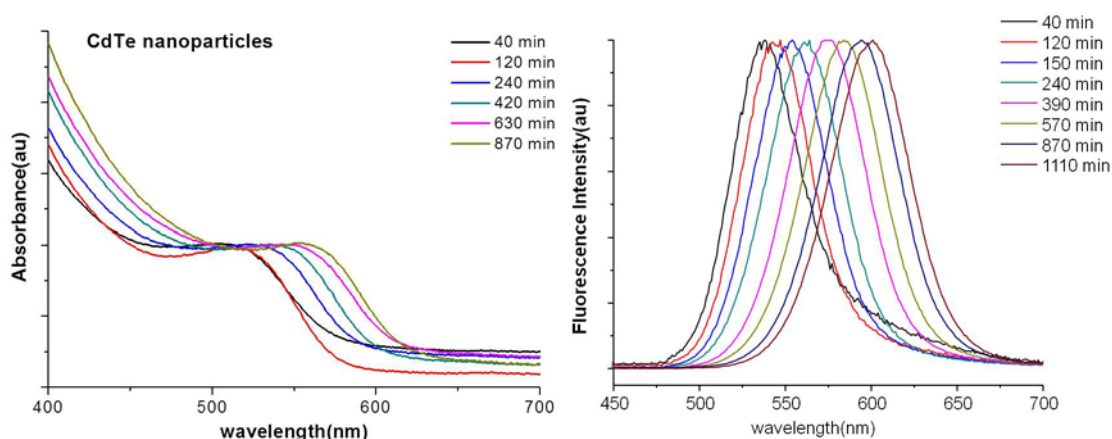


Figure 2.8. Normalized (a) absorption and the corresponding (b) emission spectra of CdTe NCs during growth. The reaction time is indicated in the figure. The excitation wavelength for PL measurement was 400 nm.

Figure 2.8 shows the normalized UV-Vis and PL emission spectra of CdTe in various growth times. It can be seen that both absorption and emission peaks of CdTe NCs continuously shift to higher wavelengths with a prolonged reaction time. The prolonged reaction time is necessary to reach a certain particle size. The absorption maximum of CdTe NCs shifts from 500 nm to 580 nm and the PL peak positions shifts from 520 nm to 635 nm within 1200 min. The shifts to longer wavelengths are due to quantum confinement. The emission color of CdTe NCs under UV light was varied from green to red. The difference between UV-Vis and PL peak position (Stokes shift)

is due to the inhomogeneous broadening which affects the absorption spectra to the greater degree than the emission spectra. The bandwidths of CdTe whose emission peaks are at different wavelengths can be calculated by measuring FWHM. The FWHM of CdTe NPs becomes broader as NPs get bigger. The FWHM of reddish-orange emitting particles is about 55 nm and the result is consistent with literature (Rogach et al. 2007). The FWHM values, as low as 20 nm being increased up to 55 nm for the bigger NCs. The average FWHM is about 50 nm and it shows that the sizes of the NCs are highly monodisperse. Energy of valence band (E_{VB}) of NPs can be determined from UV-Vis spectrum of NP by cutting wavelength axis by extrapolating first excitation peak in spectrum. E_{VB} of NCs varied 2.1eV to 2.4eV, respectively. The quantum yields of the particles are between 25-30%. Figure 2.9 shows the growth kinetics of CdTe NPs. At first, the growth rate of the particles is faster but when the particles become larger, the growth rate slows down. The slowing down shows that the NC size approaches the exciton size and the degree of quantum confinement decreases.

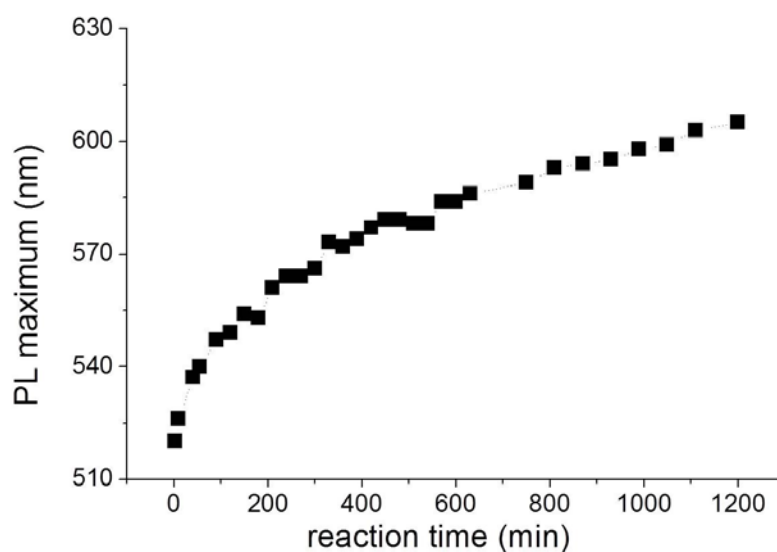


Figure 2.9. PL emission maximum as a function of reaction time.

Quantum dot synthesis can be considered as crystal growth in nanoscale. XRD was used to determine the crystal structure of NCs. Figure 2.10 represents the X-ray diffraction pattern of CdTe NCs. The crystal structure of CdTe NCs was estimated to be zinc blende by the diffraction angles (2θ) (Gu et al. 2008, Pan, et al. 2007). A zinc blende unit cell is defined by the a-axis lattice parameter. Geometrical considerations show that tetrahedral coordination is favored in ionic binary compounds having

cation/anion radius ratio between 0.225 and 0.732, while octahedral coordination is favored for a ratio greater than 0.732 (Brown I.D. 1988). In CdTe, the cation/anion radius ratio is $r(\text{Cd}^{2+})/r(\text{Te}^{2-}) = 0.444$, thus favoring tetrahedral coordination. CdTe can be grown with either spherical, tetrapod, or rod morphologies and the spheres are zincblende (Manna et al. 2003 and Shieh et al. 2005). Three XRD peaks centered at 2θ angles of 23.93, 40.27, and 46.28 are in consistent with the literature (Rogach et al. 2007, Gu et al. 2008, Pan, et al. 2007).

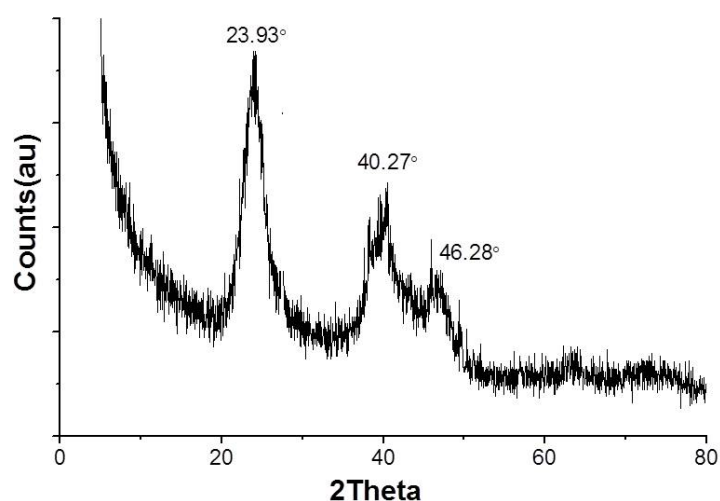


Figure 2.10. XRD pattern of TGA stabilized larger size CdTe NCs (PL emissions wavelength 635 nm)

TGA-capped CdTe NCs with 25% quantum yield have been synthesized by using 3.12 mmols Cd^{+2} , 2.5 ml Te precursors and 420 microliters of TGA. To increase the photostability of the NPs, CdTe NCs were coated with CdS shell. CdS is in principle a good candidate as the shell material for the CdTe core. CdTe/CdS heterostructures are relatively easier to synthesize due to the low lattice mismatch between them. The band gap of CdS (2.5 eV) is much wider than that of CdTe (1.5 eV) and the lattice parameter mismatch (3.6%) to CdTe which is relatively small compared with ZnSe (12.5%) and ZnS (16.5%) (Hines, M. A. and Guyot-Sionnest, P. 1996 and Trindade et al. 2001).

As afore mentioned Thiourea was used as S source. To see the influence of the amount of thiourea on photophysical properties of core/shell NCs, different amount of thiourea was injected to the CdTe NCs. Amount of thiourea was changed relative to amount of Te. The highest quantum yield which is 45% was obtained when the ratio of Te: S was 1:10. The growth was slow compared to that of CdTe NCs. For other cases in which the Te:S ratios were 1:20, 1:3, and 1:1 the red shift in PL wavelength was

increased significantly. The higher growth rate hinders the control over the crystal formation. Temporal evolution of fluorescence maxima of CdTe/CdS core/shell NCs with different amount of thiourea is shown in Figure 2.11

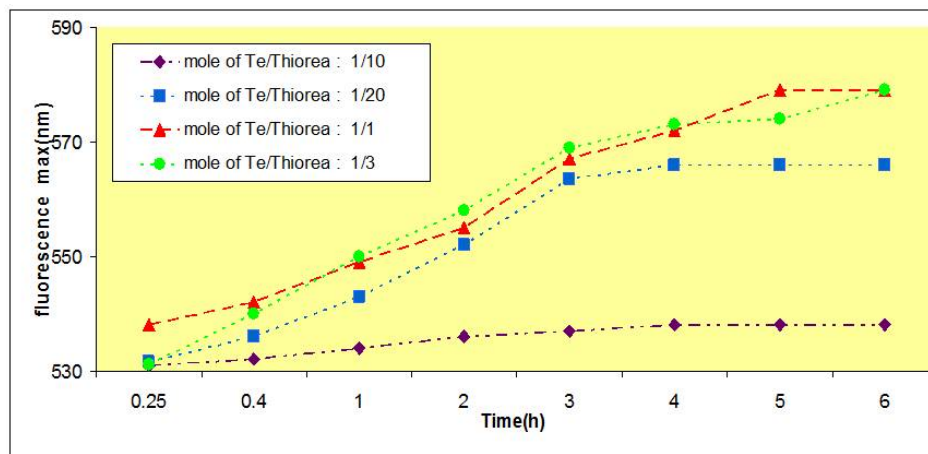


Figure 2.11. Growth kinetics of CdTe/CdS core/shell nanoparticles

Sulfur precursor solution was injected to the green emitting CdTe NCs. Figure 2.12 illustrates procedure for CdS coating on core type NCs schematically.

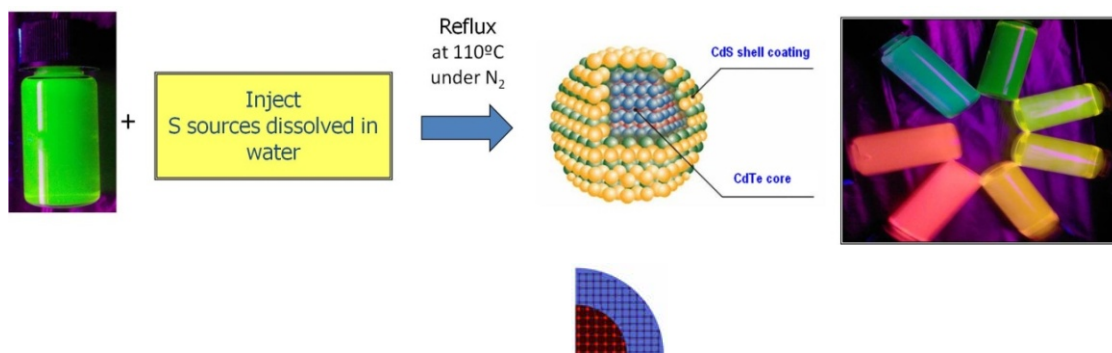


Figure 2.12. Schematic illustration of synthesis of CdTe/CdS core shell nanocrystals.

Thiourea releases sulfur to form CdS shell around CdTe core resulting in enhancement of the PL efficiency. Coating of CdTe NCs with CdS shell greatly inhibits the oxidation of CdTe core. Prolonged reaction time results in red-shifted UV-Vis and PL peak maximum due to increase in size of core/shell NCs. The UV-Vis and the PL spectra of CdTe/CdS are shown in Figure 2.13. The red-shift upon shell growth is the

result of a decrease in energy of excitons in the CdTe/CdS NPs due to the spreading of their wave functions into the CdS shell (Peng et.al 2007). The shifting upon coating is also another indication of core/shell structure formation rather than CdTe_xS_{1-x} alloyed structure. CdTeS alloy structure has larger band gap energy than CdTe and the alloy formation will cause blue-shifting rather than red-shifting. But we observed red-shift in both UV-Vis and PL spectra.

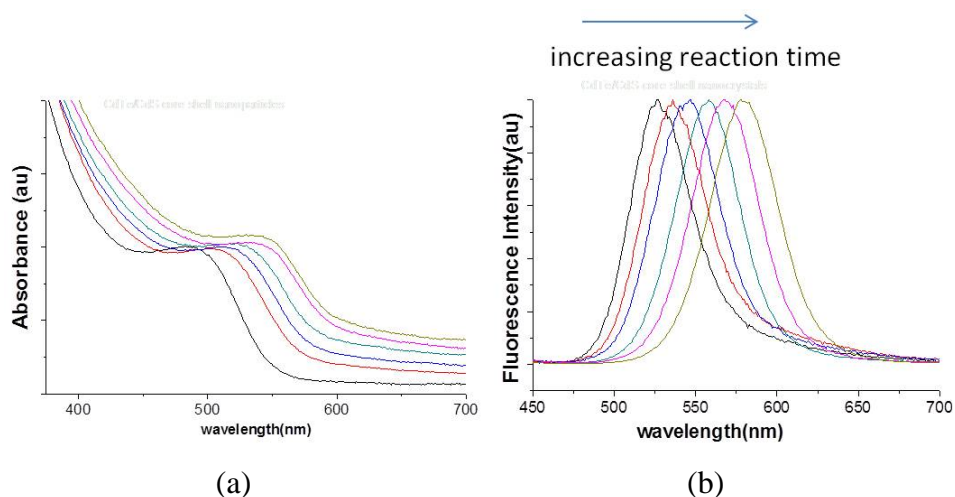


Figure 2.13. Normalized (a) UV-Vis and the (b) PL emission spectra of CdTe/CdS core shell NCs obtained after optimization (Te/S: 1/10).

The PL emission wavelengths of CdTe/CdS NCs are tunable from 525 nm to 630 nm in 24 hours. The PL FWHM, which is related to the particle size distribution, was about 60 nm. With a prolonged reflux time the size of particles increased. At the same time further reflux results in decreasing in quantum efficiency of the NCs from 45% to 27%. The decrease is possibly due to dislocations and new defects that were formed with further growth of CdS. The 3.6% lattice mismatch between CdTe and CdS results in defects and new source for nonradiative recombination sites.

Figure 2.14 shows the photographs of aqueous solution of different sized CdTe/CdS core/shell QDs under normal room light and under UV light. The luminescent colors varied from green to red. From left to right the sizes of the NCs are increasing. Highest quantum yield (45%) belongs to orange color emitting CdTe/CdS core shell NCs. The QY of the particles also diminishes with increasing number of shells. The QY increased with the initial CdS shell, probably due to the fact that the first shell passivates the surface of an already emissive core particle and suppresses nonradiative processes. Thicker shell creates surface trap states.

Sample purifications were carried out exactly like the cores. More than 2 times purification leads to decrease in the quantum yield of the particles by ~40%. The 3rd and 4th purification destroy the surface of the NCs drastically. Excessive use of 2-propanol (more than 40%) in the precipitation procedure strips off any ligands leaving the surface of the particles exposed and can cause irreversible agglomeration or surface oxidation. Crude solution of the core shell NCs are highly photostable. For further usage the NCs should be stored as the sample as is. After purification and redispersing in proper buffer solution having same pH with crude solution they still emits light.

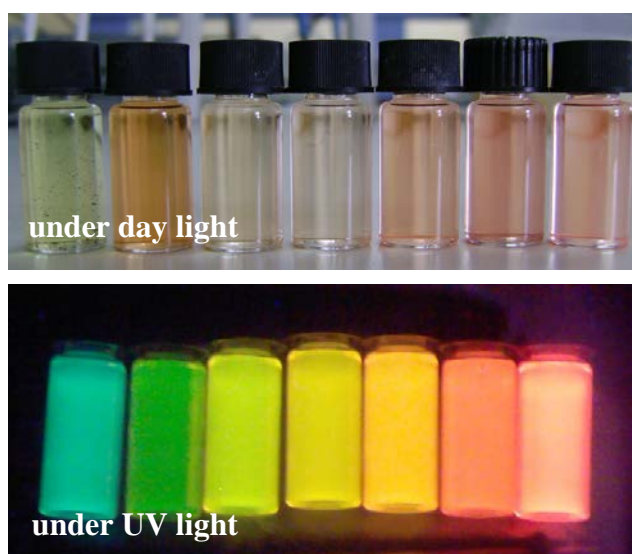


Figure 2.14. Luminescence image of CdTe/CdS NCs under day and UV light.

The formation of the CdS shell is further supported by XRD investigations. Figure 2.15 shows XRD pattern of four different sizes of CdTe/CdS NCs. The characteristic XRD pattern of CdTe and CdS bulk crystals are also seen in the bottom and top of the figure respectively. The small sized CdTe/CdS core/shell NCs exhibited a diffraction pattern quite close to that of bulk cubic CdTe. The dominant structure of small sized core shell NCs is the CdTe crystal phase. In contrast, the diffraction pattern of the larger sized CdTe/CdS NCs slightly moves toward higher angles with peak widths and shapes being nearly unchanged, which is close to the diffraction peak of cubic CdS. Our results are similar to the changes observed in literature (Gue et al. 2008, Rogach et al. 2007, Peng et al. 2007). The crystal structure of CdTe/CdS NPs is zinc blende type. The XRD pattern of the core shell NCs shows general pattern of the cubic lattice and the diffraction peaks shifts to larger angles and located between the the cubic

CdTe and CdS crystals. The midlocation between the CdTe and CdS phase is the indication of CdS shell formation. In literature similar changes were reported for the core shell NCs (Gu et al. 2008, Peng et al. 2007). The XRD diffraction peaks of 2.3 nm sized NCs are broad compared to that of NCs of 6.6 nm size. The broad nature of the peaks is attributed to the smaller size.

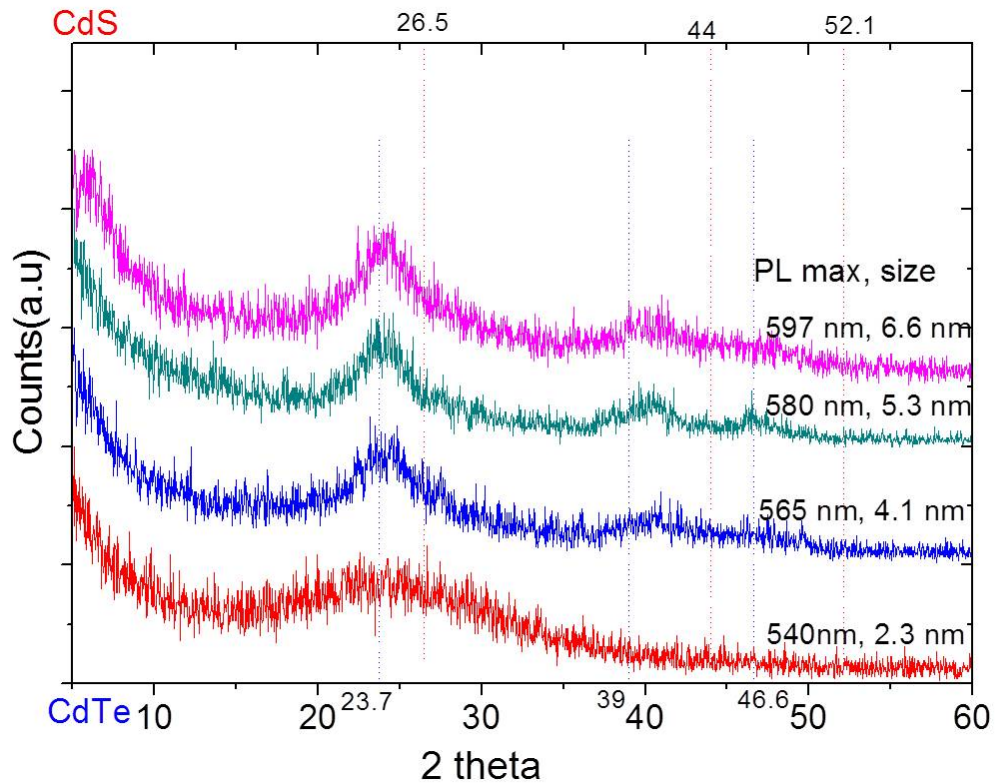


Figure 2.15. XRD pattern of different sized CdTe/CdS NCs, the lines representing blue lines show 2 theta of face centered cubic bulk CdTe (bottom), the dot red lines represent the 2 theta of face centered cubic bulk CdS (top). NCs have zinc blend structure. PL peak positions and the size of the NCs are also given inside the figure. The given sizes were obtained by DLS.

The CdTe/CdS core/shell NCs were analyzed by AFM, SEM-EDX and, ICP-MS analysis techniques. AFM (Figure 2.16) images of the NCs show that the obtained particles grow monodispersly. EDX (Figure 2.17) map also prove that the NCs contain Cd, Te, S, C, O, N. ICP-MS analysis (inserts of Figure 2.17) showed prolonged reflux time results in growing the particles so the number of Cd and Te amount increases with the time.

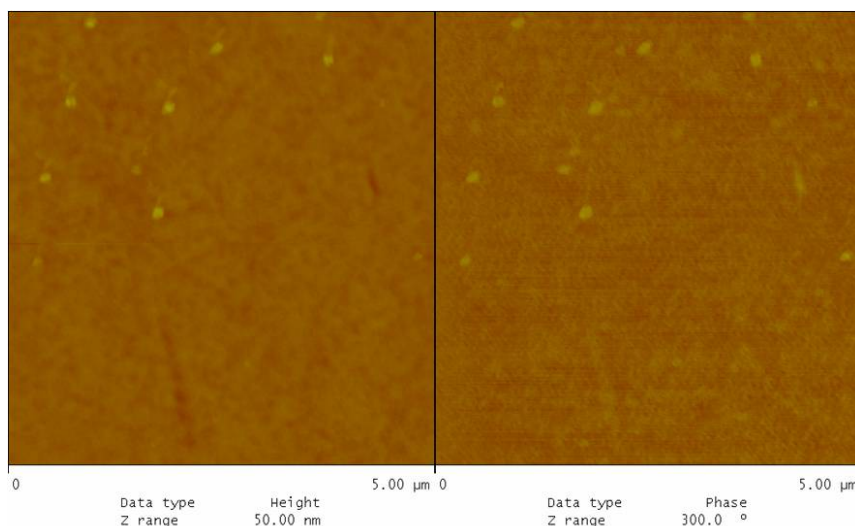


Figure 2.16. AFM picture of TGA-capped CdTe/CdS NCs (Te:S,1:10)

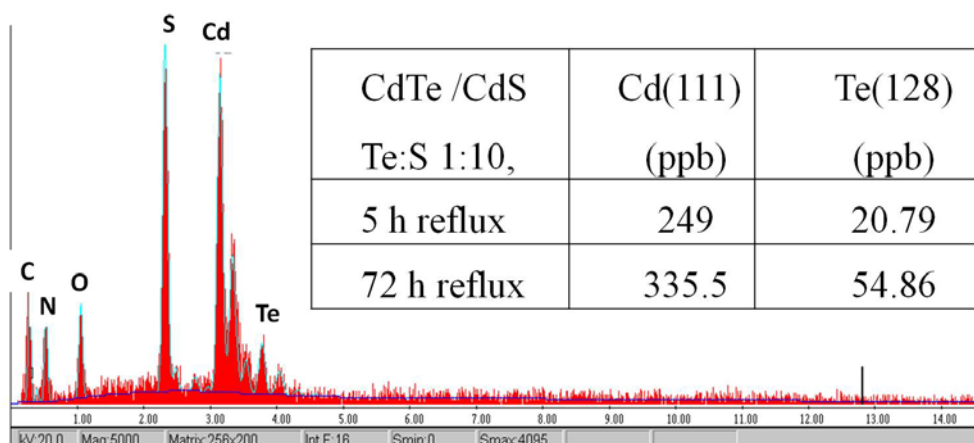


Figure 2.17. EDX map of TGA-capped CdTe/CdS NCs (Te: S; 1:10). Insert: the table shows ICP-MS results of TGA-capped CdTe/CdS NCs.

TEM images of the CdTe/CdS NCs (PL max: 575 nm) are represented in Figure 2.18. TEM measurements verified that crystalline sizes of CdTe/CdS NCs are less than 5 nm. Dynamic Light Scattering (DLS) measurements give the size of NCs as 5.4 ± 1.8 nm. These results are larger than TEM results as expected because DLS measures both the hard core and the hydrodynamic diameter of NCs. However, TEM measures only the hard core of NCs (Qian et al. 2007). TEM images show that NCs are spherical and the size distribution is monodispersed.

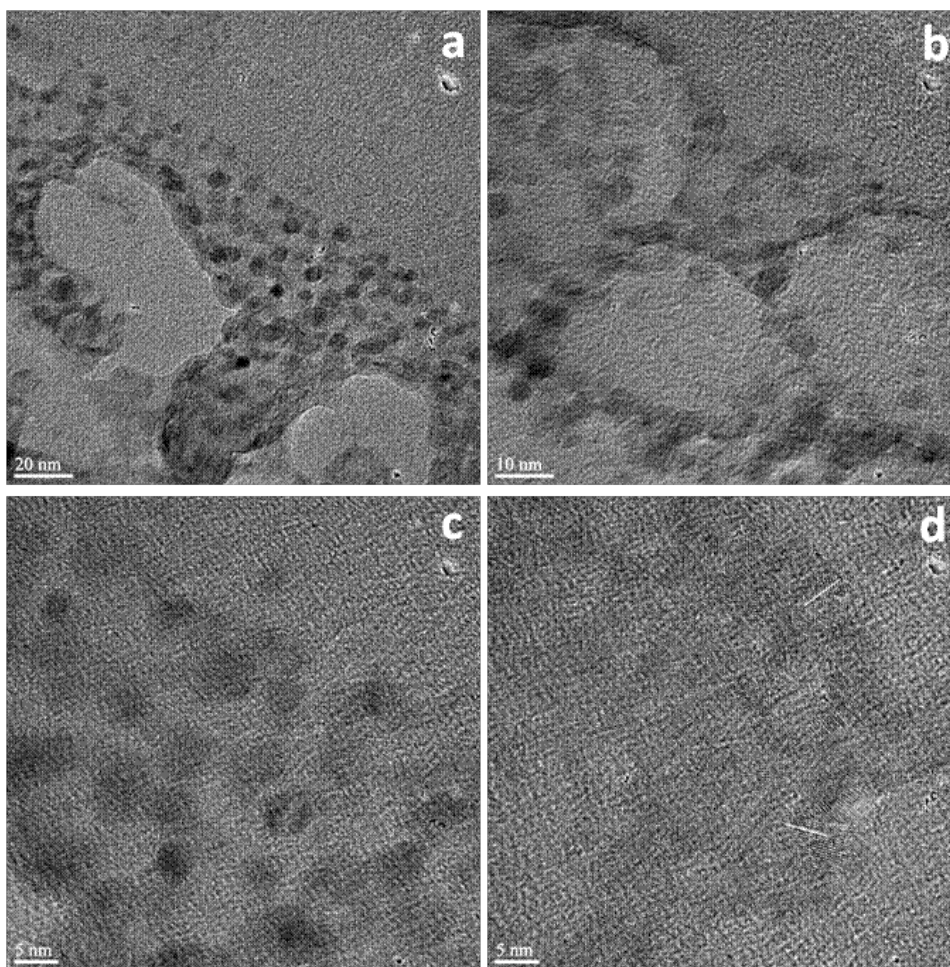


Figure 2.18. TEM images of CdTe/CdS core/shell NCs (a) 20 nm, (b) 10 nm, and (c-d) 5 nm scale.

Photoluminescence lifetime measurement is another method to confirm a change in the surface state of QDs and it is direct way to understand the role of surface defects in the change of photo induced luminescence of NCs. The characteristic PL decay profiles of exciton emissions of water-dispersible TGA-capped CdTe and CdTe/CdS are seen in Figure 2.19. For all samples, time-resolved emission measurements have been done at their peak wavelengths as in steady state PL spectra. The PL decay curves for each NC are successfully fitted to multi-exponential model. Fluorescence decay traces with relative amplitudes of the core and core/shell NCs are tabulated in Table 2.1.

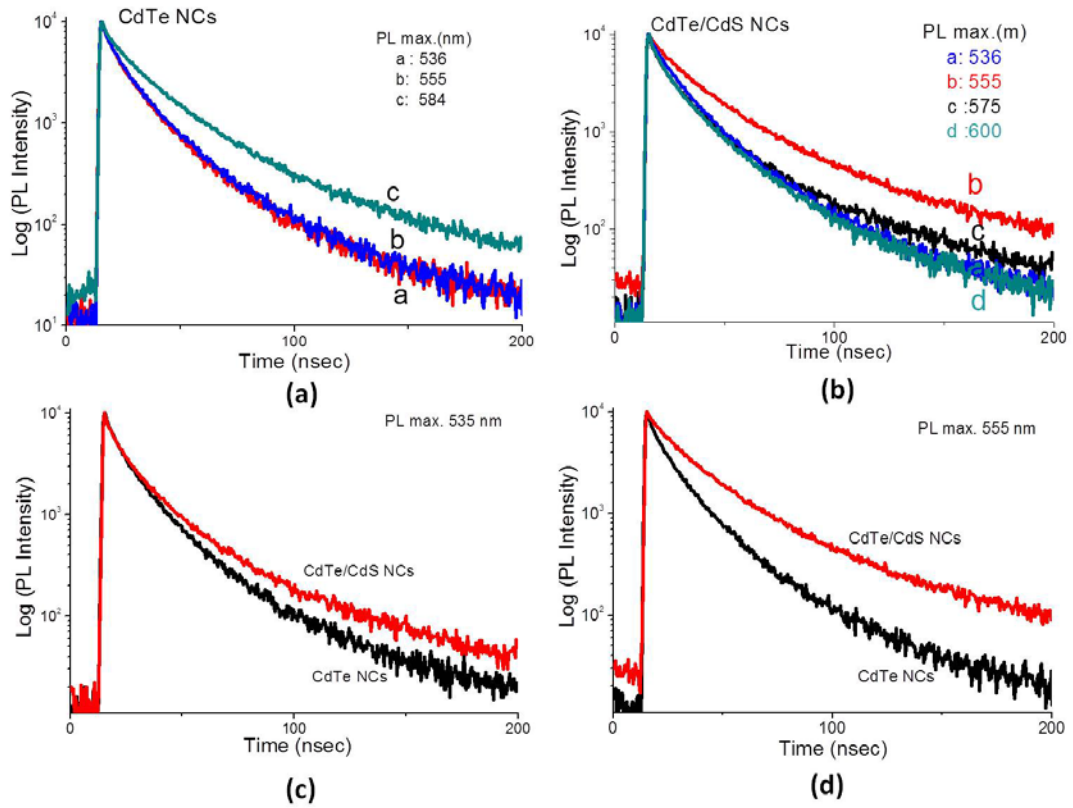


Figure 2.19. PL decay curves of exciton emission of (a) CdTe NCs of increasing size, (b) CdTe/CdS NCs of increasing size, (c) CdTe and CdTe/CdS NCs emitted at 535 nm wavelength, and (d) CdTe and CdTe/CdS NCs emitted at 555 nm wavelengths.

The decay times were best described by multi (three-four) exponential fit ($\chi^2 < 2.0$). Fitting was acceptable statistic χ^2 value as close to 1. The fitting yields shorter life time component, τ_1 , with of several nanoseconds and longer life time component, τ_3 (τ_4) equal to several tens of nanoseconds. Average lifetime τ was calculated using the equation below (eqn 2.1) (Jones et al. 2003) and they were tabulated with relative percentages of each components in Table 2.1.

$$\tau_{av} = ((A_1 * \tau_1^2) + (A_2 * \tau_2^2) + (A_3 * \tau_3^2)) / ((A_1 * \tau_1) + (A_2 * \tau_2) + (A_3 * \tau_3)) \quad (2.1)$$

Average lifetime values showed that coating of core with shell prolongs the PL lifetimes by more than hundred percent. CdTe and CdTe/CdS NCs emitted at 535 nm wavelength have different lifetime values (Figure 2.19c). While the average life value of the CdTe NCs is 25.2 ns, value of the CdTe/CdS is 62.7 ns. The amplitudes of longer lifetime values became higher in CdTe/CdS core shell NCs. Similar trend in lifetime values were observed for CdTe and CdTe/CdS NCs emitted at 555 nm wavelength. The

average life values of the CdTe and CdTe/CdS NCs are 28 ns and 79 ns, respectively. The core shell NCs has higher QY (26 %) than the CdTe NCs (17 %). Studies in the literature showed that the probability for the excitons to be present on the surface is higher in NCs with high QY. The increase in QY of CdTe/CdS compared to CdTe is due to CdS shell growth. The shell profoundly reduces PL quenching by defects from the surface of CdTe surface. Our results show that the exciton lifetimes in CdTe/CdS NCs are longer compared to the CdTe. CdS shell coating makes CdTe/CdS QDs a long lifetime compared to the CdTe cores due to drastic decrease in defective states in the core/shell structure. With increasing shell thickness; the average lifetime of the core/shell QDs was also prolonged. The spatial separation of electron and hole can result in a decrease of the wave function overlap and thus a longer lifetime of the charge recombination is expected in CdTe/CdS NCs. In the core/shell NCs CdTe and CdS have similar band gaps and the electron-hole is confined into the core and shell individually (Yuan et al. 2012, Gu et al. 2008, Rogach et al 2007).

Table 2.1. Fluorescence lifetime values for CdTe and CdTe/CdS NCs. χ^2 values are between 0.960 and 1.120. CdTe/CdS NCs have longer lifetime values.

Sample	PL emission (nm)	Size by DLS (nm)	τ_1 (ns)	Rel %	τ_2 (ns)	Rel %	τ_3 (ns)	Rel %	τ_4 (ns)	Rel %	τ_{average} (ns)
CdTe	535	2.2	3.4	11.4	12.8	61.5	36.1	27.0	-	-	25.2
CdTe	554	4.2	1.2	1.9	5.9	18.4	15.6	59.1	43.8	20.6	28.2
CdTe	585	5.1	5.6	9.2	20.7	64.6	2.1	26.2	-	-	26.4
CdTe/CdS	536	2.3	2.6	5.5	10.4	36.2	27.0	43.9	104.6	14.4	62.7
CdTe/CdS	557	4.1	2.2	1.3	13.7	30.1	33.4	52.2	129.7	16.5	79.4
CdTe/CdS	575	4.6	4.8	11.5	15.2	26.4	82.4	62.1	-	-	76.7
CdTe/CdS	600	5.3	4.4	14.4	16.4	64.5	46.5	21.2	-	-	30.1

The average lifetime values of CdTe/CdS NCs increases to some certain extent with coating and further increase in size leads to decrease in life time values. It shows that to increase in to some certain size reduces the surface to volume ratio and decreases number of possible defect states which act as recombination center. Further growth to larger sizes will cause the formation of interior trap states like crystal defect (Yagi et al. 2006, Liu et al. 2011). Upon the increasing in NC size the band gap energy of NCs decreases. While the energy of conduction band decreases the valance band energy shifts up and the energy of surface trap state decreases.

2.6. Conclusion

Thiol-capped CdTe core and CdTe/CdS core/shell NCs were preferred to study due to their efficient solubility in water without losing their photostability. They were synthesized successfully by using one-pot approach at relatively low temperature. The synthesis of the CdTe NCs was carried out under N₂ atmosphere in two steps. In order to get NCs of high quality, some optimization studies were performed. During the optimization the ratio of reactants, amount of solvent, pH, and reflux time were changed. It was found that the relative amount of TGA to Cd precursor plays a pivotal role in the quality of synthesis. The mole ratio of TGA to Cd was adjusted as 6.05:3.12 and it was the optimum ratio for synthesizing monodisperse spherical NCs with high QY. The pH of the solution was adjusted to 11.0-11.5 because at this pH the most possible Cd species have no/less adsorption site to the NCs. Therefore NCs grows monodispersly without agglomeration. The CdTe core NCs were synthesized in both 55 ml and 110 ml of water. In concentrated (55 ml) medium, the growth of NCs was very fast and the QY of the NCs was very low. The concentration affects the ion diffusion. The NCs synthesized in 110 ml distilled water have a QY of 25%. To obtain certain size NCs, reaction time was prolonged. The absorption and emission peaks of CdTe NCs continuously shifted to higher wavelengths with a prolonged reaction time. The shifts to longer wavelengths are due to quantum confinement. Optimized synthesis provides thiol capped CdTe NCs with bright emission tunable from 520 nm to 640 nm. The NCs show long decay up to 26.4 ns.

The CdTe core was coated with CdS shell. The coating CdTe by a CdS shell was done by the injection of thiourea to the crude solution of CdTe during the growth. Amount of thiourea was changed relative to the amount of Te. The coating enhanced the optical properties of the CdTe NCs. The highest quantum yield which is 45% was obtained when the mole ratio of Te:S was 1:10. The excitonic life time of CdTe/CdS core/shell NCs is higher than that of CdTe and the core shell NCs shows up to 79.4 ns PL decay. Thiol-capped NCs are water dispersible and quantized growth of NCs can be achievable by controlling the reaction time. All the NPs are reproducible with high quality.

CHAPTER 3

DEVELOPMENT OF COLLOIDAL $Zn_xCd_{1-x}Te$ TERNARY NANOALLOYS: TUNING SPECTRAL PROPERTIES OF THE NANOALLOYS BY SIZE AND COMPOSITION

3.1. Introduction

Colloidal synthesis of II-VI semiconductor nanocrystals (NCs) is well developed and nanoscale materials with desirable properties can be easily synthesized (Donega C.D.2011, Muray et al. 1994, Reiss et al. 2003, Steigerwald and Sprinkle 1987). The structure and composition of NCs along with size are the main factors that govern their optical properties. Band gap energy of NCs can be precisely engineered not only by size but also by changing constituent stoichiometries of NCs as well as their internal structure. Engineering of alloyed type NCs opens up production of new semiconductor NCs with different optical and electronic properties. The tuning of electronic and optical properties by changing the size may cause problems in many applications. Therefore, research on band gap engineering via control of NC composition is of particular interest but it is in infancy (Regulacio and Han 2010).

The alloying could tune the spectrum since the interatomic interaction among various elements or compounds are different. Generally, tuning the bandgap of NCs by alloying could result in high luminescence and stability compared to the case for the component with a narrower bandgap. Zhong *et al.* synthesized ternary $Zn_xCd_{1-x}Se$ and $Zn_xCd_{1-x}S$ alloyed NCs with luminescent properties comparable to or even better than the best-reported binary CdSe and CdS based NCs respectively (Zhong et al. 2003). The composition-tunable emission across the visible spectrum has been systematically demonstrated over the composition of the $Zn_xCd_{1-x}Se$ NCs and the emission wavelength shifts gradually to blue with the increase of Zn content.

The high luminescence efficiency and stability of the resulting alloy NCs are attributed to the larger particle size, higher crystallinity, higher covalency, lower inter-diffusion, and spatial composition fluctuation (Zhong et al. 2003).

Alloyed semiconductor NCs are different from core/shell type crystals and they can be classified into two groups as having (1) a uniform internal structure (i.e., homogeneous) or (2) a gradient internal structure, where the alloy composition varies in different parts of the NC (Figure 3.1). Depending on the number of components that constitute the alloy, they can be classified as either ternary (3 elements) or quaternary (4 elements). Ternary alloys can be called as either anion-common alloys such as $Zn_xCd_{1-x}A$ (A: S,Se,Te) in which only one anion present and cation-common alloys MS_xSe_{1-x} (M: Cd,Zn) in which only one cation present in crystal (Regulacio and Han 2010).

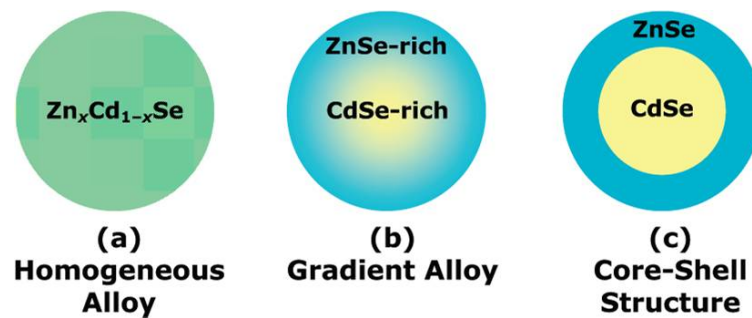


Figure 3.1. Schematic representation of having a (a) homogeneous, (b) gradient, and (c) core-shell structure of spherical NCs (Source: Regulacio and Han 2010).

Band gap tunability have been achieved in many homogeneous alloyed materials, such as $Cd_xHg_{1-x}Te$ (Qian et al. 2007), $Cd_xZn_{1-x}S(Se)$ (Zhong et al. 2003, Jin et al 2009, Kim, Park, and Jang 2010, Ouyang et al. 2008, Sharma et al. 2010) and $PbSe_xS_{1-x}$ (Brumer et al. 2005).

Generally the cation-common and anion-common composition variations have been done by controlling initial stoichiometry of reactants. Colloidal ternary anion-common alloys such as $Zn_xCd_{1-x}S$ and $Zn_xCd_{1-x}Se$ have been synthesized by different research groups (Sharma et al. 2010, Kim, Park, and Jang 2010, Zhong et al. 2003, Lesnyak et al. 2008).

It is possible to tailor alloy properties within the range of values corresponding to the pure parents. Among a variety of binary metal chalcogenides, the $Zn_xCd_{1-x}Te$ ternary alloy system has not been extensively studied. $Zn_xCd_{1-x}Te$ alloyed type core NCs still need to be developed.

There are a few studies about the synthesis of colloidal $Zn_xCd_{1-x}Te$ NCs (hereafter nanoalloys) via wet chemistry and knowledge about the synthesis is limited.

Li *et al.* studied the composition of crystals changed by adjusting the reaction time. They have synthesized water-dispersible $Zn_xCd_{1-x}Te$ alloyed NCs with glutathione (GSH) as the stabilizer by incorporating Zn into CdTe through a one-step aqueous route. Emission wavelength of $Zn_xCd_{1-x}Te$ NCs was tuned from 470 to 610 nm depending on the size and composition. The photo-luminescent quantum yield of resultant NCs reached up to 75% (Li *et al.* 2010).

In another study, Gholami-Kaliji and his coworkers studied the influence of synthesis temperature on the optical properties of the TGA-capped $Zn_{0.4}Cd_{0.6}Te$ alloyed NCs. They reported that the size of the NCs can be adjusted by applying different reaction temperatures ranging from 80 to 125 °C (Gholami-Kaliji *et al.* 2011).

Wang *et al.* synthesized TGA-capped $Zn_xCd_{1-x}Te$ nanoalloys having maximum quantum yield (QY) of 20.2% in aqueous medium. Composition-dependent optical behavior was observed for $Zn_xCd_{1-x}Te$ nanoalloys where x was changed from 0 to 0.7. Their study on the effect of growth time and the synthesis temperature on the optical properties of the nanoalloys showed that PL maxima shifted to longer wavelength due to quantum size effect. (Wang *et al.* 2007).

The synthesis of trioctylphosphine oxide stabilized and highly luminescent $Zn_xCd_{1-x}Te$ ternary nanoalloys were achieved at 300°C by Abu Bakar *et al.* During their synthesis the molarity of cadmium and zinc were controlled at 1 mmol and their respective mole ratio was changed. The NCs have a QY of ca. 60% and PL wavelength was in the range of 640 to 675 nm. They did not observe any relationship between composition and photophysical properties of the nanocrystals with the incorporation of Zn into CdTe nanostructure (Abu Bakar *et al.* 2009).

The central objective of the present work is to use the chemical routes to synthesize colloidal $Zn_xCd_{1-x}Te$ ternary nanoalloys. The optical and structural properties of $Zn_xCd_{1-x}Te$ nanoalloys have been studied in detail by adjusting the metal mole ratio in the precursor mixture. The findings indicate that the absorption edges of those nanoalloys can be varied from blue to red region, while the emission peak can be adjusted from 500 to 650 nm. Moreover, by the compositional variation of $Zn_xCd_{1-x}Te$ ternary nanoalloys, it is possible to alter the lattice constant since these parameters are dependent on the Cd/Zn ratio. Colloidal $Zn_xCd_{1-x}Te$ nanoalloys will be of particular

interest due to tunability of compositions, low temperature synthesis, simple set-up, low cost, and water-dispersibility.

3.2. Experimental

All of the chemicals with the highest purity were used without further purification. During the synthesis, the salts of Zn and Cd metals, NaHTe, thioglycolic acid, water, Te powder, NaBH₄ and sodium hydroxide were used. Cadmium chloride (CdCl₂, Fluka 99%) and zinc chloride (ZnCl₂, Sigma Aldrich 95%) were Cd²⁺ and Zn²⁺ precursors, respectively. Sodium borohydride (NaBH₄, Riedel 95%), Tellurium powder (Te, Fluka 99.9%) and distilled water were used to synthesize Te precursor, NaHTe. Thioglycolic acid; TGA (HSCH₂CO₂H, Merck 98%) was used as capping agent. NaOH was used to adjust the pH of the precursor solution alkaline. 2- Propanol (C₃H₈O, Riedel 99.5%) was used to precipitate the nanoalloys for purification.

3.2.1. Synthesis

The one-pot method was used to synthesize the nanoalloys. The same optimization conditions were applied as developed for the synthesis of CdTe NCs. During anion-common ternary nanoalloys synthesis such as Zn_xCd_{1-x}A (where A is Te, Se, S), the general trend is to keep the initial metal mole ratio constant (Sadhu and Patra 2008, Ouyang et al. 2008, Zhong, Feng, et al. 2003, Zhong, Han, et al. 2003). In this study, the amounts of cadmium and zinc precursor were kept constant at 3.12 mmol. Table 3-1 shows how individual mole numbers of CdCl₂, ZnCl₂ and NaHTe precursor were varied in the reactions.

3.2.1.1. Synthesis of NaHTe as Te Precursor

In all experiments, freshly synthesized purple-colored NaHTe was used (Gu et al. 2008). Te powder (0.0918 g) and NaBH₄ (0.06 g) were put into a reaction flask and it was purged with N₂ for 30 min. After addition 10.0 ml of distilled water to the reaction flask, the mixture was heated at 80⁰C for 2 h under N₂ atmosphere. The solution was

allowed to form purple color under the N₂ flow. No purification techniques were performed.

Table 3.1. The mole numbers of CdCl₂, ZnCl₂ and NaHTe

CdCl ₂ (mmol)	ZnCl ₂ (mmol)	NaHTe (mmol)	Initial Zn/Zn+Cd mole ratio
3.00	0.12	0.18	0.04
2.87	0.25	0.18	0.08
2.65	0.47	0.18	0.15
2.55	0.57	0.18	0.18
2.50	0.62	0.18	0.20
2.45	0.68	0.18	0.22
2.39	0.73	0.18	0.23
2.34	0.78	0.18	0.25
2.28	0.84	0.18	0.27
2.20	0.92	0.18	0.29
2.14	0.98	0.18	0.31
2.08	1.08	0.18	0.34
1.95	1.17	0.18	0.38
1.82	1.30	0.18	0.42
1.69	1.43	0.18	0.46
1.56	1.56	0.18	0.50
1.32	1.80	0.18	0.58
1.08	2.08	0.18	0.66
0.78	2.34	0.18	0.75
0.52	2.60	0.18	0.83
0.25	2.87	0.18	0.92
0.00	3.12	0.18	1.00

3.2.1.2. Synthesis of Zn_xCd_{1-x}Te Ternary Nanoalloys

The Zn_xCd_{1-x}Te alloyed NCs were synthesized by addition of freshly prepared oxygen-free NaHTe solution to the deaerated hot (80 °C) zinc-cadmium mixed precursor solutions. Experimentally, the precursor solutions (Cd+Zn) were prepared by mixing CdCl₂, ZnCl₂ and 420 μl thioglycolic acid in 110 ml distilled water. The molar ratio of Zn to Cd in the mixed precursor solutions was adjusted. Then TGA as a capping agent was added to the mixed precursor solutions. To preserve the uniform size

distribution and to prevent agglomeration of the semiconductor nanoalloys, capping agents are generally exploited during the synthesis. Then the pH of the solution was adjusted to 11-11.2 by addition of 1.0 M NaOH solution. At that pH, colorless precursor solutions were obtained. The solution was transferred into a two-necked flask and bubbled with N₂ to get rid of oxygen in the medium. Then the precursor solutions were heated at 80 °C for 1 h. Further reflux were avoided to prevent the possible decomposition of thioglycolic acid to give S²⁻ (Rogach et al. 2007).

The reaction temperature was increased up to 110 °C and the resulting mixture solution was refluxed at this temperature to get nanoalloys with desired size and composition. Schematic illustration of ternary Zn_xCd_{1-x}Te nanoalloy synthesis is shown in Figure 3.2. The color of the solution changed gradually from colorless to brown (reddish), showing the aging of the nanoalloys. The growth of Zn_xCd_{1-x}Te nanoalloys was continuously monitored by taking aliquots amount of colloidal Zn_xCd_{1-x}Te solution and quenching the reaction at different time interval. Finally, Zn_xCd_{1-x}Te nanoalloys were precipitated by addition of isopropyl alcohol and then centrifuged. The Zn_xCd_{1-x}Te nanoalloys as powder were obtained by drying under N₂ atmosphere.

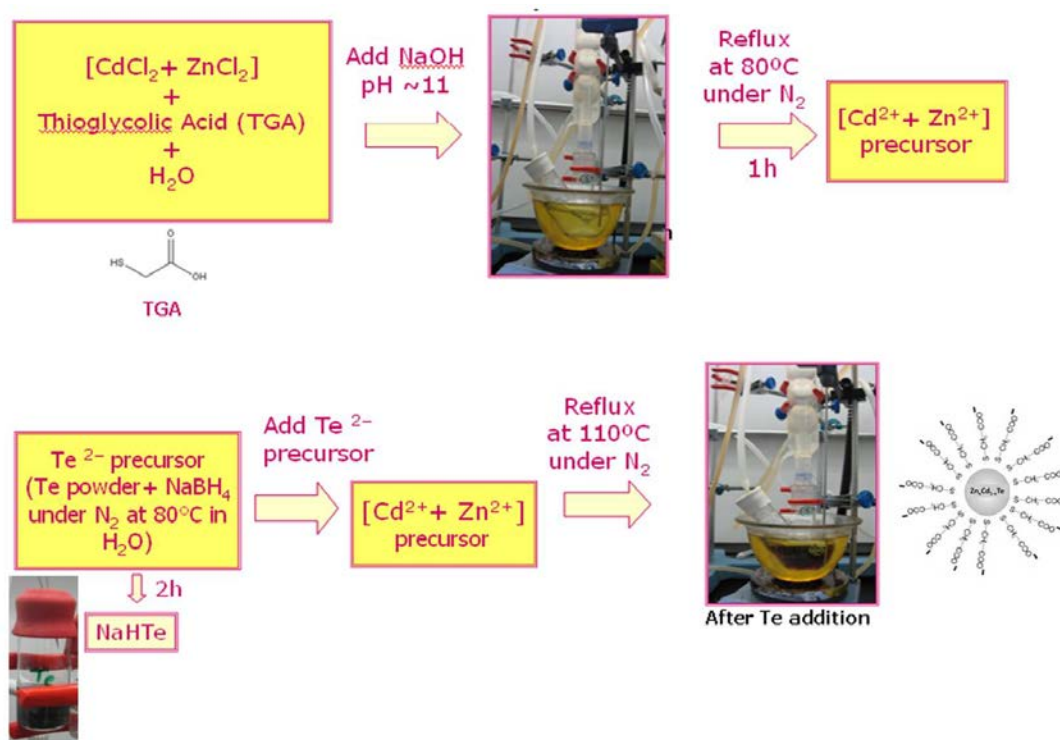


Figure 3.2. Schematic illustration of synthesis of Zn_xCd_{1-x}Te ternary nanoalloys

3.3. Results and Discussion

It is well established that the adjustment of the initial mole ratio of precursors modifies the composition of the nanoalloys (Lee et al 2006, Jang et al 2003, Jin et al 2009, Lesnyak et al 2009, Kim et al 2010, Khatei et al 2011). Therefore, it is expected that the optical properties should be tuned by the composition. The initial mole ratio of metal precursors was systematically varied by keeping the size of the nanoalloy constant. The adjustment of mole ratio was realized by increasing the amount of Zn/Cd from 0.04 to 1.00 while keeping the total amount of metals constant, Cd+Zn: 3.12 mmol, in metal precursor mixture (Table 3.1, Table 3.1).

For homogeneous anion-common ($Zn_xCd_{1-x}A$ where A: S,Se,Te) alloy crystals there should be systematic blue shifting of the absorption and the emission maxima as the fraction of Zn incorporated in the crystal structure increases because band gap of ZnTe (2.25 eV) is wider than that of CdTe (1.49 eV) (Madelung 1996, Streetman and Sanjay 2000).



Figure 3.3. Images of $Zn_xCd_{1-x}Te$ nanoalloys with different Cd:Zn ratio under day (above) and under UV light (below).

In the Figure 3.3, the photograph of $Zn_xCd_{1-x}Te$ nanoalloys under day light and illuminated under UV light are seen. The luminescent color varied from green to orange depending on the composition of the nanoalloys.

The determination of internal structure is challenging but it is necessary not straightforward. The Vegard's law (Eqn 1.10) has been used to determine the composition of the nanoalloys. However, the fractions of Zn and Cd in chemical

formulas calculated from XRD pattern and EDX analysis were not similar to the results obtained from ICP-AES analysis (Table 3.2). For relatively homogeneous nanoalloys the findings are similar. However, for some nanoalloys the results obtained from the XRD and EDX analysis techniques were not reproducible. Therefore it is required to understand whether the ternary nanoalloy possesses unhomogeneous internal structure or not. ICP-AES findings to measure the nanoalloy composition are found to be reproducible.

Table 3.2. Chemical formula of the nanoalloys obtained by different analysis techniques.

Initial Zn/Zn+Cd mole ratio	Nanoalloy Composition		
	ICP-AES	EDX	XRD
0.04	Zn _{0.16} Cd _{0.84} Te	Zn _{0.31} Cd _{0.69} Te	Zn _{0.24} Cd _{0.76} Te
0.08	Zn _{0.19} Cd _{0.81} Te	Zn _{0.33} Cd _{0.67} Te	Zn _{0.27} Cd _{0.73} Te
0.15	Zn _{0.14} Cd _{0.86} Te	Zn _{0.18} Cd _{0.82} Te	Zn _{0.21} Cd _{0.79} Te
0.18	Zn _{0.12} Cd _{0.88} Te	Zn _{0.54} Cd _{0.46} Te	Zn _{0.24} Cd _{0.86} Te
0.2	Zn _{0.17} Cd _{0.83} Te	Zn _{0.19} Cd _{0.81} Te	Zn _{0.30} Cd _{0.70} Te
0.23	Zn _{0.19} Cd _{0.81} Te	Zn _{0.15} Cd _{0.85} Te	Zn _{0.29} Cd _{0.71} Te
0.25	Zn _{0.21} Cd _{0.88} Te	Zn _{0.28} Cd _{0.72} Te	Zn _{0.20} Cd _{0.80} Te
0.27	Zn _{0.23} Cd _{0.77} Te	Zn _{0.11} Cd _{0.89} Te	Zn _{0.39} Cd _{0.61} Te
0.29	Zn _{0.27} Cd _{0.73} Te	Zn _{0.17} Cd _{0.83} Te	Zn _{0.23} Cd _{0.77} Te
0.31	Zn _{0.27} Cd _{0.73} Te	Zn _{0.13} Cd _{0.87} Te	Zn _{0.36} Cd _{0.64} Te
0.34	Zn _{0.35} Cd _{0.65} Te	Zn _{0.25} Cd _{0.75} Te	Zn _{0.54} Cd _{0.46} Te
0.38	Zn _{0.31} Cd _{0.69} Te	Zn _{0.23} Cd _{0.77} Te	Zn _{0.42} Cd _{0.58} Te
0.42	Zn _{0.41} Cd _{0.59} Te	Zn _{0.14} Cd _{0.86} Te	Zn _{0.65} Cd _{0.045} Te
0.46	Zn _{0.37} Cd _{0.63} Te	Zn _{0.17} Cd _{0.83} Te	Zn _{0.52} Cd _{0.38} Te
0.50	Zn _{0.13} Cd _{0.87} Te	Zn _{0.35} Cd _{0.75} Te	Zn _{0.18} Cd _{0.82} Te
0.58	Zn _{0.46} Cd _{0.54} Te	Zn _{0.24} Cd _{0.76} Te	Zn _{0.75} Cd _{0.25} Te
0.66	Zn _{0.18} Cd _{0.82} Te	Zn _{0.19} Cd _{0.81} Te	Zn _{0.27} Cd _{0.73} Te
0.75	Zn _{0.35} Cd _{0.65} Te	Zn _{0.28} Cd _{0.78} Te	Zn _{0.21} Cd _{0.79} Te
0.83	Zn _{0.65} Cd _{0.35} Te	Zn _{0.52} Cd _{0.46} Te	Zn _{0.44} Cd _{0.56} Te
0.92	Zn _{0.56} Cd _{0.44} Te	Zn _{0.69} Cd _{0.31} Te	Zn _{0.85} Cd _{0.15} Te

The metal variations inside nanoalloys during growth have been followed by ICP-AES. To determine how composition of the nanoalloys varies with reaction time, samples were taken during the growth at different time intervals. The same volume of samples have been purified through precipitation by 2-propanol. Both upper (supernatant) and lower parts of the aliquots have been separated and diluted with the proper amount of water. Then, the nanoalloys have been decomposed by 2.5% HNO₃ acid. A set of standard solutions was prepared for each metal ion. The calibration

curves, intensity (counts) versus concentrations of Cd^{2+} and Zn^{2+} were plotted separately. The R-squared values were found to be between 0.998 and 0.994 for Cd and Zn standards, respectively. By using the curves, the amounts of metals in supernatants and in nanoalloys were calculated. The mass-balance analysis of the crude solution of the nanoalloys provided that the ICP-AES findings are reproducible. The analysis shows that total amount of Cd and Zn is approximately equal to their respective initial amounts with maximum error of 15.7%. These results are tabulated in Table 3.3.

Table 3.3. Total amount of Cd and Zn in the supernatant and the aged nanoalloys measured by ICP-AES with errors.

Zn/Zn+Cd mole ratio in precursors	Cd amount in precursors (mg)	Total amount of Cd in supernatant+crystals obtained by ICP-AES (mg)	Zn amount in precursors (mg)	Total amount of Zn in supernatant+crystals obtained by ICP-AES (mg)	% error Cd amount	% error Zn amount
0,08	321.44	309.25	16.5	14.9	3.8	9.7
0.18	285.60	250.53	37.62	31.81	12.3	15.4
0.25	262.08	229.17	51.48	49.95	12.6	3.0
0.34	232.96	204.02	71.28	62.92	12.4	11.7
0.50	174.72	168.42	102.96	93.50	3.6	9.2
0.58	147.84	129.81	118.00	100.72	12.2	14.6
0.66	120.96	104.43	137.28	122.54	13.7	10.7
0.83	58.24	51.37	171.60	164.50	11.8	4.1
0.92	28.00	24.37	189.42	177.15	13.0	6.5

Figure 3.4 depicts the variation of Zn and Cd inside the crystal structure during growth. Metal variations in the nanoalloys during growth depend on both metal amounts in precursor mixture and reflux time. It is seen that nanoalloys synthesized under low Zn/Zn+Cd mole ratio in precursor (from 0.04 to 0.50), the ratio of Zn/Cd in the nanoalloys is almost constant during the growth (Figure 3.4a-h). Increasing in Zn/Zn+Cd mole ratio in precursor results in fluctuations. As the reflux time prolongs metal fractions in the nanoalloys are changing through the growth (Figure 3.4i, k). Under very high Zn/Zn+Cd mole ratio in precursor (from 0.83 to 0.92), the ratio of Zn/Cd in the nanoalloys is almost constant during the growth (Figure 3.4l, m). According to number of unreacted metal ions, reactivity of the metals (Cd^{2+} and Zn^{2+}) towards Te^{2-} anion differed from each other. The competitive behavior in terms of activity of the metals was seen especially when the Zn/Zn+Cd was 0.5. Up to that particular ratio, the structures of the nanoalloys are rich in Cd. At higher Zn/Zn+Cd mole ratio in precursors, generally the nanoalloys had Zn-rich structure. The nanoalloys

have four different internal structures (distribution of atoms in the nanoalloys) in overall depending on the amount of metals, the reactivity of metal ions to Te^{2-} ions, and the growth time. Figure 3.5(a-d) simply memorizes the groups and Figure 3.5 (e) represents internal structure of formed nanoalloys schematically.

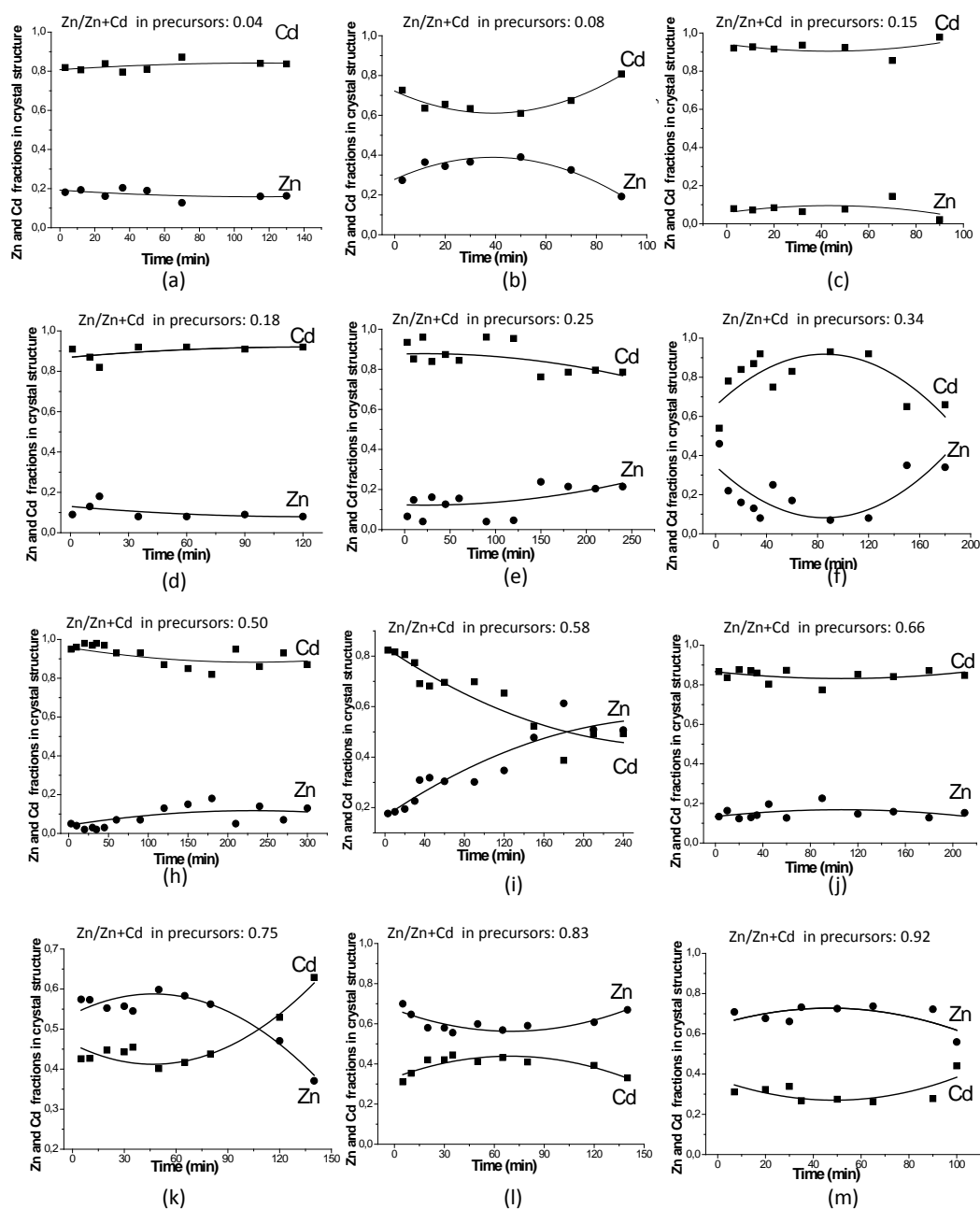


Figure 3.4. Change in the respective mole ratios of Zn and Cd in colloidal nanoalloys synthesized under different metal precursor concentration with various growth times to keep the time to keep the size constant. Zn/Zn+Cd were changed from 0.04 to 0.92.

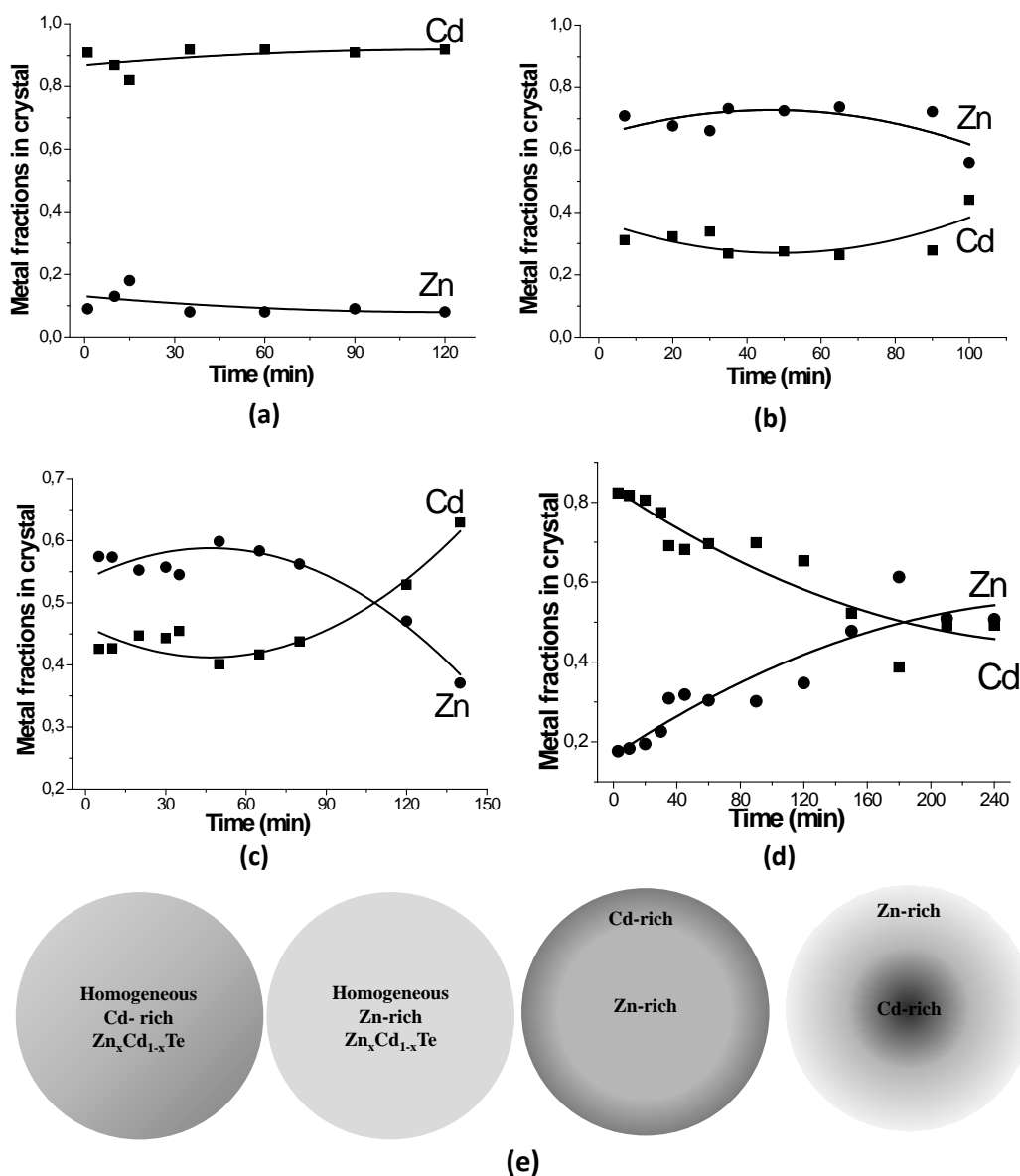


Figure 3.5. (a-d) Change in the respective mole ratios of Zn and Cd in colloidal nanoalloys synthesized under different mole ratio of metal precursors through reflux time. The change is followed by ICP-AES. (e) Schematic representation of homogeneous and heterogeneous nanoalloy structures.

It is observed that at high Cd and low Zn precursor concentration where $Zn/Zn+Cd$ are between 0.04 and 0.50, the nanoalloys have Zn-poor Cd-rich internal structure. The ratio of Zn/Cd in the internal structure of the nanoalloy is almost constant with time and at the end of the growth, the composition is still rich in Cd and poor in Zn. According to Figure 3.5 (a) the respective fractions of the metals are roughly constant during reaction. Cd^{2+} ions are more reactive than Zn^{2+} ions toward Te^{2-} ions. CdTe is the easiest crystal system which could be formed compared to ZnTe under the high amount of cadmium precursor. Since both cadmium and tellurium possess higher

chemical potential and high affinity energy for inter-coordination than the ZnTe system (Trindade, O'Brien, and Pickett 2001). With a little increase in the initial Zn/Zn+Cd mole ratio in the precursor ($0.50 < \text{Zn}/\text{Zn}+\text{Cd} < 0.58$), at the beginning of the growth the formed crystals is rich of Cd. With the increasing growth time, more Zn is incorporated into the nanoalloy structure. As the crystal size is getting larger, the outer part starts to be rich in Zn. The nanoalloy has Cd-rich Zn-poor inner and Zn-rich Cd-poor outer internal structure with low quantum yield (Figure 3.5(d)). The increase in the initial Zn/Zn+Cd mole ratio from 0.66 to 0.75 results in the formation of initially Zn-rich Cd-poor internal crystal structure. As the growth time prolongs, Zn fractions in the nanoalloys decrease. The nanoalloys have Zn-rich Cd-poor inner part and Cd-rich Zn-poor outer part. The change in the metal fractions in the nanoalloy crystal structure is shown in Figure 3.5(c). On the other hand drastic increase in initial Zn mole in the precursor mixture ($\text{Zn}/\text{Zn}+\text{Cd}=0.92$) causes the formation of Zn-rich and Cd-poor gradient internal structure ((Figure 3.5 (b)). The metal ratio in the precursor mixture and reactivity of the metal ions totally affect their activity towards Te^{2-} anion. Generally with the precursors having high amount of Zn, Zn^{2+} ions form complex with TGA and the formed nanoalloys have not been passivated by enough capping agent. The lattice mismatch between CdTe and ZnTe crystals is $\sim 5-6\%$ (Rawalekar et al. 2010). The mismatch creates considerable distortion in the sense that atomic positions in the original zinc blend lattice structure. As the lattice parameter decreases, the formation of the vacancy is more favorable. Moreover, Zn-Te bonds are less ionic and thus it is easier to break Zn-Te bond compared to Cd-Te bonds. It favours the formation of cation-site defects. Some studies in literature showed that even the nanoalloys have equal number of Zn, depending on the arrangement of the metals throughout the inner crystal structure there will not be a systematic change in photophysical properties such as position of PL peak and quantum yield with the Zn incorporated into the CdTe crystal structure due to exciton leakage (Jin et al. 2009, Lesnyak et al. 2008).

In this study, a possible alloying mechanism for the growth of the $\text{Zn}_x\text{Cd}_{1-x}\text{Te}$ nanoalloys is proposed. At low Zn and high Cd precursor concentration a Cd-rich and Zn-poor core is formed because Cd is more reactive than Zn toward Te. As the initial Zn/Zn+Cd increases up to 0.58, the internal structure of the nanoalloy is rich of Cd. When the growth time prolongs, there should be a gradual increase in Zn incorporation into the crystal structure. The outer part has an increase in the zinc content toward the surface rather than core. So the outermost part may mainly consist of $\text{Zn}_x\text{Cd}_{1-x}\text{Te}$. Such

an accumulation of ZnTe in the outer part directly leads to an effective inorganic 'coating' to protect the Cd-rich core; the result is nanoalloys with high quantum efficiency. Because the outer layer acts as a protective shell like in core/shell structures. Nanoalloys synthesized by low Zn/Zn+Cd initial mole ratio, have the highest QYs.

At high zinc concentration in the precursor metal mixture ($Zn/Zn+Cd=0.66$), the zinc might have the preference to make complex with the excess of TGA in the solution, that might lead to the formation of the nanoalloys with Zn content. Further increase in Zn concentrations in the precursor mixture results in nanoalloy having higher amount of zinc. Also, at this condition, the excess zinc in the reaction might induce changes in the surface physics and chemistry of the resulting nanoalloys so that enable the formation of high surface defect on the NCs. Hence, this could enhance the surface recombination trap and decreases the QY of which the lowest was obtained for the nanoalloys ($Zn_{0.65}Cd_{0.35}Te$) having high Zn fractions.

In terms of nucleation and growth there is no study on the colloidal synthesis of ternary $Zn_xCd_{1-x}Te$ nanoalloys. To understand the reaction completely, we should be interested in the reaction kinetically. We tried to understand the kinetic of the ternarification processes. The chemistry of the reaction is complex. It was easy to nucleate and to grow the CdTe without any impurities or any other metals. But, in our experimental conditions, it is very hard to synthesize nano-sized ZnTe. In the presence of Cd cation, $Zn_xCd_{1-x}Te$ nanoalloys have been synthesized. The presence of any host material (Cd^{2+}) or any impurities create a new reaction pathway. Many reaction conditions were used to control the synthesis of ternary $Zn_xCd_{1-x}Te$ nanoalloys. However the nucleation was very hard to control. In every stoichiometry of reactants the composition of critical nuclei is different and difficult to determine. Cd^{2+} (109 pm) and Zn^{2+} (88pm) have different ionic radii. The sizes of the metal ions and their reactivities have impact on the size of nuclei (crystallite). According to our results nucleation is very sensitive to respective mole ratio of the metal precursors. At low Zn concentration, the formed nuclei is in rich of Cd and since the size of $Zn^{2+} < Cd^{2+}$, Zn ion can incorporate into CdTe nuclei without much distortion. The compatibility of ions is low at low Zn ion concentration. At high initial Zn concentration, nuclei are Zn-based and Cd distorts the nuclei to some extent and lattice energy of the crystallite. So nucleation is extremely difficult at high Zn concentration.

When only Zn (3.12 mmol) was used as a metal source, the synthesis of ZnTe nanocrystal was not achieved. The crystal structures of ZnTe crystals can be assigned as

cubic structures, with the presence of characteristic (111), (220), and (311) peaks in the XRD patterns (ICDD PDF No. 00-001-0582) but the crystals did not contain any ZnTe (Figure 3.6 upper insert). XRD diffraction pattern of the formed products is seen in Figure 3.6 and it shows that at that experimental condition only Te and NaCl were formed as products. XRD patterns of the products can be assigned to Te crystals with the characteristic (101), (102), and (110) Te peaks (ICDD PDF No. 00-036-1452) (Figure 3.6 lower insert). The spectrum also has some sharp peaks belonging NaCl crystals (ICDD PDF No. 78-0751).

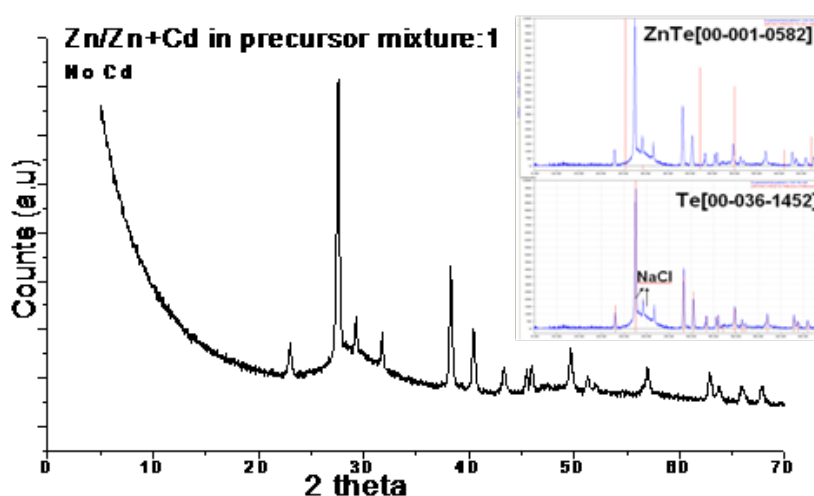


Figure 3.6. X-ray powder diffraction pattern of the crystals formed when Zn/Zn+Cd mole ratio in precursor solution is 1. Insert: (upper) the mismatched lines represents the characteristic XRD peaks of ZnTe, (lower) matched lines belongs to the characteristic XRD peaks of Te crystals.

ICP-AES was used to investigate the metal variation in all of the nanoalloys. Figure 3.7 shows the results obtained from all nanoalloys synthesized under different precursor concentration where the relative amount of Zn in precursors varied from 0 to 1. The percent Zn in the synthesized nanoalloys can be almost linearly controlled by the initial mole ratio of Zn/Zn+Cd, up to 50% as depicted in Figure 3.7. The graph deviates from linearity at high Zn/Zn+Cd mole ratio in the precursor mixture. With an increase in the initial Zn/Zn+Cd ratio from 0.46 to 0.92, the composition of the alloy shows fluctuation. The increase in the initial Zn/Zn+Cd mole ratio results in formation of nanocrystals having with highest amount of Zn (about 0.65). But overall trend is that the amount of Zn inside the nanoalloys tends to increase as the initial Zn/Zn+Cd mole ratio increases. At the near-integer values of the Zn: Cd mole ratio in precursor solution

(approximately 1:1, 2:1, 3:1, 5:1), the Zn amount in the nanoalloy changes in parabolic pattern with respect to initial amount of the metal precursor (The insert in Figure 3.7).

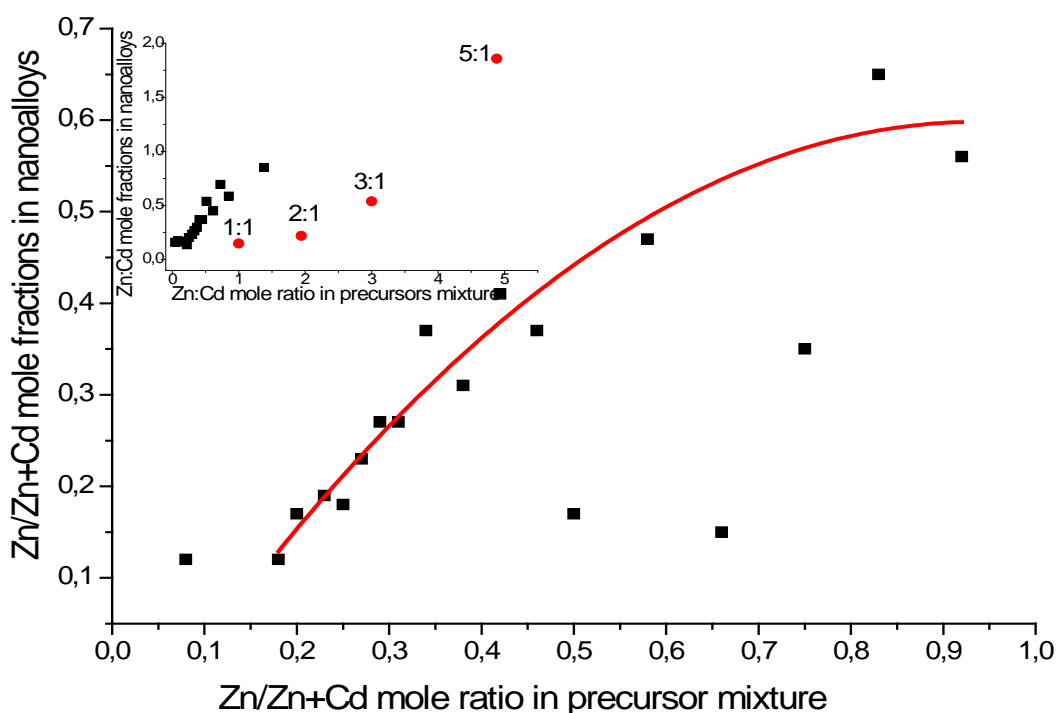


Figure 3.7. Change in Zn/Zn+Cd mole fractions in nanoalloy structure with Zn/Zn+Cd mole ratio in precursor solutions. ICP-AES is used to measure the relative amount of Zn in nanoalloys. Insert: Change in Zn:Cd mole ratio in the nanoalloy with the initial Zn:Cd ratio.

Respective mole ratio of the metals and their reactivity are two competing parameters that may play a key role to control colloidal synthesis of the nanoalloys and the quality of the nanocrystals. The formation of Cd-rich nanoalloys validates the method for the nanoalloy formation even in the presence of excess Zn ions. When the mole of Zn in the precursors is equal to that of Cd (Zn/Cd mole ratio: 1:1), Cd-rich $Zn_{0.13}Cd_{0.88}Te$ nanoalloys were formed. Final composition of the nanoalloys shows that Cd is 6 times reactive than Zn. Under that condition the Cd-rich nanoalloy is formed almost homogeneously. It is noted under the excess amount of cadmium, the nanoalloys was ended with cadmium ions facilitating bonding with the ligands, thus protecting the emitting part of the nanoalloys, resulting in highly fluorescent nanoalloys compared to Zn-ended nanoalloys. The reactivity of Cd towards Te is lowered significantly with the increase in Zn mole ratio in the precursor solution. The reactivity of metals towards Te become similar when the metal mole ratio approaches to 4:1 (Zn: Cd). As the Zn: Cd ratio in precursor mixture is higher than 4:1, Zn-rich nanoalloys is formed. When the

precursor Zn:Cd mole ratio is 5:1, Zn behaves more active than Cd towards the Te anion and Zn-rich ($Zn_{0.65}Cd_{0.55}Te$) nanoalloys are formed. Further increase to Zn:Cd to 11.5 resulted in Zn-rich alloy with low QY. High amount of zinc in the precursor mixture surpass the reactivity of Cd ions, a Zn-rich internal structure is formed.

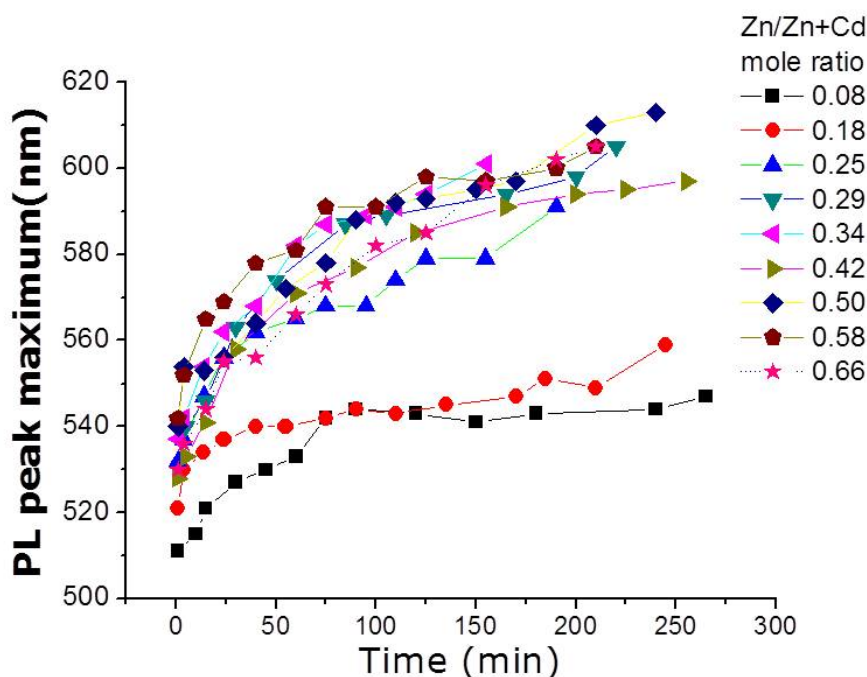


Figure 3.8. The temporal evolution of peak position of PL emission peaks of TGA-capped $Zn_xCd_{1-x}Te$ nanoalloys. The initial Zn/Zn+Cd mole ratio in precursor mixture was varied.

The growths of the nanoalloys were followed by means of the steady state spectroscopy. The temporal evolution of the PL peak maxima is shown in Figure 3.8. The PL peaks shift to red by the growth time. The growth trends of the nanoalloys regardless of composition are similar. Growth curves rise very fast and the growth rates of the seeds are different at the beginning. After certain duration, the growth rate decreases. Various parameters affect both the nucleation and the growth. However, the important parameter is the respective mole ratio of metal precursors. Although Cd is more reactive than Zn towards Te (Trindade, O'Brien, and Pickett 2001) the respective concentration of metals could modify the rate of reactivity towards the anion. The change in PL maxima is due to both change in size and composition of nanoalloys. The PL peak maxima of the nanoalloys, sampled at the moment when reflux temperature reached at 110 °C (within 25 min), were different. It indicates that at nucleation step, varies kind of seeds were formed. The crystals synthesized with lower amounts of

Zn/Zn+Cd yielded more blue-shifted. PL peaks at the initial stage of the growth. The growth rate can be precisely controlled by the reaction time, but the rate of nucleation was very fast, therefore it is hard to control. Rate of nucleation is independent of composition at all initial metal precursors. The two different trends attributed to the competitive reactivity of the metals towards the anion during the growth process.

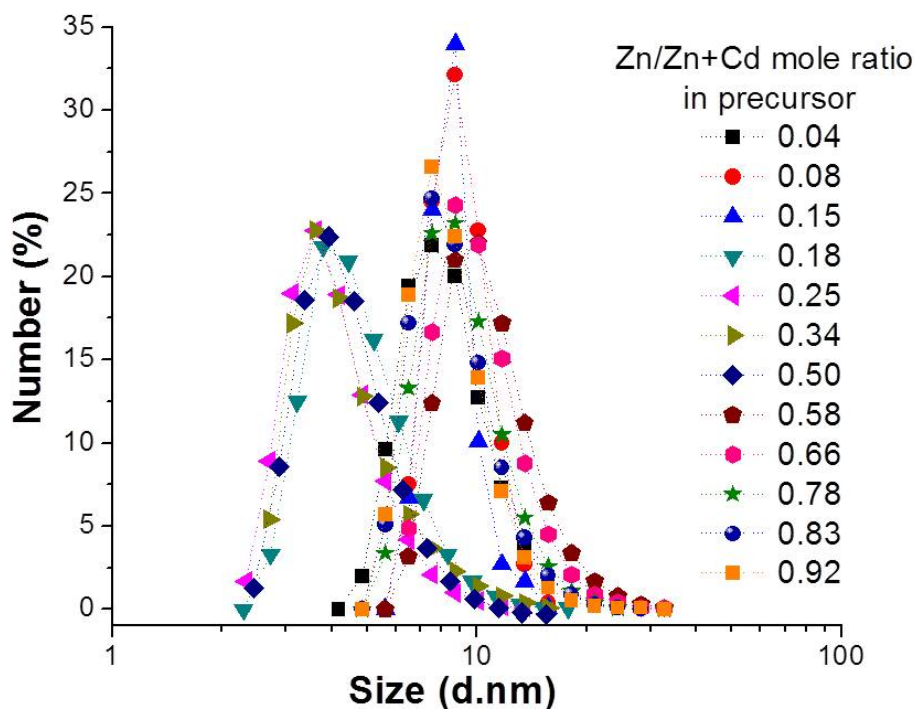


Figure 3.9. Size distributions of the nanoalloys obtained from different initial Zn/Zn+Cd mole ratios.

Growth of the nanoalloys also was monitored by DLS. 1.0 ml of crude colloidal solution of nanoalloys was placed in disposable plastic cuvette and the size of spherical shaped nanoalloys was measured by Zeta Sizer. At the first four initial conditions the particle size was fixed to $\sim 4.5 \pm 1.4$ nm and for the other sets the nanoalloys were grown to around $\sim 9.5 \pm 2.4$ nm by changing the growth time. The results are shown in Figure 3.9. The 4.5 ± 1.4 nm sized nanoalloys could be grown to bigger size by regulating the reaction time. It was found that the particle size varied depending on initial concentration of metal precursor and the growth time.

Within the same growth time, nanoalloys synthesized with low initial Zn/Zn+Cd mole ratio had smaller size than the nanoalloys synthesized from high initial Zn/Zn+Cd mole ratio. The nanoalloy's nuclei initiated with high amount of Cd has slower growth rate compared to nanoalloys nuclei initiated with high amount of Zn. The reflux time

varied between 90 min to 300 min. At high initial Zn/Zn+Cd mole ratio, the reflux time was short to reach a certain sized nanoalloys. Reflux time is not the only factor that affects the size distribution. The size distribution of nanoalloys will be affected whether ternarification occurs via doping to the tetrahedral (T_d) holes inside the Cd(Zn)Te binary crystal or through interchanging the cation places. The reflux process was continued to reach certain sized nanoalloys. The final size of the nanoalloys was obtained by quenching the reflux. For fixed sized nanoalloys the optical response will be influenced by the composition. Therefore size of the nanoalloys were tried to be fixed for the composition dependent investigations.

The size and the shaped of the nanoalloys were determined by STEM and TEM. Unpurified nanocrystals were used during this microscopic analysis. According to Zeta potential analysis the surface of the nanoalloys are negatively charged because of presence of $-COO$ groups of thioglycolic acid. The zeta potentials of the nanoalloys vary from -60 mV to -45 mV. After purification process, the zeta potential of the nanoalloys is reduced from ~ 60 mV to ~ 35 mV. So the nanoalloys exhibit agglomeration after purification. To redisperse the purified nanoalloys into water, we tried to adjust the pH of water to ~ 11.0 by buffer solution. STEM images (Figure 3.10(a-b)) show that the nanoalloys also agglomerate in pH-adjusted water solution. But here the agglomeration is in controlled manner.

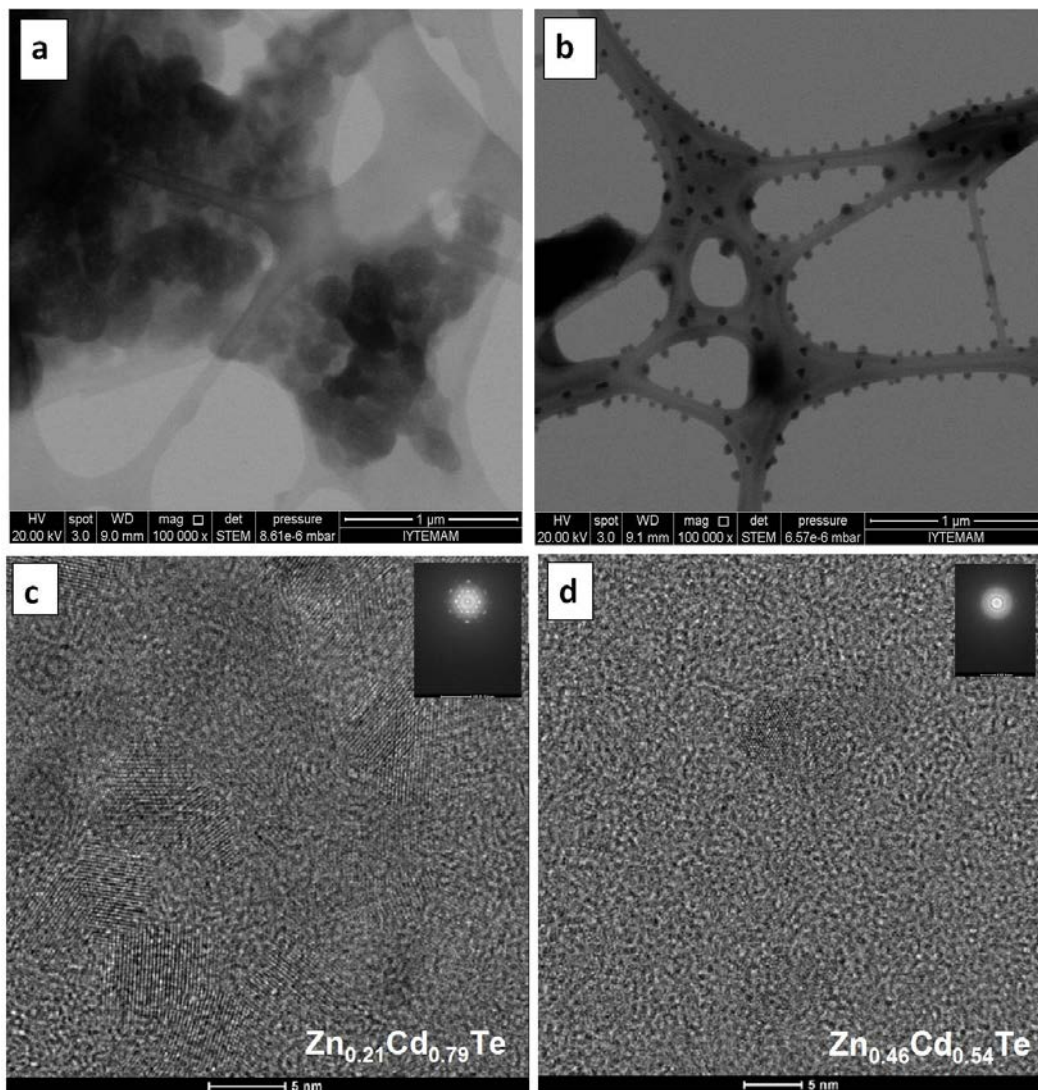


Figure 3.10. STEM images of $\text{Zn}_{0.18}\text{Cd}_{0.82}\text{Te}$ nanoalloys at $1\mu\text{m}$ scale (a) redispersed in pure water (b) redispersed in pH-adjusted water (c-d) HRTEM images of $\text{Zn}_{0.21}\text{Cd}_{0.79}\text{Te}$ and $\text{Zn}_{0.46}\text{Cd}_{0.54}\text{Te}$ nanoalloys at 5nm scale. The inserts illustrate an electron diffraction pattern taken in the same area.

Figure 3.10(c-d) represents the high resolution transmission electron microscopy (HRTEM) images of TGA-capped $\text{Zn}_{0.21}\text{Cd}_{0.79}\text{Te}$ and $\text{Zn}_{0.46}\text{Cd}_{0.54}\text{Te}$ nanoalloys with an emitting wavelength at 550 nm and 600 nm , respectively. The images presenting that the TGA-capped nanoalloys were crystalline, monodisperse, spherical and well separated, with a mean size of the $\text{Zn}_{0.21}\text{Cd}_{0.79}\text{Te}$ and $\text{Zn}_{0.46}\text{Cd}_{0.54}\text{Te}$ nanoalloys are less than 5 nm and 10 nm , respectively. Moreover, the results from electron diffraction (ED) pattern provide further evidence for recognizing the zinc blend crystal phase. The high uniformity of the nanoalloys and high symmetry of ED pattern shows the formation of defectless lattices.

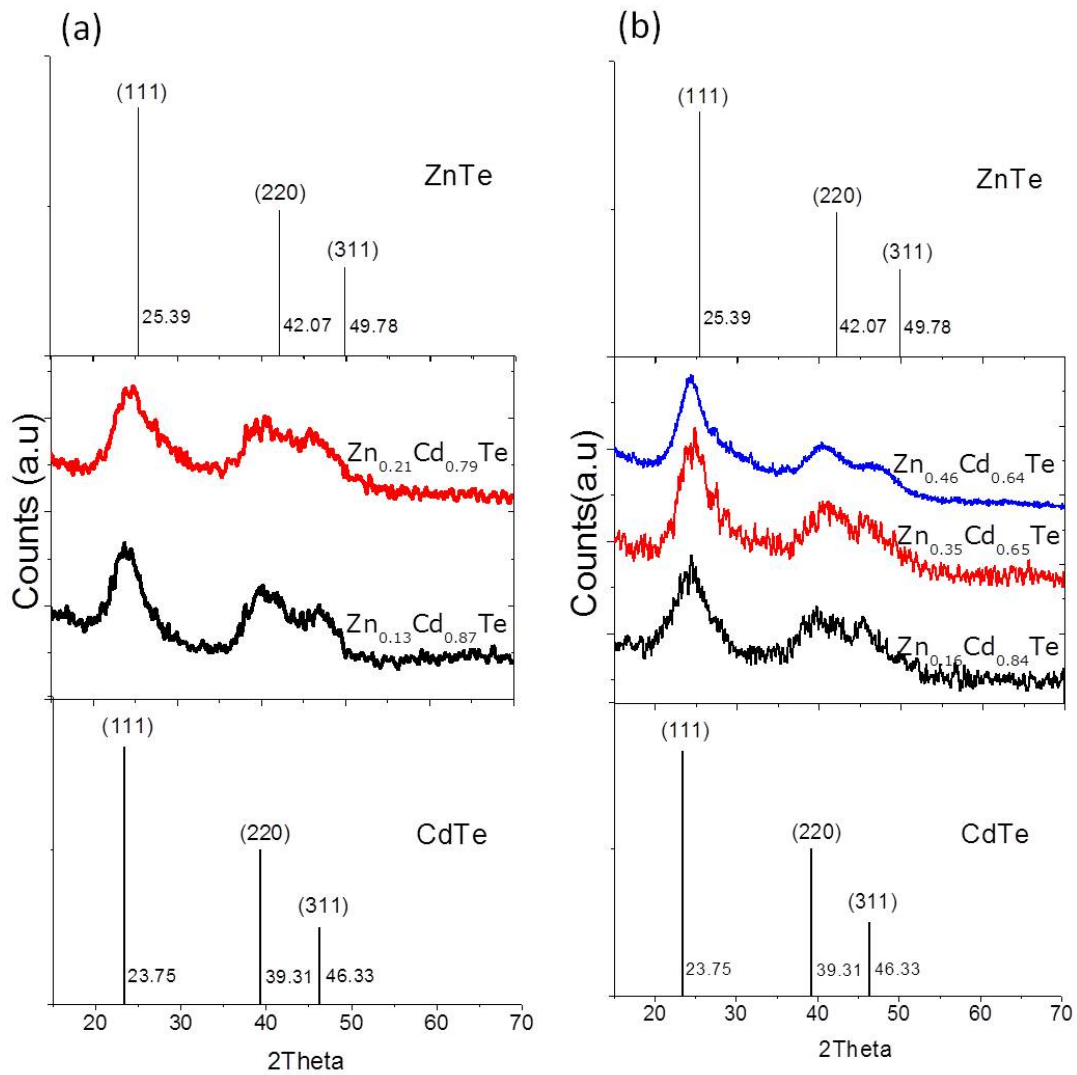


Figure 3.11. X-Ray powder diffraction patterns of (a) homogeneous $Zn_xCd_{1-x}Te$ nanoalloys (b) heterogeneous $Zn_xCd_{1-x}Te$ nanoalloys synthesized by using different amount of Zn/Zn+Cd precursor ratio. Powder patterns of cubic CdTe (PDF card # 150770) and cubic ZnTe (PDF card # 752085) are included for comparison in the bottom and top inserts, respectively.

X-ray powder diffractometer were used to analyze the crystal structure of nanoalloys. Doping or alloying of a crystal does not result in appearance of new X-ray diffraction peaks but instead leads to gradual shifts in lattice parameters of the host material as the concentration of dopant/replaced concentration increases. Figure 3.11(a) shows XRD patterns of homogeneous $Zn_xCd_{1-x}Te$ nanoalloys with the Zn fractions of 0.13 and 0.21. In Figure 3.11(b) XRD patterns of heterogeneous $Zn_xCd_{1-x}Te$ nanoalloys with the Zn fractions of 0.16, 0.35, and 0.46 were provided. It is observed that the nanoalloys have a cubic zinc blend structure, with the presence of characteristic (111), (220), and (311) peaks in the XRD patterns. In the bottom and top inserts of Figure 3.11

characteristic powder pattern of bulk CdTe and ZnTe are shown, respectively. In the bulk crystals the peaks are very narrow. Broadening of the peaks indicates the small size of the nanoalloys. As the Zn content in homogeneous nanoalloys increases, the 2θ values of the characteristic peaks shift to larger angles to some extent and the shifting is easily seen in Figure 3.11(a). The systematic shifting of the diffraction peaks toward larger angles as the Zn content increases (Figure 3.11(a)) is indication of the decrease in lattice parameter due to the smaller ionic radius of Zn relative to that of Cd and is consistent with the Vegard's law. On the other hand the extent of shifting is not pronounced in heterogeneously formed nanoalloys (Figure 3.11(b)). The extent is related with internal crystal structure. With the assumption of having homogeneous crystal structure, lattice constants, and compositions of nanoalloys were calculated by Vegard's law. The cell parameter of binary CdTe and ZnTe NCs are 6.481Å and 6.070Å respectively. Calculated cell parameter of nanoalloys varies between 6.052 to 6.347Å. The results were not consistent with the parameters calculated by using x values obtained by ICP-AES analysis. It shows that internal structure of the nanoalloys has gradient composition. So the Vegard's law is not applicable for heterogeneous structure. There is no linear relationship between the a -axis values of the alloys and x values.

There was both linear and nonlinear relationship between the band gap energy and the composition obtained from XRD patterns. It shows that some of synthesized nanoalloys have heterogeneous crystal structure. The nonlinear relation is known as "bowing". In a study (Tit et al. 2009) the absence of bandgap bowing in the common-anion II–VI semiconductor ternary alloys is investigated and have shown in theoretical calculations on the $Zn_xCd_{1-x}Se_{1-y}Te_y$ and $Zn_xCd_{1-x}S_{1-y}Se_y$ quaternary alloys that the bandgap energy possesses a bowing character when only the anion mole fraction (y) is varied, while it follows almost a linear variation when only the cation mole fraction (x) is varied. Similar bowing and linear behaviors were also reported in the experimental work on the common-cation and common-anion II–VI ZnTe-based alloys (Rozale et al. 2009).

The surfaces of the particles have been stabilized by thioglycolic acid. Infrared spectroscopy was used to determine functional groups on the surface of nanoalloys. Figure 3.12 shows FTIR spectrum of TGA and TGA-capped $Zn_xCd_{1-x}Te$ nanoalloys. Infrared spectra of TGA display a sharp peak at 1720 cm^{-1} which indicates the presence of C=O (Song et al. 2008). Also, there is a peak at 2560 cm^{-1} (S-H) in free TGA. The

peak disappears in $Zn_xCd_{1-x}Te$ nanoalloys and it implies the bonding of TGA to the nanoalloys. TGA-capped $Zn_xCd_{1-x}Te$ nanoalloys display characteristic peaks at 1230 cm^{-1} , 1350 cm^{-1} , and 1550 cm^{-1} . These absorption peaks are ascribed to C-OH, C-O and C=O respectively. According to the spectrum –SH groups of TGA are directly bounded to metal centers and vibrational frequency of the TGA-capped nanoalloys show shifting respect to that of pure TGA. The extent of shifting is related with the number and the type of metals directly bound to the –SH groups of TGA. The nanoalloys having highest fraction of Zn in the structure have characteristic vibration at lower wavenumber (cm^{-1}).

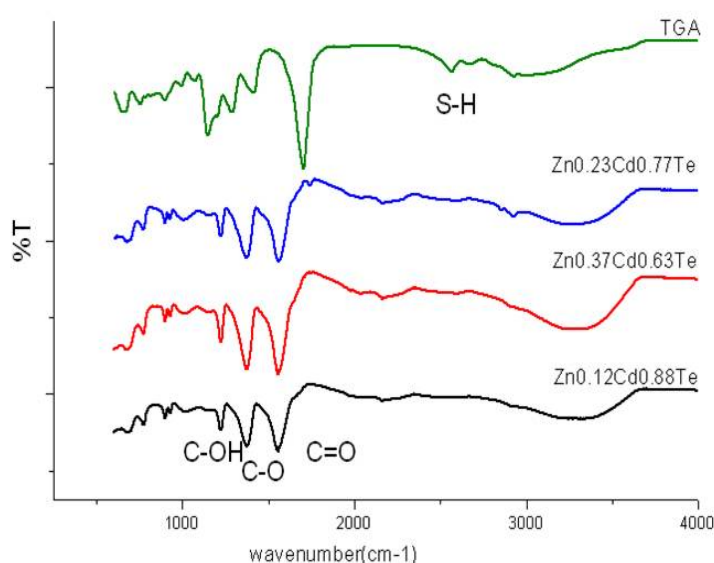


Figure 3.12. FTIR spectrum of TGA and TGA-capped $Zn_xCd_{1-x}Te$ nanoalloys.

The optical properties of the colloidal semiconductor nanoalloys can be modulated by size and composition of the alloyed nanocrystal. To monitor the optical modulation of the nanoalloy, the spectroscopic and structural techniques were employed by taking aliquots of samples during the reaction progress. Figure 3.13 represents the optical and structural properties as well as the temporal evolution of the nanoalloys $Zn_{0.12}Cd_{0.88}Te$, $Zn_{0.18}Cd_{0.82}Te$, $Zn_{0.46}Cd_{0.54}Te$, and $Zn_{0.56}Cd_{0.44}Te$ (determined by ICP-AES) capped by thioglycolic acid.

Normalized absorption and photoluminescence spectra the nanoalloys with different compositions are displayed in Figure 3.13. For optical characterization all nanoalloys were dispersed in water. The UV-Vis absorption spectra were collected between 300 and 700 nm. The PL spectra were collected between 425 and 800 nm using

an excitation wavelength of 400 nm. All nanoalloys synthesized from different initial metal concentration have similar Gaussian shaped absorption and photoluminescence spectra. Figure 3.13a show the typical absorption and PL spectra of the $Zn_{0.12}Cd_{0.88}Te$ nanoalloys sampled at different reaction times varied from 5 min to 200 min. The absorption wavelengths were tuned from 495 nm to 525 nm while the PL maxima of the nanoalloys shifted from 520 nm to 560 nm with longer reaction time (the size increased and the metal variation is constant during the growth time (Figure 3.13a-insert)). The red-shift from 520 nm to 560 nm in the PL spectra inferred the size dependency of the nanoalloys, by DLS measurements. It is proven that the spectral shift is a result of change in the size of the nanoalloy. Absence of any shoulder or broader band in the photoluminescence spectra arising from the energy levels showed the formation of defect-free surface structure at all. The full width at half maxima of the PL spectra was about 25-35 nm. The Stokes shift increased gradually with longer reaction time.

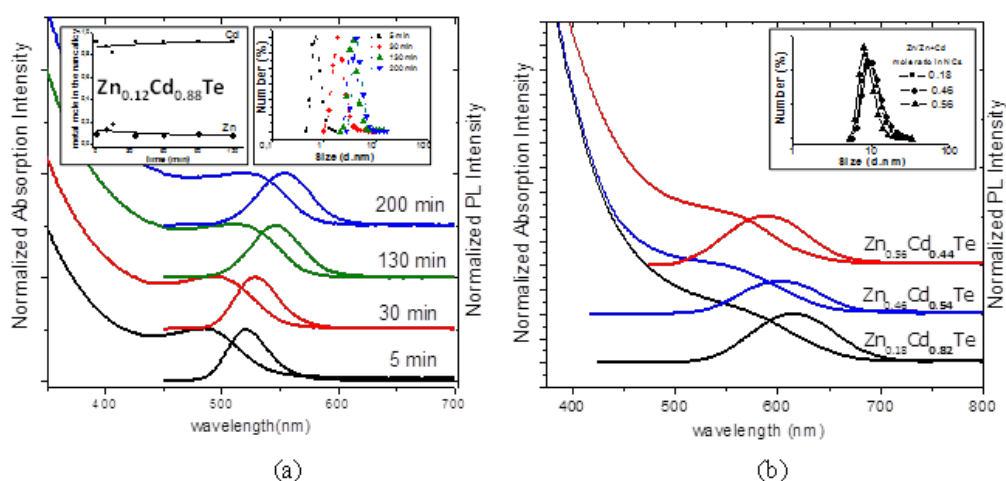


Figure 3.13. (a) Normalized UV-Vis and PL spectra of the $Zn_{0.12}Cd_{0.88}Te$ nanoalloys through growth. The nanoalloys were grown for 200 min. Insert: Change in respective mole ratios of Zn and Cd in the NCs by ICP-AES and DLS measurements (b) Normalized UV-Vis and PL spectra of the 9.5 ± 2.4 nm sized $Zn_{0.18}Cd_{0.82}Te$, $Zn_{0.46}Cd_{0.54}Te$, and $Zn_{0.56}Cd_{0.44}Te$ nanoalloys. Insert: Size distributions of the nanoalloys obtained from different Zn/Zn+Cd mole ratio in precursor.

In Figure 3.13b normalized absorption and photoluminescence spectra of 9.5 ± 2.4 nm sized $Zn_{0.18}Cd_{0.82}Te$, $Zn_{0.46}Cd_{0.54}Te$, and $Zn_{0.56}Cd_{0.44}Te$ nanoalloys are seen. The figure illustrates how the composition tunes the PL peak position of the $Zn_xCd_{1-x}Te$ nanoalloys. The shape of the PL spectra of the nanoalloys was the same; there is only one single emission band. The PL wavelength of the nanoalloys was tuned

from 610 to 590 nm by increasing the fraction of zinc incorporated by varying the respective mole ratio of the Zn and Cd in the precursor mixture, from 0.18 to 0.56. As the Zn content of the nanoalloy increases, systematic blue-shift is observed in the UV-Vis and PL peak position of corresponding same-sized nanoalloys. The systematic blue-shifting with the incorporation of Zn inside the nanoalloys is due to composition change because ZnTe crystals have a wider band gap relative to that of CdTe. It was also observed that there was no additional PL peaks and no emission from the trap states appeared in the spectrum. It is clearly indicative of the formation of $Zn_xCd_{1-x}Te$ nanoalloys rather than the parent binary systems or the core-shell structure. DLS (Figure 3.13b inserts) measurements also prove that the spectral shift is a result of the composition; not due to size.

Photophysical parameters of the synthesized nanoalloys are listed Table 3.4. The listed composition values of the nanoalloys are the values determined by ICP-AES. The change in PL maxima and QY with the Zn content of the nanoalloys is represented graphically in Figure 3.14(a) and Figure 3.14(b), respectively. Quantum yield of the nanoalloys were measured by using Rhodamine 6G in water as a standard (the reference quantum yield of 0.98). The similar size nanoalloys emit light at different wavelength. For fixed sized nanoalloys (4.5 ± 1.4 nm and 9.5 ± 2.4 nm) the optical response was influenced by the composition (Figure 3.14a). The nanoalloys having low Zn content have blue shifted PL max. The relationship between the PL wavelength and the number of incorporated Zn is not completely linear. The blue-shift in PL wavelength is observable for the Zn-poor small-sized nanoalloy.

Photophysical parameters of the nanoalloys are affected by composition of the nanoalloys. In the study the effective change in the PL characteristic was observed at both low and high zinc concentration, it could be understood that the ternarification or doping process might be effectively occurred at this condition. Some of the synthesized nanoalloys have higher QY compared to other nanoalloys. The $Zn_{0.21}Cd_{0.79}Te$ nanoalloys have blue-shifted PL emission from 575 nm to 555 nm compared to $Zn_{0.13}Cd_{0.87}Te$. A similar blue-shift is also observed in the PL peak position of $Zn_{0.19}Cd_{0.81}Te$ (λ_{PL} : 547 nm) and $Zn_{0.16}Cd_{0.84}Te$ (λ_{PL} :554 nm), $Zn_{0.14}Cd_{0.85}Te$ (λ_{PL} :550 nm) nanoalloys. The extent of shifting was different for each nanoalloy. With some nanoalloys, instead of blue-shifting, red-shifting was seen. Even $Zn_{0.65}Cd_{0.35}Te$ has more Zn inside its structure compared to $Zn_{0.56}Cd_{0.44}Te$ NCs, it has PL maximum at 630

nm while $Zn_{0.56}Cd_{0.44}Te$ emits light at 590 nm. Both small size and large size nanoalloys exhibit optical bowing which violates the Vegard's Law (Figure 3.14a).

In the literature the photophysical parameters are constructively and linearly affected by the replacement of Zn to Cd in CdS, CdSe, CdTe NCs structures. PL peaks shift to blue region and QY of the NCs decreases as Zn content of NCs increases (Ouyang et al. 2008, Li et al. 2010, Rozale et al. 2009, Zhong, Han, et al. 2003, Sharma et al. 2010, Kim, Park, and Jang 2010). As the Zn content increases stokes shift and FWHM become larger. General trend between the initial respective mole ratio of metals and final ratio have deviations from linearity.

Table 3.4. Photophysical parameters of the nanoalloys with different Cd:Zn ratios (300 μ l samples diluted to 1ml with water).

Size : 4.5 ± 1.4 nm

Initial Zn/Zn+Cd mole ratio	Nanoalloys	UV-Vis max (nm)	PL max (nm)	Stokes shift (nm)	FWHM (nm)	QY (%)
0.18	$Zn_{0.12}Cd_{0.88}Te$	550	580	30	54	53
0.25	$Zn_{0.21}Cd_{0.88}Te$	530	550	20	51	45
0.34	$Zn_{0.35}Cd_{0.65}Te$	540	590	50	49	20
0.50	$Zn_{0.13}Cd_{0.87}Te$	545	575	30	47	49

Size : 9.5 ± 2.4 nm

Initial Zn/Zn+Cd mole ratio	Nanoalloys	UV-Vis max (nm)	PL max (nm)	Stokes shift (nm)	FWHM (nm)	QY (%)
0.04	$Zn_{0.16}Cd_{0.84}Te$	523	554	31	52	43
0.08	$Zn_{0.19}Cd_{0.81}Te$	519	547	28	49	41
0.15	$Zn_{0.14}Cd_{0.86}Te$	519	550	31	51	46
0.58	$Zn_{0.46}Cd_{0.54}Te$	565	600	45	53	27
0.66	$Zn_{0.18}Cd_{0.82}Te$	580	610	30	41	16
0.75	$Zn_{0.35}Cd_{0.65}Te$	589	625	36	69	13
0.83	$Zn_{0.65}Cd_{0.35}Te$	584	630	48	72	9
0.92	$Zn_{0.56}Cd_{0.44}Te$	572	590	25	70	17

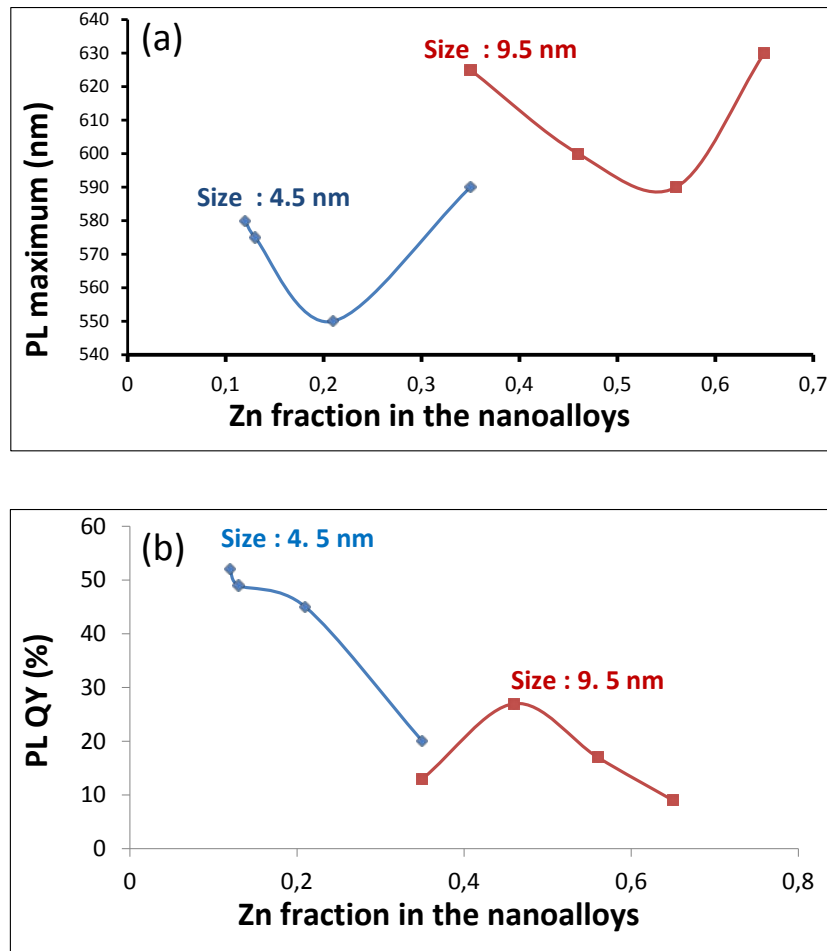


Figure 3.14. Graphical representation of (a) the change in PL peak position (b) the change in QY with the fraction of Zn in the nanoalloys (Table 3.4).

There is a decrease in QY of the nanoalloys with the increasing amount of Zn. The lower quantum yield was hypothesized to the increased structural disorder induced by excess amount of Zn incorporated into the nanoalloy. Zn is more electronegative than Cd, which is why Zn act as a quencher and it pulls the electrons towards itself. The quencher decreases the QY of the nanoalloys.

The $\text{Zn}_{0.19}\text{Cd}_{0.81}\text{Te}$ (λ_{PL} : 547nm) and $\text{Zn}_{0.18}\text{Cd}_{0.82}\text{Te}$ (λ_{PL} : 610nm) nanoalloys have similar composition; their photophysical parameters are completely different from each other. The results showed that there is nonlinear relationship between composition of the nanoalloys and their photophysical properties. The extent of shifting and the nonlinearity depends on type internal structure of the nanoalloy.

Whether the formed alloy crystals are simply homogeneous or heterogeneous, annealing process could be carried out and diffusion of cations inside the structure will be minimized. Optical properties of nanoalloys were enhanced by means of annealing.

During annealing process atoms will rearranged and number of surface and internal defect states will decrease. The precipitated ZnCdTe alloy NCs were redispersed in deionized water to obtain the sample with 330 mg/L, 110 mg/L, and 37mg/L of ZnCdTe. The experiments were conducted in these concentration groups at three different temperatures (343, 353, and 363 K). UV-Vis absorbance spectra were used to record the behavior of nanoalloys in aqueous solution.

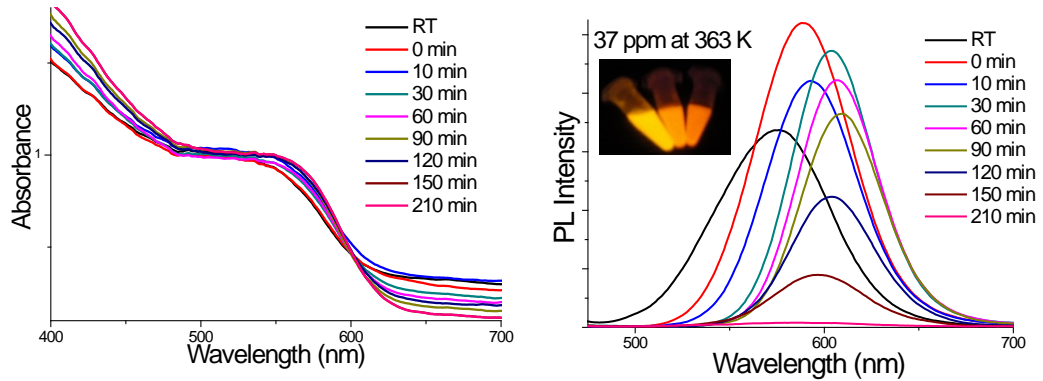


Figure 3.15. The typical UV-Vis spectra (left) and PL (right) spectra of the $Zn_xCd_{1-x}Te$ nanoalloys solution with particle concentration of 37 mg/L from room temperature and 0 to 210 min at 343K. (Insert: picture of the annealed nanoalloys under UV light).

Figure 3.15 shows the typical evolution of UV-Vis absorbance and PL spectra of $Zn_xCd_{1-x}Te$ nanoalloys during the annealing process from 0 to 210 min. It shows that the absorption edge of UV-Vis absorption spectra has a red-shift, which implies that either the nanoalloys are growing or atoms are rearranged inside the crystals. The average particle sizes of the $Zn_xCd_{1-x}Te$ nanoalloys were estimated from UV-Vis spectra using the absorption edge method (Pesika et al. 2003), with the variation of bandgap (ΔE_g) in the $Zn_xCd_{1-x}Te$ nanoalloys as a function of diameter (d) (Viswanatha et al. 2005), ($\Delta E_g = 1/(0.0275d^2 + 0.2403d + 0.1469)$).

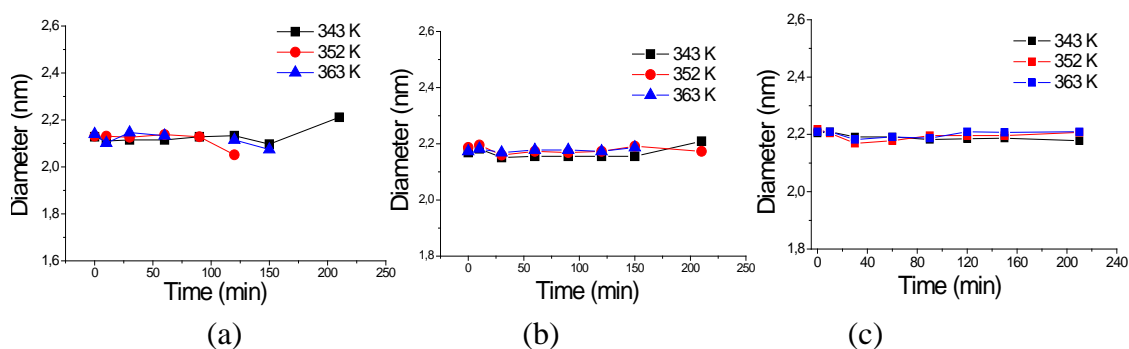


Figure 3.16. Experimental data of variation in the sizes of $Zn_xCd_{1-x}Te$ nanoalloys as a function of time for three different primary concentrations of (a) 37mg/L, (b) 110mg/L, (c) 330mg/L.

As shown in Figure 3.16 the growth curves of $Zn_xCd_{1-x}Te$ nanoalloys were obtained for three concentration samples at three different temperatures (343, 353, and 363 K). For each system, we can clearly see that increasing temperature does not affect the particle size. Also the changes in size of the $Zn_xCd_{1-x}Te$ nanoalloys are time - independent at these temperatures. In order to see the influence of primary particle concentration on the rearrangement of the atoms in $Zn_xCd_{1-x}Te$ nanoalloys, average particle sizes against particle concentration at varied growth time points were extracted and plotted in Figure 3.17.

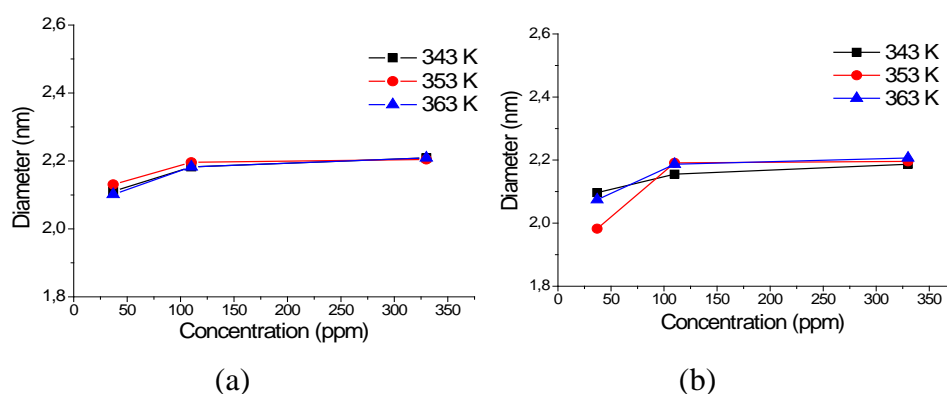


Figure 3.17. Average diameters, d , of the TGA-capped $Zn_xCd_{1-x}Te$ nanoalloys (a) at 10 min of the initial heating stage, and (b) at 150 min of the latter heating stage vs primary particle concentrations at different temperatures (343, 353, and 363K).

It is known that if the alloy is homogenous, during heating PL maximum should stay constant. If not, the PL peaks are shifting due to the rearrangement of atoms inside the crystals. According to the annealing results, the $Zn_xCd_{1-x}Te$ nanoalloys have

unhomogeneous internal structure. The initial red shifting in UV-Vis and PL maxima might indicate structural rearrangement. The increase in PL intensity indicates the diminution in defective states and the quantum yield increase in by a fraction of 15%. Further heating results in blue--shifting and it will be due to rearrangement of atoms. Through further heating, particles lost their emission properties. In a research, the similar experiment is done for CdTe NCs in H₂O which shows that increasing temperature facilitates the particle growth of CdTe and the particle size increases due to oriented attachment of NPs to each other (Yin et al. 2011). Contrary to this study, the size of Zn_xCd_{1-x}Te nanoalloys did not change with temperature and concentration.

Photostability of the Zn_xCd_{1-x}Te nanoalloys and their QY can be improved by coating with CdS shell by adding thiourea (S source) to the Zn_xCd_{1-x}Te nanoalloy crude solution at 110⁰C under N₂ atmosphere as in the case of coating of CdTe with CdS. All Zn_{0.21}Cd_{0.79}Te ternary nanoalloys coated with CdS and as coating it was seen that the diffraction angle of most intense peak shifts to that of CdS. But the shell is not simply CdS .The shell should include both cation in its structure. As supposed the quantum yield was increased from 42% to 51%.

3.4. Conclusion

Accounts on the synthetic chemistry of Zn_xCd_{1-x}Te nanoalloys were very limited and we developed a new way to synthesize highly luminescent colloidal Zn_xCd_{1-x}Te ternary nanoalloy. The one-pot approach was applied at low temperature compared to organometallic-hot injection technique. Ternary thiol-capped Zn_xCd_{1-x}Te nanoalloy has been synthesized by changing the respective mole ratio of metal (Zn/Zn+Cd) in precursors from 0.04 to 0.92. During the synthesis total amount of metal precursors was kept constant at 3.12 mmol and the respective mole ratios of Zn/Cd in the precursor mixture were changed. It was modulated from 0.12 to 0.65. The fractions of incorporated Zn in the nanoalloys were verified by ICP-AES. The size- and composition-tunable optical properties of the Zn_xCd_{1-x}Te nanoalloys were characterized.

The photophysical parameters of the nanoalloys are affected by final mole ratio of Zn²⁺ to Cd²⁺ inside nanolloy structure. The PL peak positions, the quantum efficiency, and internal structure are affected by the replacement of Zn in Cd position in

the crystal. The steady-state spectroscopic analyses of the nanoalloys show that composition-tunable $Zn_xCd_{1-x}Te$ nanoalloys exhibit highly luminescent properties with high quantum yield (up to 53%). The QY of the nanoalloys could be improved by coating with CdS shell or by annealing for suitable time. These processes enhanced the QY more than 10%.

PL of the nanoalloy is tunable from 520 to 620 nm by either the size or the alloy composition. The size of the nanoalloy is varied from 2.0 ± 0.8 to 9.5 ± 2.4 nm, determined by DLS measurements. DLS measurements showed that the size distribution of the nanoalloys is highly monodisperse and TEM images confirmed the size and size distribution of the nanoalloys. We suggest that the composition of the nanoalloy is modulated by adjusting the amount of metal precursors and the alloying process depends on the reactivity of precursor toward Te anions. The Cd-rich homogeneous nanoalloys are formed when the initial mixture of the metal precursor contains lower amount of Zn. The Zn-rich nanoalloys are formed at high Zn/Zn+Cd mole ratio in the precursor solution. It was noted that the reactions with lower Zn precursors were reproducible and controllable. The nanoalloys obtained from low amount of initial (Zn/Zn+Cd) mole ratio have narrow spectral width, (FWHM: 40-55 nm), whereas the nanoalloys synthesized from higher amount of (Zn/Zn+Cd) initial mole ratio have wide spectral width, (FWHM: ~72 nm). All nanoalloys have zinc blend structure. They have composition- and size-dependent band gap energies.

We note that the magnitude of the QY falls as the size is increased to 10 nm and number of incorporated Zn is increased, the larger surface area and uncoordinated Zn may introduce surface defects reducing the radiative rate constant which correlates QY values.

CHAPTER 4

EXCITON DYNAMICS OF COLLOIDAL

Zn_xCd_{1-x}Te NANOALLOYS

4.1. Introduction

Nanocrystals have been under intense investigation as a subject of basic science (Knowles et al. 2012) and application in technology such as light-emitting devices (Colvin, Schlamp, and Alivisatos 1994), low threshold lasers (Klimov et al. 2000; Klimov et al. 2007), biological labels (Bruchez et al. 1998), and photovoltaic cells (Farrow and Kamat 2009). The electronic structure and optical properties of nanometer-sized materials is adjustable. The tunable energy spectrum suggests that the time scales and pathways by which the excited carrier relaxes may be unique (Nozik 2001; Kambhampati 2011). Exciton dynamics provide unique information both on the nature of optical transitions and on the local environment of an optically active species.

Photoluminescence lifetime measurements are an important tool to study linear and nonlinear optical behavior of exciton(s) in nanometer scale systems. The time resolved analysis show several discrete features, which could not be pronounced in steady state PL spectra. With time-resolved spectroscopic analysis, one can obtain information on electronic energies, the spectral distribution of photoexcited carriers (excitons), exciton-exciton interaction, carrier energy-relaxation and recombination dynamics (Wang et al. 2009; Maly et al. 2002; Scotognella et al. 2011; Kobayashi et al. 2011; Liu et al. 2011; Sarkar et al. 2007). Decay time constants and spectral distribution provide information about exciton dynamics. The exciton dynamics is related with scattering process from phonons, impurities, defects, interfaces and surfaces, exciton-exciton scattering and also free exciton present in crystal.

The subject of the work is to study exciton dynamics and exciton-exciton interactions by varying composition and size of alloyed semiconductor nanocrystals. The time range of non-radiative relaxation processes of excitons and energy transfer processes varies in femtoseconds and/or picoseconds. The radiative recombination processes in excitonic systems is usually about nanosecond.

For binary systems, the dynamics and the interactions can be varied by the size of NCs. In the study of Rajesh *et al.*, exciton recombination time of three different sized ZnSe QDs have been measured and it has been found that the recombination time shows biexponential decay and the decay time decreases with the reduction in quantum dot sizes (Rajesh et al. 2008). In another study, Viale and his coworkers studied on population dynamics in CdTe/ZnTe QDs by pump-probe technique. They found that exciton transfers from ZnTe to CdTe within 2 ps and it is interpreted as an indication of carrier localization corresponding to energy minima. Thermalization of exciton from the excited state to the lowest excitonic states occurs in 20-25 ps. Also dephasing (due to Auger recombination) dynamic analysis of the excitons showed that when the excitation intensity increases the weight of the fast component increases with respect to slow one because more than one exciton was created (Y.Viale et al. 2003). Energy density and photon density should determine the number of formed excitonic states.

The carrier dynamics and their lifetime are not only size dependent but are indeed also composition dependent (Klimov V. 2000, Califano et al. 2005). Radiative recombination lifetimes of CdSe, CdS and CdSSe are different. The lifetime decreases with an increase in the sulfur fraction of CdS_xSe_{1-x}. It is simply explained by electron-hole mobility due to the difference in the effective mass of the electron and hole (m_h (CdS):0.7 and m_h (CdSe):0.4) in the individual materials. According to effective mass, CdS should have longer lifetime than CdSe. The defective states with S content in CdSSe results in decrease in radiative recombination lifetime

In literature Cd- and Pb-based semiconductor NCs have been studied in terms of both synthesis and exciton dynamics (Liu et al. 2011; Fitzmorris et al. 2012; Miaja-Avila et al. 2012; Gao et al. 2011; Yan, Chen, and Van Patten 2011). In CdSe NCs, Auger recombination leads to the deactivation of doubly excited nanoparticles within time from 400 ps to 10 ps, depending on the NC size. The smaller the size of NC, the faster the recombination of e-h pair (Klimov V. I. 2007). Any change in the size and the lattice parameters of the crystal affects both the splitting energy between dark and bright state. The splitting completely influences the behavior of carrier dynamics. For 1.5 nm CdSe NCs the splitting energy is about 1.7 meV and for 6 nm NCs the energy is about 0.7 meV. The four types of QDs; CdS (zinc blende), PbSe (rock salt), CdSe (wurtzite), Ge (diamond) have different splitting at their lowest excitonic states. It is predicted that a dark state is the lowest energy exciton state in PbSe NCs and bright state is the lowest energy exciton state in Ge. Coating also affect the exciton recombination lifetime. As

the size of NCs decreases, the recombination decay rate of e-h pair increases. The coating of CdSe core with a ZnS shell results in increase of exciton recombination the lifetime even the CdSe and CdSe/ZnS NCs have the same size. (Califano et al. 2005 and Fisher et al. 2005).

Energy density and photon density determine the number of excitons formed. In CdSe NCs, when the e pump fluence is 3.4 mJ cm^{-2} per pulse, multiple excitons (more than three excitons) were created in the excited states per NC on average (Fisher et al. 2005). Dynamical analysis of exciton shows that there was increase in the weight of the fast component with the excitation intensity due to formation of more than one exciton. The relaxation rate of these multi-exciton states is extremely fast (ps time scale) due to Auger quenching processes. The decay rate depends on size of spherical NCs and it is getting longer for larger particles (150 ps for 3.4 nm CdSe and 50 ps for 2.3 nm CdSe QDs). Also the radiative decay time values of bi-exciton and tri-excitons 5.1 nm sized CdSe core shell NCs are 8.4 ns and 6.8 ns, respectively. When the photon fluence is $j_p=10^{12}$ photon/cm² per laser pulse, the average number of exciton in each NCs is less than 1 ($N_0 < 1$), i.e. the case of single exciton (Fisher et al. 2005).

In order to get detailed information about the exciton dynamics of the colloidal $\text{Zn}_x\text{Cd}_{1-x}\text{Te}$ nanoalloys were analyzed by ultrafast multidimensional fluorescence spectroscopy using a streak camera system (Figure 4.1) at the MicroSpectroscopy Centre (MSC) in Wageningen, the Netherlands.

4.2. Experimental Setup

Picosecond fluorescence spectra measurements were performed using a synchroscan streak camera system (Figure 4.1). The basic aim of the streak camera set up is to determine simultaneously time-resolved emission spectrum and decay times information. The temporal resolution of the synchroscan streak camera system is 2 ps. The set-up consist of the mode-locked lasers and a synchroscan streak system as a detection part equipped with a spectrograph (Chromex, Albuquerque, NM model 250is) and a digital CCD camera (Hamamatsu model C4742-95-12NRB). A streak system commonly referred to as a Streak Camera (Hamamatsu, Hamamatsu, model C5680-24S), in an ultrafast photonic recorder with time resolution down to 200 femtoseconds with photon counting sensitivity. Simultaneous recording of photonic temporal behavior

is possible over a defined spatial dimension, or wavelength information when coupled to spectrograph.

Excitation light pulses were obtained with a set of lasers and optical amplifiers from Coherent Inc., Santa Clara, CA, USA. A mode-locked Ti: Sapphire laser model Mira 900 was used to generate long light pulses of 400 nm, duration of about 150 fs and repetition rate of 79.5 MHz.

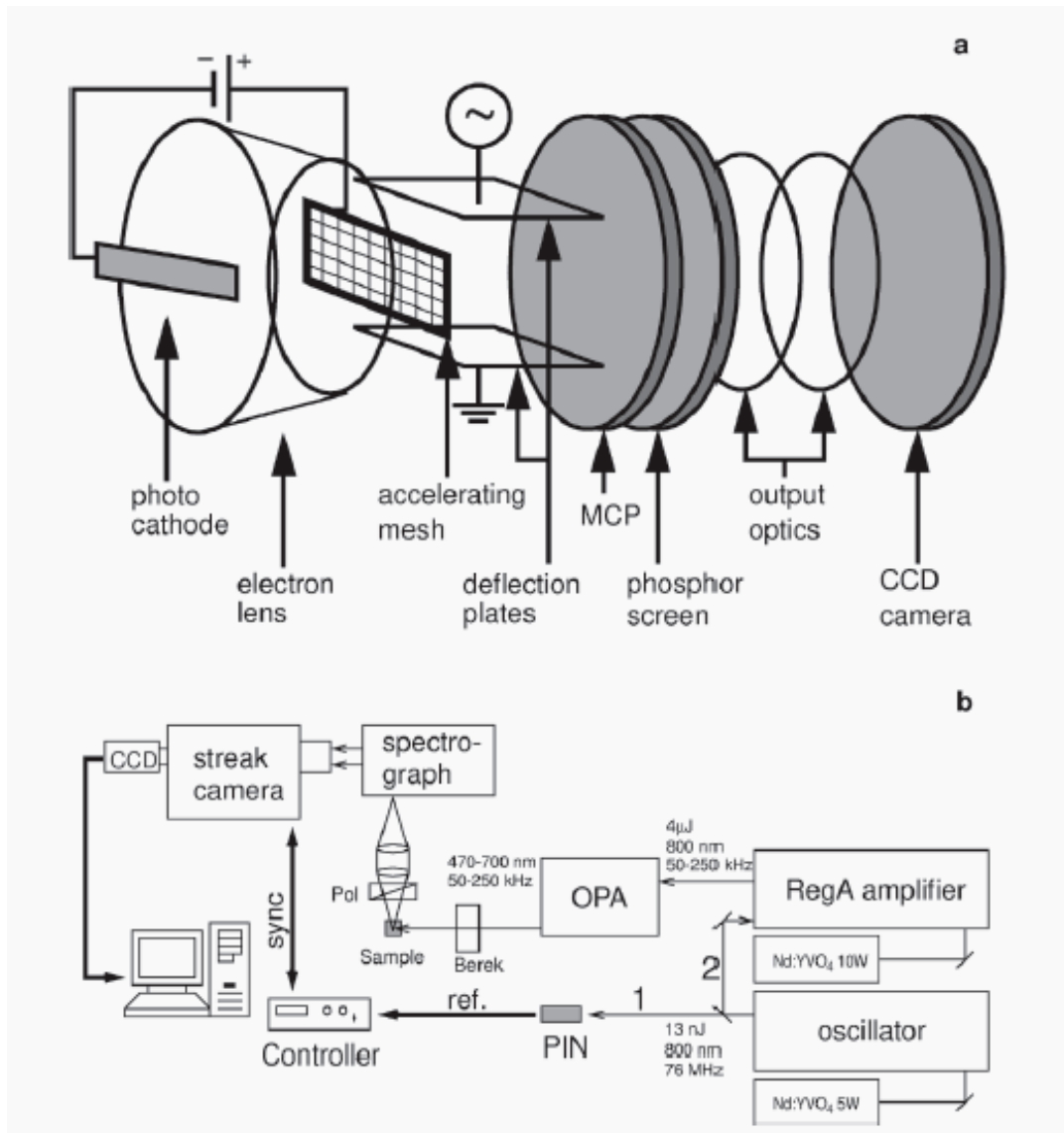


Figure 4.1. Schematic representation of (a) a streak camera and (b) the synchroscan streak-camera setup in Laboratory of Biophysics, Wageningen University, Wageningen, The Netherlands. PIN: photodiode (Source: van Stokkum et al. 2008).

A small fraction of the output-intensity of this laser is used for synchronization with a sweep field in the streak camera, while the major part was fed into a regenerative amplifier model RegA 9000, where the energy of the pulses is increased while the repetition rate is decreased to 250 kHz. Continuous wave solid state lasers (Coherent Verdi V5 and Coherent Verdi V10) were used to pump a Mira and RegA, respectively. The output of the RegA is directed to an optical parameter amplifier (OPA 9400) which is used to produce excitation pulses of all wavelength 400 nm. The average output of the OPA was changed from microwatt (10^{14} photons/cm²) to a hundred mW (10^{17} photons/cm²). The light intensity was modulated with neutral density filters and residual white light of the OPA was removed with an interference filter.

In front of the streak camera an imaging spectrograph was mounted (model 250is, Chromex, Albuquerque, NM, USA). Fluorescence emission was focused into the input slit of the spectrograph, using two identical achromatic lens assemblies (model UV APO special, $f = 70$ mm, $d = 22$ mm, Sill Optics, Wendelstein, Germany) placed in a complementary manner with a Glan Taylor polarizer (model GT20, Leysop Ltd., Essex, England) and an optical cut-off filter 490 nm in between to suppress raman scattering. The output of the spectrograph was coupled directly onto the stripe-shaped (height 70 μ m) cathode of the streak-camera (model C5680 with model M5675 Synchronscan unit, Hamamatsu Photonics K.K., Hamamatsu City, Japan).

The detection of fluorescence with a streak camera allows for simultaneous registration of both the time of emission of a fluorescence photon and the emission wavelength. Streak camera output is three dimensional: intensity/time and intensity/wavelength information can be simultaneously obtained by moving the cursor in the time scale and in the wavelength scale, respectively. The wavelength dispersion of the spectrograph was in the horizontal direction, the time dispersion of the streak tube was in the vertical direction (Figure 4.2).

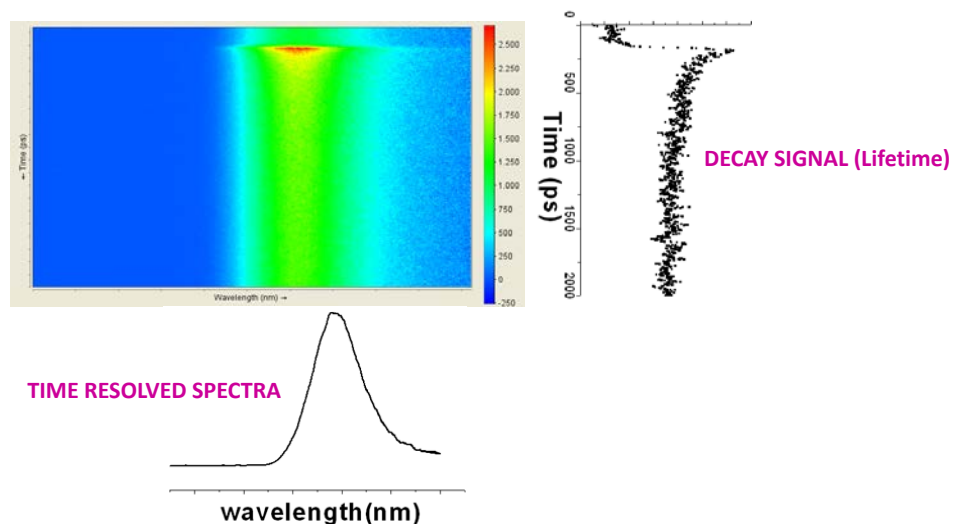


Figure 4.2. Streak images of $Zn_xCd_{1-x}Te$ ternary colloidal nanoalloys (above). Fluorescence intensity of nanoalloys is represented by colors from red (high) to blue (low). The time-resolved emission spectra of the nanoalloys obtained from a picoseconds resolved Streak camera (below). Position resolved decays of the nanoalloys from shorter to longer time windows (right).

4.3. Time-Resolved Measurements of $Zn_xCd_{1-x}Te$ Colloidal Nanoalloys

Time-resolved fluorescence measurements $Zn_xCd_{1-x}Te$ colloidal nanoalloys have been carried out by the Streak camera system. During the analysis 100 microliter colloidal solution of the nanoalloys were diluted with proper amount of ultra-pure distilled water and they were put in the quartz cuvette. The cuvette placed into the sample holder. The measurements were performed without stirring. Spot size of the laser beam was 100 micrometer. The spectral interval varied from 470 nm to 730 nm. The sweep range of the streak camera was 2 ns. Streak camera images of the nanoalloys were measured upon excitation with a 400-nm laser light. Laser power changed from 1 mW to 100 mW during measurement. The streak camera images have been corrected for the instrumental curvature. Then the images have been globally analyzed.

The colloidal nanoalloys have been excited above their band gap with the photons having energy of 3.1 eV (400nm) by changing photon fluence from $j_p=10^{15}$ to 10^{17} photon/cm² using ND filters. Energy density and photon density play a role to determine the number of formed excitons upon exciations in the nanoalloys. As increase the number of photon fluence (laser power), the PL intensity of each nanoalloy increase.

Since the band gap of the NCs have been engineered by changing size and the composition, semiconductor NCs have specific threshold energy for the absorption of the photons. The band gap energies (E_g) of NCs determine the fundamental threshold energy for the absorption. The photons having less energy than the E_g are not absorbed. Excitation of the NCs with photons having $h\nu > E_g$, results in electrons and holes with excess energy. So the electrons and hole are out of equilibrium in terms of energy. The excess energy is distributed between the electron and hole. The distribution is calculated by (Nozik 2001);

$$\Delta E_e = (h\nu - E_g) [1 + m_e^*/m_h^*]^{-1} \quad (4.1)$$

$$\Delta E_h = (h\nu - E_g) - \Delta E_e, \quad (4.2)$$

where m_e^* and m_h^* are the effective masses of electrons and holes, respectively, ΔE_e is the energy difference between the conduction band and the initial energy of the photogenerated electron, and ΔE_h is the energy difference between the valence band and the photogenerated hole. Nozik explains the hot carrier relaxation/cooling dynamics in semiconductors, as depicted in Figure 4.3. The created hot e-h pairs first cooled via thermalization through carrier scattering very rapidly (<100 fs) (Figure 4.3) (Pelouch et al. 1992). It is the fastest process (τ_{fast}). The next process is carrier phonon interaction whereby excess energy of the carriers transferred to phonons to reach equal lattice and carrier temperature and the process (τ_{slow}) is slower than the thermalization process. Finally electrons and holes recombine radiatively or nonradiatively. The photogenerated electron-hole pairs will undergo spatial separation process which is the basis for devices/cells to convert the photon energy into electrical energy (Nozik 2001).

Another schematic representation of possible exciton relaxation in semiconductor NCs by Wu, F. and Zhang Jin is shown in Figure 4.4 (Wu, F. and Zhang Jin Z. 2009). The solid line (1) in the figure with upward arrow indicates photoexcitation. The curved lines with downward arrows show different relaxation processes: (2) electronic relaxation within the conduction band, (3) bandedge electron-hole recombination (4) exciton-exciton annihilation (5) trapping into trap states and (6) trapped electron-hole recombination. The trapped carriers can further recombine radiatively or nonradiatively. Trap states in NCs have lifetimes from a few tens in picoseconds to nanoseconds or longer, depending on the nature of trap states.

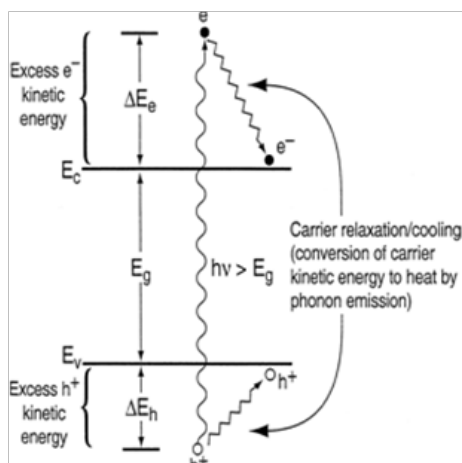


Figure 4.3. Hot carrier relaxation/cooling dynamics in semiconductor (Source: Nozik 2001).

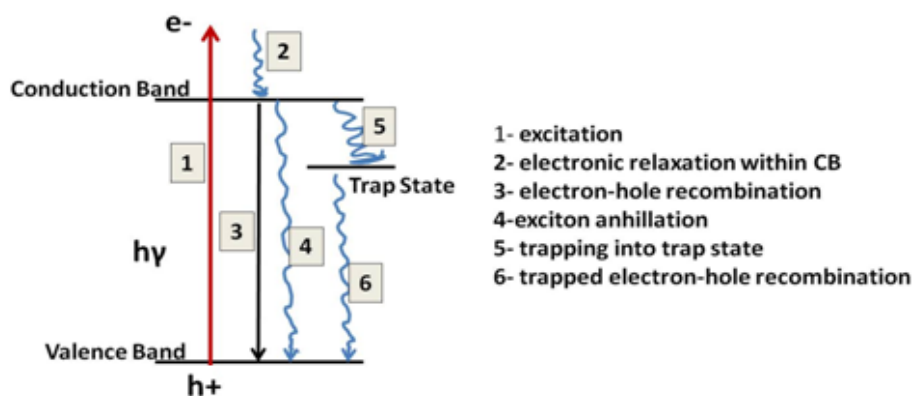


Figure 4.4. Schematic illustration of charge carrier relaxation in semiconductor nanocrystals.

4.4. Results of Time-Resolved Measurements of $Zn_xCd_{1-x}Te$ Nanoalloys

Photophysical parameters, size and type of structure of the measured $Zn_xCd_{1-x}Te$ colloidal nanoalloys have been listed in Table 4.1. Stock solutions of the nanoalloys have been analyzed. Dilution factor was determined to be 1/100. The measurements of crude solution of nanoalloys and weakly diluted nanoalloys showed that the concentration of the nanoalloys have profound effect on lifetime values and the dynamics. In case of concentrated nanoalloys, energy would be transferred between the

individual particles. The energy transfer processes are as fast as exciton dynamics. To minimize/exclude energy transfer and to see the exact effect of laser power on the exciton-exciton interaction, the stock solution of nanoalloys (110 mg / 110 ml) have been diluted with water to obtain the concentration of 10 $\mu\text{g/ml}$. This translates to an average nanoalloy center-to-center distance of much larger than inter-nanoalloy distance in concentrated case. During the measurement of $\text{Zn}_x\text{Cd}_{1-x}\text{Te}$ colloidal nanoalloys with laser power of 100 mW, cut of filter of 12.5% was used to prevent the oversaturation of detector.

Table 4.1. Photophysical parameters of analyzed $\text{Zn}_x\text{Cd}_{1-x}\text{Te}$ colloidal nanoalloys and their size (this information was reached in chapter 3).

Nanoalloys	λ_{abs} (nm)	λ_{PL} (nm)	Size (nm)	QY (%)	Type of Structure
$\text{Zn}_{0.12}\text{Cd}_{0.88}\text{Te}$	550	580	4.50	53	homogeneous
$\text{Zn}_{0.21}\text{Cd}_{0.79}\text{Te}$	530	550	4.50	45	homogeneous
$\text{Zn}_{0.35}\text{Cd}_{0.65}\text{Te}$	540	590	4.50	20	heterogeneous
$\text{Zn}_{0.18}\text{Cd}_{0.82}\text{Te}$	580	610	9.50	41	homogeneous
$\text{Zn}_{0.46}\text{Cd}_{0.54}\text{Te}$	565	600	9.50	27	heterogeneous

Figure 4.5 shows the streak camera images of $\text{Zn}_x\text{Cd}_{1-x}\text{Te}$ colloidal nanoalloys (from up to down) excited with different laser power: 1 mW, 10 mW, 100 mW, from left to right respectively. Each nanoalloys have the highest emission intensity at $t=0$ ps and intensity decreases exponentially. Streak camera images of the $\text{Zn}_x\text{Cd}_{1-x}\text{Te}$ colloidal nanoalloys under low pump intensity, 1 mW, do not significantly differ from each other. The number of particles in the solution and their photoluminescence quantum yield affects the fluorescence intensity.

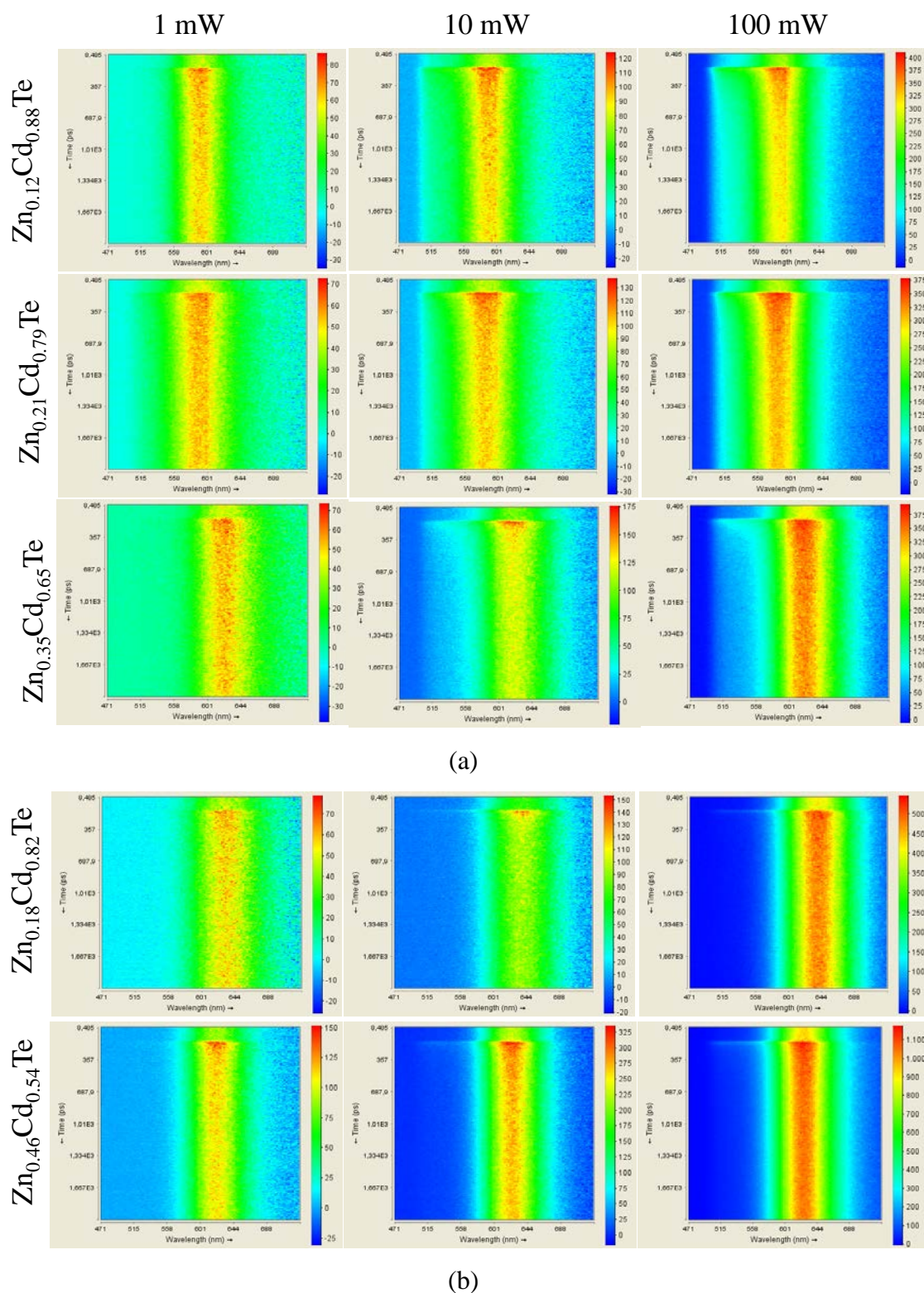


Figure 4.5. Streak camera images of (a) 4.5 ± 1.4 nm sized (b) 9.5 ± 2.4 nm sized $\text{Zn}_x\text{Cd}_{1-x}\text{Te}$ colloidal nanoalloys (from up to down) excited with different laser power: 1 mW, 10 mW, 100 mW, from left to right, respectively. Fluorescence intensity of the nanoalloys is represented by colors from red (high) to blue (low).

It is clear from the streak camera images that the fluorescence of the $\text{Zn}_x\text{Cd}_{1-x}\text{Te}$ colloidal nanoalloys excited under 1 mW laser power are not so intense compared to that of the nanoalloys excited at 100 mW laser power. Each colloidal nanoalloys have the highest emission intensity at $t=0$ ps and intensity decreases with time exponentially. At the same time, a new band at the lower wavelength (higher energy) arises from with the increasing laser power, as seen in the pictures (Figure 4.5). In the streak camera images, it might be difficult to distinguish or see blue-shifted emission.

All dynamic phenomena of excitons reflect on fluorescence spectra. PL intensity of the nanoalloys increases with laser power. The increase in PL intensity is highly dominant when laser power is increased from 80 mW to 100 mW. The change in intensity of the PL, shape of the PL peaks and FWHM proves that exciton exciton interactions exist. The exciton-exciton interaction starts at excitation with 1mW laser power. Blue-shifted band formation and laser power dependency of PL intensity is seen in Figure 4.6. From these spectra it can be seen that there is a new excitonic energy state (pointed by a red arrow in the figure) formed by exciton-exciton interaction in the one-exciton state. The number of photons/cm² varied from 10^{15} to 10^{17} photons/cm² induces exciton-exciton interaction in the nanoalloys. The multiexcitonic state has higher energy than one-exciton state so the shoulder is seen at lower wavelength (blue region). Also the spectra showed that the contribution of the multiexcitonic state (new energy state) increases at high laser power. The excited states (multi-excitonic states) of the nanoalloys were populated with many excitons under higher number of photons. The energy level structure and population dynamics changes from nanoalloy to nanoalloy. In case of smaller sized nanoalloys, the interaction is more dominant with respect to larger size nanoalloys. In the 4.5 ± 1.4 nm-sized nanoalloys, diffusion of excitons is more restricted compared to the larger size nanoalloys. Zn fraction in the nanoalloy determines the extent of exciton-exciton interaction. The contribution of multiexcitonic state in $\text{Zn}_{0.21}\text{Cd}_{0.79}\text{Te}$ is higher than that in $\text{Zn}_{0.12}\text{Cd}_{0.88}\text{Te}$. It shows that as the Zn fraction in the nanoalloy composition increases the exciton-exciton interaction becomes more profound. The formation of blue-shifted peak in 9.5 ± 2.4 nm-sized $\text{Zn}_{0.18}\text{Cd}_{0.82}\text{Te}$ and $\text{Zn}_{0.46}\text{Cd}_{0.54}\text{Te}$ nanoalloys is not as profound as in small size nanoalloys. It is due to weak exciton-exciton interaction (Figure 4.6) since width of the field that excitons diffuse in the nanoalloys is extense. Weakness of the interaction increases the possibility of Auger-process-assisted trapping of exciton in the nanoalloys. In bigger size (9.5 ± 2.4 nm) nanoalloys, as the Zn fraction of nanoalloys increases from 0.18 to

0.46, multiexciton state still forms but not as much significant as in the small size nanoalloys. The weak blue band in the big nanoalloys indicates that exciton-exciton annihilation causes diminution of PL intensity. The exciton-exciton interactions might be via Auger recombination in which two electrons and holes recombine to form an excited electron-hole pair (Figure 4.7). The Auger like process is very fast (on the order of picoseconds) compared to a radiative process (on the order of nanoseconds) in a NC. The fast nonradiative decay of multiexcitons in the $Zn_xCd_{1-x}Te$ colloidal nanoalloys occurs within 20-100 ps. The contribution of the fast processes increases with laser power and the corresponding lifetimes are given in Table 4.2. During the exciton-exciton interaction, two electron-hole pairs recombine by simultaneously promoting the other free electron or hole into second exciton state which has higher energy than the one-exciton state.

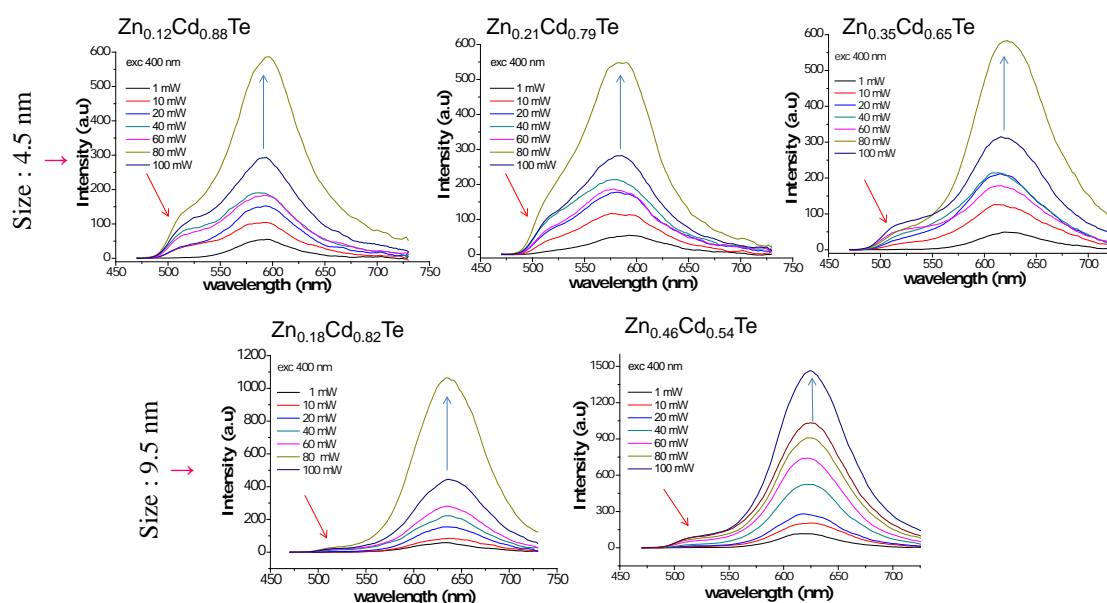


Figure 4.6. The emission intensity spectra of 4.5 ± 1.4 nm and 9.5 ± 2.4 nm-sized $Zn_xCd_{1-x}Te$ colloidal nanoalloys at initiation time obtained under different laser powers, correspondingly from low to high, of 1 to 100 mW. Blue arrows represent the one-exciton state in nanoalloys and shows extent of increase in PL intensity with laser power. Red arrows show the multiexciton states and the contribution of the state with laser power.

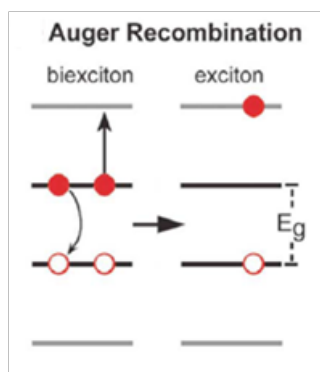


Figure 4.7. Schematic representation of Auger recombination in terms of energy bands. Two electrons and a hole (left) recombine to form a “hot” electron (right), with time constant τ_c .

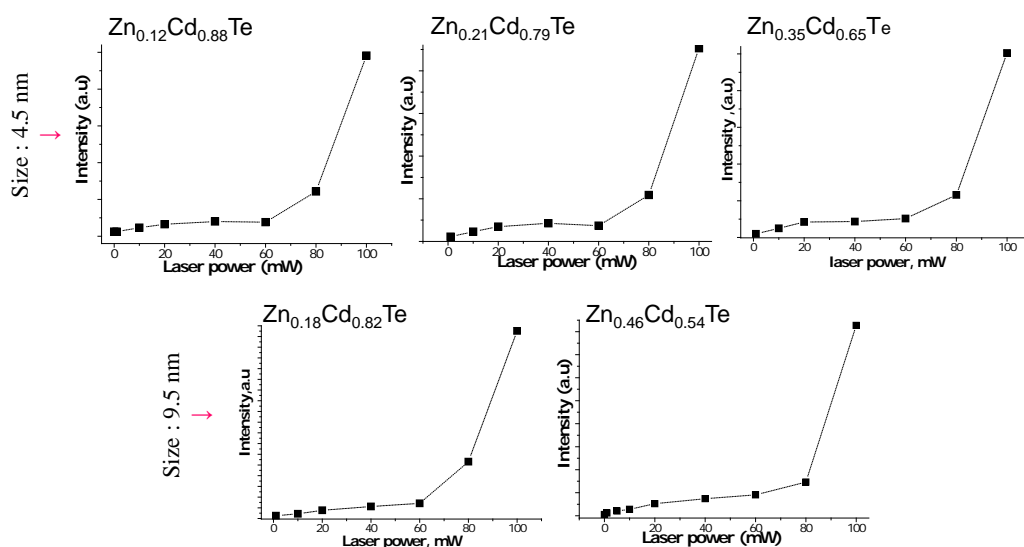


Figure 4.8. The dependence of emission intensity of 4.5 ± 1.4 nm and 9.5 ± 2.4 nm size $\text{Zn}_x\text{Cd}_{1-x}\text{Te}$ colloidal nanoalloys on the laser power.

Excitation under high laser power results in increase in PL intensity of the nanoalloys. As a whole, the increase in PL intensity with laser power is not linear but in certain intervals there are linear patterns (Figure 4.8). Up to a laser power of 20mW, the trend is linear. The slope of the rise is ($I_{\text{output}}/I_{\text{input}}$) about 0.53 for 4.5 ± 1.4 nm size $\text{Zn}_{0.12}\text{Cd}_{0.88}\text{Te}$. As the Zn fraction changes from 0.12 to 0.35 the slope increases from 0.53 to 0.67. Between 20-60 mW, excited states of the nanoalloys were saturated. The change in intensity with laser power ($I_{\text{output}}/I_{\text{input}}$) in this interval is less than that of the previous one for all the nanoalloys. The slope was decreased approximately from 0.50 to 0.35. The observed difference in optical response with the laser power indicated a change in the dominant relaxation channel as a result of the nonlinear interactions in the

system of photon-excited carriers. A significant increase in emission intensity of the nanoalloys was observed with further increase in laser power from 60 to 80 and 80 to 100 mW (Figure 4.8). For the 4.5 ± 1.4 nm size nanoalloys, the slope of the change ($I_{\text{output}}/I_{\text{input}}$) in intensity with the laser power from 60 to 80 and from 80 to 100 mW is 2.75 and is 3.76, respectively. For the 9.5 ± 2.4 nm-sized $\text{Zn}_{0.18}\text{Cd}_{0.82}\text{Te}$ colloidal nanoalloys the slope of the change ($I_{\text{output}}/I_{\text{input}}$) in intensity with the laser power from 1 to 20 is 0.45 and with the increase in the Zn fraction of the nanoalloys (from 0.18 to 0.46) the slope is about 0.53. Between 20-60 mW, excited states of the nanoalloys were saturated as in the small size nanoalloys. Further increase in the laser power from 60 to 80 mW and 80 to 100 mW, the slope is 2.94 and 3.48, respectively for $\text{Zn}_{0.18}\text{Cd}_{0.82}\text{Te}$ colloidal nanoalloys and the slope is 1.52 and 4.12, respectively for $\text{Zn}_{0.46}\text{Cd}_{0.54}\text{Te}$ colloidal nanoalloys.

The degree of exciton-exciton interaction via Auger recombination in the larger size nanoalloys is less than that in the smaller size nanoalloys because the bigger-sized particle has less surface trap states (Bryant and Jaskolski 2005). The energy and the extent of exciton-exciton interaction are determined by interior structure of nanoalloys, surface ligands, and the trap states. The $\text{Zn}_x\text{Cd}_{1-x}\text{Te}$ colloidal nanoalloys have same surface ligands-TGA, but their interior structure, degree of capping by TGA and type trap states are different. The differences determine the energies and the electron distributions not only on surface states but also of delocalized excitonic state formed upon photoexcitation. So the extent of the blue-shifted peak formation differs from nanoalloy to nanoalloy. The changes in the $I_{\text{output}}/I_{\text{input}}$ show differences.

Exciton localization and exciton-exciton interaction energy change with type of confinement regime (Schaller, Pietryga, and Klimov 2007). The blue-shifted peak formation showed that the $\text{Zn}_x\text{Cd}_{1-x}\text{Te}$ colloidal nanoalloys have type I confinement regime where the exciton is trapped within the core because the electron prefers to populate the lowest energy conduction band and the hole prefers the highest energy valance band available (Figure 4.9 and Figure 4.10). The confinement type reduces energy transfer between nanoparticles because the electron and hole are not near the surface. In Type II confinement regime nanoparticles have two materials with similar band gaps and the electron-hole is separated into the core and shell individually. Type II (Figure 4.9) confinement allow for a greater tuning of the band gap because both *the core diameter* and *the shell thickness* affect the electronic structure of the particle core/shell NCs with Type II may be a solution to the Auger recombination.

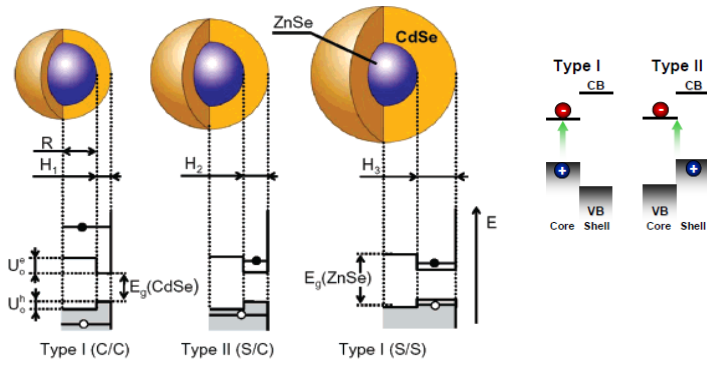


Figure 4.9. Different localization regimes supported by inverted ZnSe/CdSe hetero-NCs in the case of a fixed core radius and different shell widths (Source: Klimov I.V. 2006).

For both type II (S/C) and type I (S/S) localization regimes electron resides in the shell. Auger decay rates depend on overall extent of electronic wave function which is determined by total volume of hetero-NCs in the case of shell localized electron since the $Zn_xCd_{1-x}Te$ nanoalloys have no shell coating, Auger recombination is an active process in Type-I nanocrystals that produce exciton exciton repulsion (Klimov 2006 and Ivanov et al. 2004).

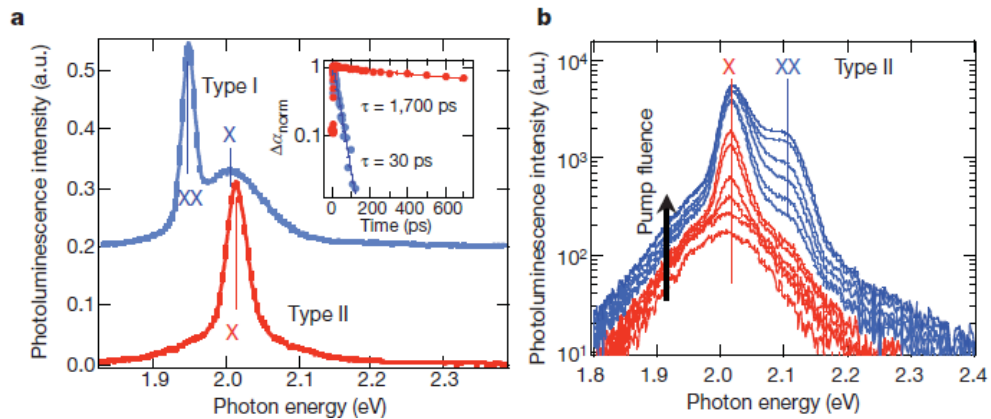


Figure 4.10. (a) ASE spectra of type-I CdSe NCs excited by 100-fs-pulses at 3 eV. Insert, transient-absorption dynamics measured for the NCs. (b) the pump-intensity-dependent photoluminescence spectra of the type-II sample show the development of a narrow ASE peak near the centre of the single-exciton emission band. The second ASE band, which develops at higher fluences, is located near the XX photoluminescence feature (Source: Klimov et al. 2007).

Exciton-exciton interaction results in profound change in the photophysical properties of the nanoalloys. In the emission intensity/wavelength spectra of the nanoalloys PL peak shape and the position changes with the laser power. The change in shape of the peaks and the substantial enlargement in the bandwidth FWHM prove that the nanoalloys have type I confinement regime. The change in PL peak positions is the another indicator of exciton-exciton interactions. PL peak maximum shifts to shorter and longer wavelength under laser power. As the laser power increases the PL maximum peaks starts shifting to both blue and red region. There is not a regular change with laser power. Figure 4.11 shows the laser power dependence of PL peak maxima.

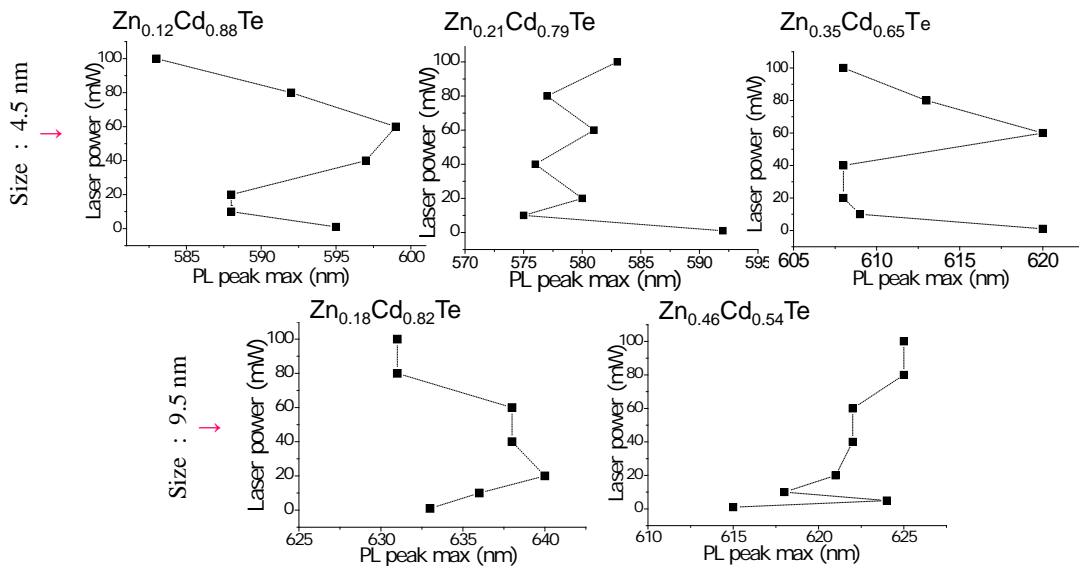


Figure 4.11. The change in the photoluminescence peak position of 4.5 ± 1.4 nm and 9.5 ± 2.4 nm sized $Zn_xCd_{1-x}Te$ colloidal nanoalloys with the laser power correspondingly from low to high, of 1 to 100 mW at initiation time ($t=0$ ps).

Exciton-exciton interactions can be repulsive or attractive. The interaction type depends on the laser power. For all 4.5 ± 2.4 nm size $Zn_xCd_{1-x}Te$ nanoalloys (4.5 nm), laser power tunes the peak positions first to blue region (high energy/low wavelength) than red region. It shows that the exciton-exciton interactions are first repulsive and further increase in the laser power results in red shifting. On the other hand, for the 9.5 ± 2.4 nm size $Zn_{0.18}Cd_{0.82}Te$ nanoalloys the shift in PL peak position is toward to red region, upon excitation up to 20 mW. The red-shifting indicates the attractive type interaction energy between excitons. With the increase of laser power from 20 to 100

mW the exciton-exciton interaction in the 9.5 ± 2.4 nm size $\text{Zn}_{0.18}\text{Cd}_{0.82}\text{Te}$ nanoalloys becomes repulsive therefore the PL peak shows blue-shifting. For the 9.5 ± 2.4 nm size $\text{Zn}_{0.46}\text{Cd}_{0.54}\text{Te}$ nanoalloys the PL peak position shifts first to red region, upon excitation up to 10 mW and the increase in laser power from 10 to 100 mW results in blue-shifting of PL peak maxima due to the repulsive type exciton-exciton interaction. All the nanoalloys have different interior structure and the exciton dynamics is governed by effective mass of electron and holes at occupied states (Schaller et al. 2007). In the 9.5 ± 2.4 nm-sized nanoalloys, the exciton is free to wander throughout the crystal compared to exciton in smaller nanoalloys. The more attractive type of the exciton-exciton interaction in the 9.5 ± 2.4 nm-sized nanoalloys can be explained by the relative free motion of the excitons in big nanoalloys compared to their motions in 4.5 ± 1.4 nm sized nanoalloys.

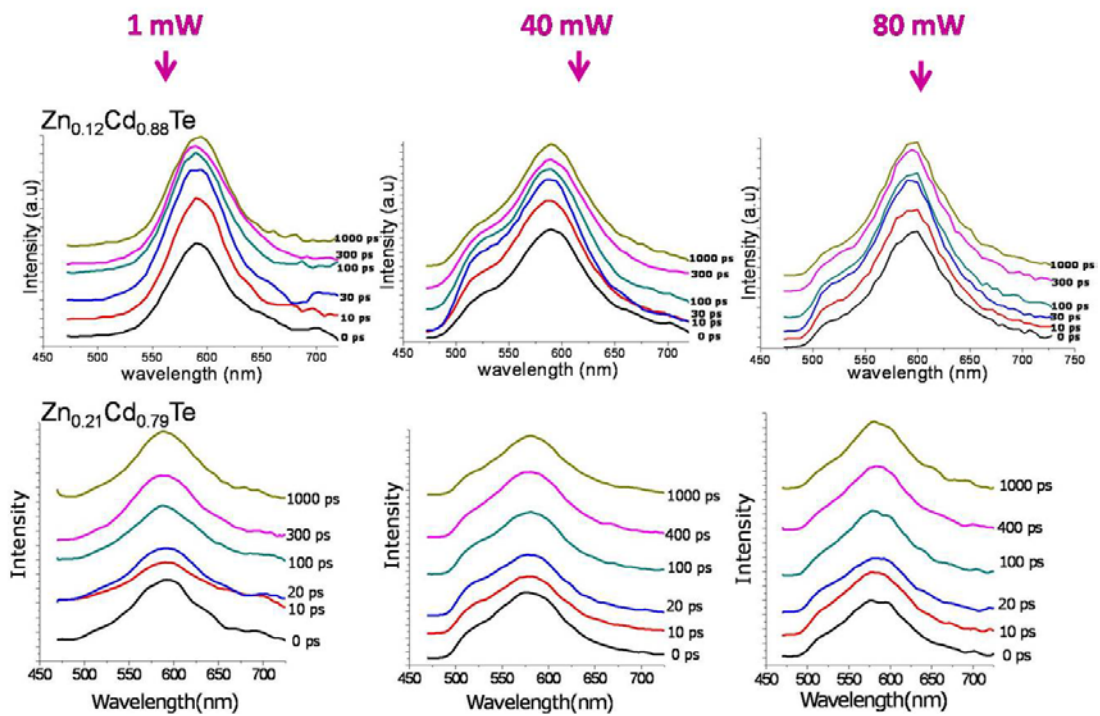


Figure 4.12. The time-resolved emission spectra of $\text{Zn}_{0.12}\text{Cd}_{0.88}\text{Te}$ and $\text{Zn}_{0.21}\text{Cd}_{0.79}\text{Te}$ colloidal nanoalloys obtained from ps-resolved Streak camera images. Size of nanoalloys is 4.5 ± 1.4 nm.

The streak camera images of the $\text{Zn}_x\text{Cd}_{1-x}\text{Te}$ colloidal nanoalloys have been analyzed at specific time intervals. The time-resolved emission spectra of nanoalloys at specific wavelengths were extracted by moving the cursor in the time scale in the rightmost column in the streak camera images of the colloidal nanoalloys (Figure 4.12

and Figure 4.13). In the time-resolved emission spectra how exciton dynamics changes with time and how changes are reflected in the emission spectra are seen.

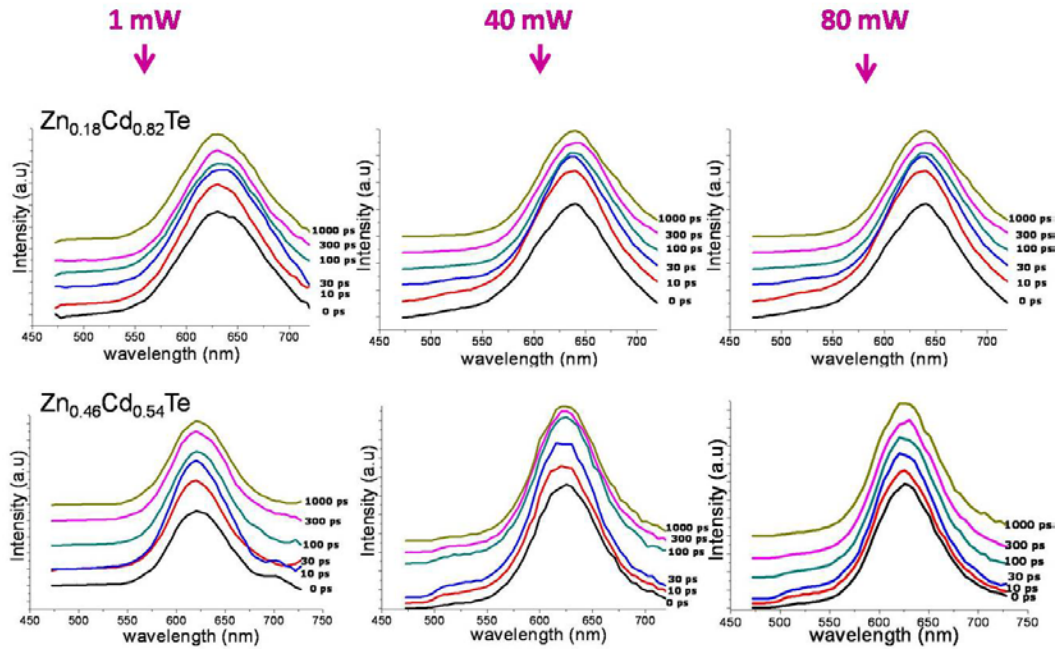


Figure 4.13. The time-resolved emission spectra of $\text{Zn}_{0.18}\text{Cd}_{0.82}\text{Te}$ and $\text{Zn}_{0.46}\text{Cd}_{0.54}\text{Te}$ nanoalloys obtained from ps-resolved Streak camera images. Size of nanoalloys is 9.5 ± 2.4 nm.

Figure 4.12 shows the time-resolved emission spectra of the nanoalloys of 4.5 ± 1.4 nm size ($\text{Zn}_{0.12}\text{Cd}_{0.88}\text{Te}$ and $\text{Zn}_{0.21}\text{Cd}_{0.79}\text{Te}$). Under the excitation of 1 mW laser power, shape of the PL peaks, the peak position and the bandwidth does not change significantly within 1000 ps. As laser power increases to 40 mW, a new band in the blue region starts to appear. The lifetime of the blue-shifted PL peak is higher than 1000 ps. The exciton-exciton interaction takes long time. Under the excitation of 80 mW laser power, the blue-shifted band still presents in time-resolved spectra. The intensity of blue-shifted peak decreases with time. Up to 30 ps the intensity of the new band enhances but its intensity decreases with time. There is substantial enlargement in the bandwidth FWHM of the nanoalloys and within 1000 ps the PL peak positions show red-shift. The shifting to the red region indicates the decrease in the repulsive exciton-exciton interaction.

The time-resolved emission spectra of the nanoalloys of 9.5 ± 2.4 nm size ($\text{Zn}_{0.18}\text{Cd}_{0.82}\text{Te}$ and $\text{Zn}_{0.46}\text{Cd}_{0.54}\text{Te}$) are shown in Figure 4.13. The excitation of the nanoalloys with 1mW laser power does not affect the dynamics of exciton significantly.

Only one exciton state is present under the excitation. The state has long lifetime. As the laser power increases to 40 mW, a new weak band in the blue region appears in a time less than 100 ps. The two-exciton state has a short life time. Under excitation of 80 mW laser power, the blue-shifted band still presents in the time-resolved spectra but it disappears within 100 ps. The intensity of blue-shifted peak decreases. Up to 30 ps the intensity of the new band enhances but within 100 ps its contribution decreases. There is substantial enlargement in the bandwidth FWHM of the nanoalloys and within 1000 ps the PL peak positions show red-shifting.

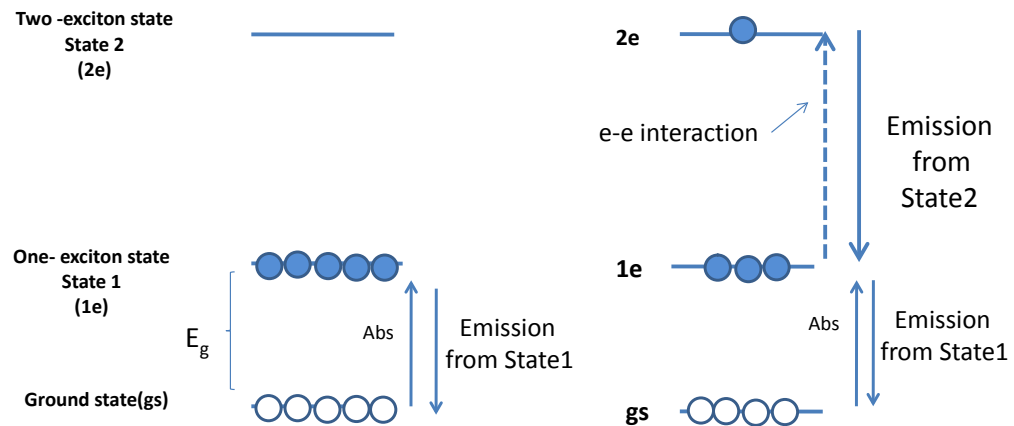


Figure 4.14. Schematic representation of one-exciton state and two-exciton state in the the colloidal $Zn_xCd_{1-x}Te$ nanoalloys

The formation of the blue-shifted peak in the PL spectra is due to population of two-exciton state as a result of the exciton-exciton interaction in the one-exciton state. Figure 4.14 represents the population scheme of two-exciton state via exciton-exciton interaction in one-exciton state. As the laser power increases from 1 mW to 40 mW, two-excitonic state (state 2) was populated by the interaction of excitons. The change in intensity of the blue-shifted emission peak (state 2) with laser power is different from the change in that of one exciton emission intensity (state 1). Throughout 1000 ps, the two-excitonic state is still populated in the 4.5 ± 1.4 nm-sized nanoalloys under the excitation of 40 mW laser power. Less than 80 mW laser power the state 2 starts to repopulate the state 1. Each state has different lifetime and the lifetime values determine whether the nanoalloys can be applicable as a lasing material. The contribution of blue-shifted PL emission under the excitation with laser power of 80 mW is small compared to the one that is excited by 40 mW. In the 9.5 ± 2.4 nm-sized nanoalloys ($Zn_{0.18}Cd_{0.46}Te$

and $\text{Zn}_{0.46}\text{Cd}_{0.54}\text{Te}$) the population of state 2 is very limited and the lifetime of the state is less than 100 ps. The nanoalloys have less exciton-exciton interactions compared to the smaller size nanoalloys.

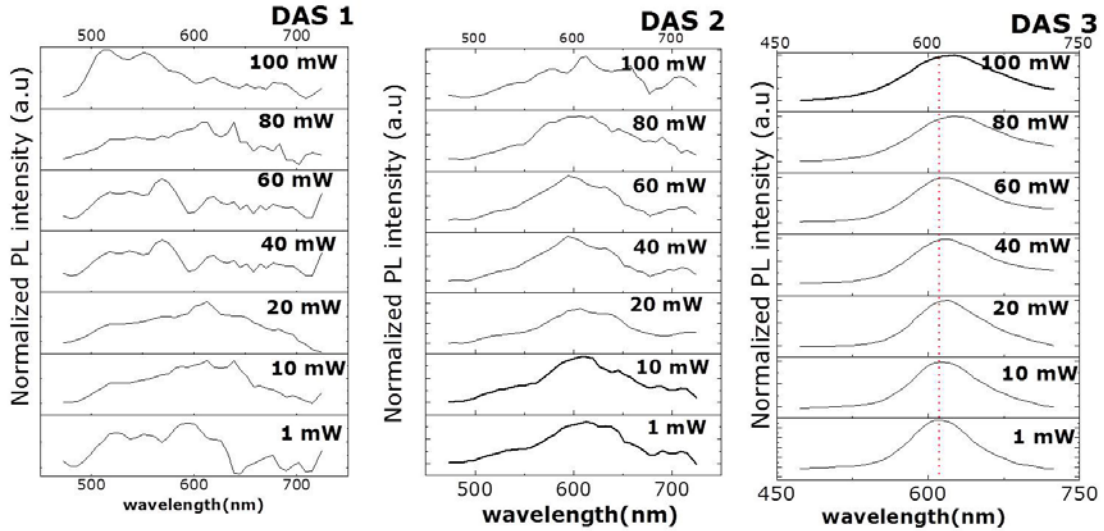


Figure 4.15. Decay associated spectra of $\text{Zn}_{0.13}\text{Cd}_{0.87}\text{Te}$ colloidal nanoalloys obtained by global analysis of their streak camera images. The size of particles is 4.5 ± 1.4 nm. The laser power was changed from 1 mW to 100 mW.

From streak camera images position-resolved decays of the nanoalloys from shorter to longer time windows was obtained. The decay curves will be fitted with a proper exponential equation to find the decay components. The technique for fitting a large collection of data to a set of parameters is known as global analysis. Global analysis is another way to get decay components and spectral position of the processes associated with the decays. The nanoalloys show multiexponential decays. All streak images were analyzed globally with Glotran software to fit the multi decay process. In this analysis; lifetimes remain constant as a function of emission wavelength. The total spectral intensity at a given wavelength is known from the steady state measurements and the relative percentage of that intensity belongs to each decay component from the lifetime measurements. Plotting each component as a fraction of the total intensity gives the emission spectrum of that microstate. This is a decay-associated spectrum (DAS) that represents the emission of a state with a particular decay lifetime (van Stokkum et al. 2008).

The DAS of $\text{Zn}_{0.13}\text{Cd}_{0.87}\text{Te}$ colloidal nanoalloys is shown in Figure 4.15 and represents the emission of state with three decay lifetime. Combination of three DAS

gives PL emission spectra at λ_{\max} . The figure shows that the bandwidth and bandshape of the spectrum of nanolalloy is changing. The corresponding decay-associated spectra (DAS), their contribution, and their spectral position are all different under excitation of different laser power. DAS1 represents the exciton-exciton interaction in which the PL emission is more blue-shifted. It has shortest lifetime and the emission disappears within less time (30 ps) DAS2 belongs to both exciton-exciton interaction and Auger-like nonradiative processes. The radiative emission is dominated by the longest lifetime component (DAS3) followed by DAS2 and DAS1. The individual emission maximum of DAS 3 does not coincide with the radiative emission maximum (at λ_{\max} : 583 nm) even at 1mW laser power.

The decay-associated spectra of the $Zn_xCd_{1-x}Te$ colloidal nanoalloys represent size and composition-dependent interaction type. Figure 4.16 and Figure 4.17 indicate the DAS of 4.5 nm ($Zn_{0.12}Cd_{0.88}Te$ and $Zn_{0.35}Cd_{0.65}Te$) and 9.5 ± 2.4 nm-sized nanoalloys ($Zn_{0.18}Cd_{0.82}Te$ and $Zn_{0.46}Cd_{0.54}Te$), respectively. All colloidal nanoalloys showed multiexponential decays (3 distinct decay processes). Each color in the DAS spectra denotes different processes; fastest process (DAS1: black line) which is in blue region, fast process (DAS2: red line), and long process (DAS3: blue line). Each individual exponential represents multi-state and multi processes. Contribution of each DAS to total emission changes with the power of laser.

In $Zn_{0.12}Cd_{0.88}Te$ under 1 mW laser power, DAS3 has the highest contribution among the three processes. DAS2 and DAS1 are in blue-shifted region compared to DAS3. Under excitation with 1mW power of laser, more excitons were created but their interaction reflected in the DAS1 and DAS2. As laser power increases to 40 mW, the amplitude of the DAS2 and DAS1 gets higher. PL peak shape and their position show changes due to exciton-exciton interaction. The spectral position of the DAS1 and DAS2 show shifting to blue region compared to DAS3 under the laser power. DAS3 is very broad and contribution of the blue-shifted emission to the DAS3 was weak with respect to DAS1 and DAS2. Further increase in laser power results in increase in amplitude of DAS3 and change in both amplitude and position of DAS2 and DAS3.

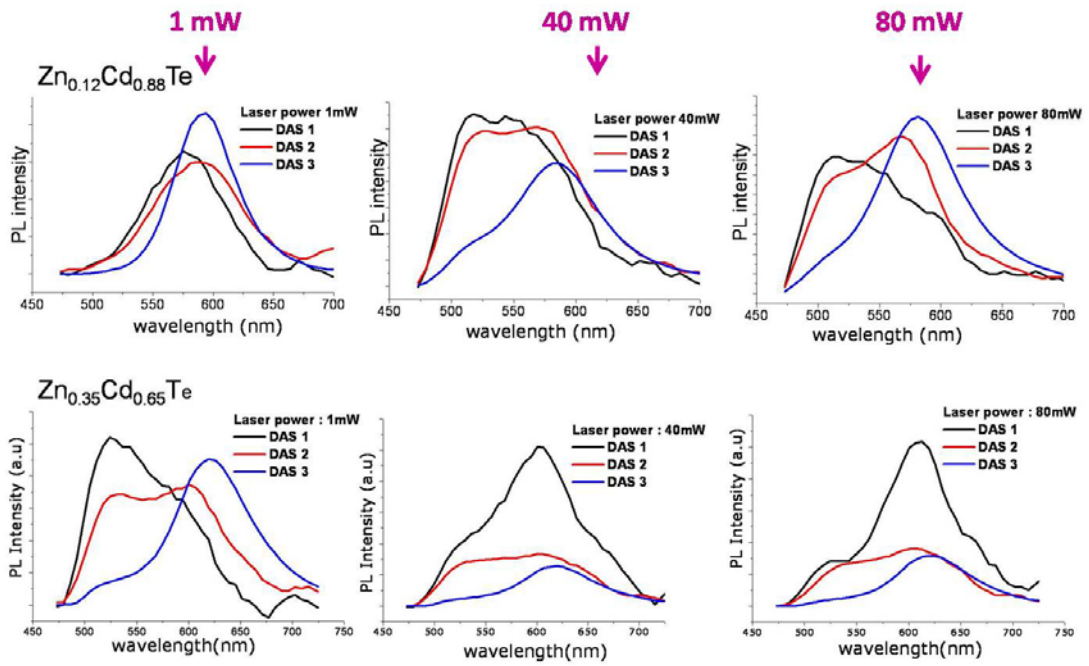


Figure 4.16. Decay associated spectra of $\text{Zn}_{0.12}\text{Cd}_{0.88}\text{Te}$ and $\text{Zn}_{0.35}\text{Cd}_{0.65}\text{Te}$ colloidal nanoalloys obtained by global analysis of their streak camera images. The size of particles is 4.5 ± 1.4 nm. The laser power changed from 1 mW to 100 mW.

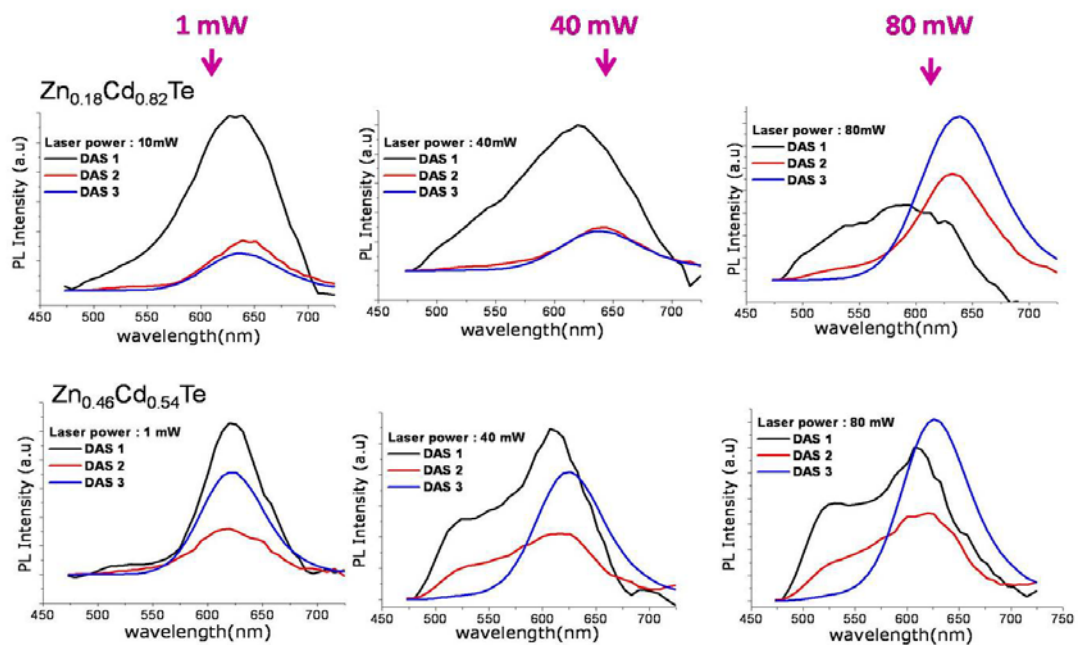


Figure 4.17. Decay associated spectra of $\text{Zn}_{0.18}\text{Cd}_{0.82}\text{Te}$ and $\text{Zn}_{0.46}\text{Cd}_{0.54}\text{Te}$ colloidal nanoalloys obtained by global analysis of their streak camera images. The size of particles is 9.5 ± 2.4 nm.

Each DAS contributes to the other to a different extent. The contribution of DAS3 is high at 80mW laser power. In the $Zn_{0.35}Cd_{0.65}Te$ nanoalloys even at 1 mW laser power excitation, DAS1 and DAS3 are more blue-shifted. Less than 1 mW laser power, exciton-exciton interaction starts. DAS1 has the highest contribution. Both DAS1 and DAS3 contribute to DAS3 and the contribution of DAS1 increases at 40 mW laser power. In the $Zn_{0.35}Cd_{0.65}Te$ nanoalloys with high fraction of Zn, the contribution of fast processes (DAS1 and DAS2) to PL emission is high (Figure 4.16).

In 9.5 ± 2.4 nm sized $Zn_{0.18}Cd_{0.82}Te$ and $Zn_{0.46}Cd_{0.54}Te$ colloidal nanoalloys, excitation under 1mW laser power increases the contribution of DAS1 (Figure 4.17). At 40 mW, DAS1 becomes highly dominant in the $Zn_{0.18}Cd_{0.82}Te$ nanoalloys. Three decays contribute to each other. DAS1 is more red-shifted compared to DAS2 and DAS3. At the highest laser power (100 mW), DAS3 highly contributes to the decay and DAS1 is more blue-shifted in the $Zn_{0.18}Cd_{0.82}Te$ nanoalloys. In the $Zn_{0.46}Cd_{0.54}Te$ colloidal nanoalloys DAS1 and DAS2 have blue-shifted shoulder due to exciton-exciton interaction. Generally the excitation intensity increases the weight of the fast component with respect to slow one because more than one exciton was created and increase in laser power initiates the exciton exciton interactions. High power intensities result in the population of the two-exciton states and non-linear processes come into play. The non-linear processes reflect on the DAS.

Lifetimes, decay constant and their amplitudes are calculated for each DAS. Decay times and their amplitudes are given in Table 4.2. In consequence of change in composition and size, the lifetime values and rate constants (time-resolved spectra and decay times) are different.

Fast decay time constants decrease with increasing power for the 4.5 ± 1.4 nm $Zn_{0.12}Cd_{0.88}Te$ and $Zn_{0.35}Cd_{0.65}Te$ nanoalloys. In the 9.5 ± 2.4 nm sized $Zn_{0.18}Cd_{0.82}Te$ and $Zn_{0.46}Cd_{0.54}Te$ colloidal nanoalloys the decay time constants decrease with the increasing power of laser. The 9.5 ± 2.4 nm-sized $Zn_{0.46}Cd_{0.54}Te$ nanoalloys have the highest fraction of Zn in their structure. The increase in size reduces the surface to volume ratio and decreases number of possible defect states which act as recombination center so lifetime gets longer. Average decay lifetimes of the $Zn_{0.46}Cd_{0.54}Te$ nanoalloys are longer than those of other nanoalloys. Slower decays were attributed to trapping and recombination of trapped carriers in the nanoalloy structure. Since the nanoalloys incorporate higher percent of Zn, excitons diffuse between Cd and Zn and it prolongs the lifetime. Average lifetime values of each nanoalloy prolongs with laser power

except $\text{Zn}_{0.21}\text{Cd}_{0.79}\text{Te}$. τ_{av} of $\text{Zn}_{0.21}\text{Cd}_{0.79}\text{Te}$ decreases by 13% because of interior trap states like defects in the crystal structure (Yagi et al. 2006; Liu et al. 2011). In the $\text{Zn}_{0.21}\text{Cd}_{0.79}\text{Te}$ nanoalloys, exciton-exciton annihilation could take place when there is a high exciton density within a small volume of sample. The power-dependent decay was assigned primarily to exciton-exciton annihilation. This mechanism becomes dominant under high excitation power where the multiple excitons are created in the nanoalloys. The annihilation leads to trap state saturation and it accumulates the band edge exciton.

Table 4.2. Decay rate constants, corresponding lifetime with their respective amplitude of the nanoalloys.

Nanoalloy	Laser Power (mW)	k1 (10^{-3})	k2 (10^{-3})	k3 (10^{-5})	τ_1 (ns)	τ_2 (ns)	τ_3 (ns)	A1 (%)	A2 (%)	A3 (%)	τ_{av} (ns)
$\text{Zn}_{0.12}\text{Cd}_{0.88}\text{Te}$	1	39.5	2.2	33.3	0.03	0.45	30	50	20	30	30
	10	16.4	1.8	2.5	0.06	0.55	40	32	35	32	39
	40	10.0	1.5	2.4	0.10	0.65	42	40	34	26	41
	100	17.9	2.0	2.4	0.06	0.50	42	43	31	26	41
$\text{Zn}_{0.21}\text{Cd}_{0.79}\text{Te}$	1	15.1	1.5	2.4	0.07	0.66	41	27	32	41	41
	10	14.2	1.6	2.5	0.07	0.61	40	40	30	30	39
	40	15.9	2.2	2.7	0.06	0.45	37	35	32	32	36
	100	12.1	1.8	2.6	0.08	0.57	38	41	35	25	37
$\text{Zn}_{0.35}\text{Cd}_{0.65}\text{Te}$	1	28.3	2.3	3.2	0.04	0.43	32	38	27	35	31
	10	27.9	2.1	2.4	0.04	0.48	42	57	23	20	41
	40	34.4	2.1	2.5	0.03	0.47	40	65	18	16	39
	100	12.9	1.7	2.0	0.08	0.59	50	36	29	36	50
$\text{Zn}_{0.18}\text{Cd}_{0.82}\text{Te}$	1	19.3	2.0	3.2	0.05	0.51	31	39	24	37	30
	10	22.3	1.6	2.7	0.04	0.61	37	66	16	18	36
	40	32.0	3.1	2.5	0.03	0.32	40	47	26	26	39
	100	46.7	2.5	2.0	0.02	0.41	50	50	18	32	50
$\text{Zn}_{0.46}\text{Cd}_{0.54}\text{Te}$	1	14.3	1.3	3.0	0.07	0.77	34	53	18	30	33
	10	27.1	2.5	2.4	0.04	0.40	42	48	22	30	42
	40	24.5	2.1	1.9	0.04	0.47	52	54	14	32	52
	100	25.2	2.1	1.6	0.04	0.47	62	44	21	35	62

Under 1-100 mW laser power, 100 μm spot size and 400 nm excitation wavelength the photon fluence j_p changed from 10^{15} to 10^{17} photon/ cm^2 s per laser pulse. Average number of excitons in each analyzed nanoalloys is higher than 1. To create more than one exciton within each crystal more than 10^{15} photon/ cm^2 per laser pulse

was used (Saba et al. 2009; Klimov 2007). In time-resolved spectroscopy it is possible to make a comment on nanosecond or longer time scale processes. To have more insight on the early time scale processes such as surface state processes, bleaching process, interior trap state processes we should analyze the NCs with of femtosecond-resolution spectroscope (Rawalekar et al. 2010).

In the Table 4.2 it is seen that the lifetime values of corresponding DAS ($\tau_{(DAS)}$) change with laser power. The DAS of the nanoalloys excited at each laser power has been fitted with the time constants with their respective amplitudes as $\tau_{1(DAS1)}$, $\tau_{2(DAS2)}$ and $\tau_{3(DAS3)}$. As the laser power increases to 100 mW, the corresponding lifetime values and their amplitudes change. The lifetime values of fast processes; $\tau_{1(DAS1)}$, increase from 30 to 60 ps and 40 to 80 ps with laser power in the $Zn_{0.12}Cd_{0.88}Te$ and $Zn_{0.35}Cd_{0.65}Te$ nanoalloys, respectively. Fraction of Zn in the nanoalloys also changes the lifetime values. On the other hand, in the 9.5 ± 2.4 nm-sized $Zn_{0.18}Cd_{0.82}Te$ and $Zn_{0.46}Cd_{0.54}Te$ colloidal nanoalloys, the lifetime values of fast processes; $\tau_{1(DAS1)}$, decreases from 50 to 20 ps and 70 to 40 ps with laser power. The size of the nanoalloys changes the lifetime values. The average lifetimes of the nanoalloys increase with an increase in the size. The increase in size reduces the surface to volume ratio, thus decreases number of possible defect states which act as recombination center.

4.5. Conclusion

Colloidally synthesized $Zn_xCd_{1-x}Te$ nanoalloys have been analyzed in terms of their exciton relaxation dynamics and exciton-exciton interactions by time-resolved fluorescence spectroscopy using streak camera system. The nanoalloys were excited at 400 nm and laser powers have been changed from 1 to 100 mW. With laser powers, 100 μm spot size and 400 nm excitation wavelength, the photon fluence are changed from $j_p = 3.2 \times 10^{15}$ to 3.2×10^{17} photon/cm²s per laser pulse, respectively. Under the high power laser excitation multistates formed, multi-transition and multi-processes took place. The decay signals of the nanoalloys showed multiexponential behavior. The amplitude and lifetime values of the fast and slow processes have been obtained by the global analysis method. Time-resolved photoluminescence decays showed exciton lifetimes in tens of picoseconds scale for fast processes and in tens of nanosecond scale for slow ones.

The detected PL signal and obtained decay-associated spectra (DAS) were affected by the power of laser, size and composition of the nanoalloys. The changes in the PL peak position, the bandwidth, and the peak shape indicated that multiexciton was generated in the $Zn_xCd_{1-x}Te$ nanoalloys under excitation with high laser power. Fluorescence intensity of the nanoalloys increased with the laser power. The increase in the PL intensity was highly dominant when laser power was increased from 80 mW to 100 mW. At 100 mW the output intensity was high. The nanoalloys of smaller sizes (4.5 ± 1.4 nm) have more excitons, so there are more exciton-exciton interactions. However the bigger-sized (9.5 ± 2.4 nm) nanoalloys have less exciton, so there are less exciton-exciton interactions. The one-exciton-lifetime of the bigger nanoalloys is longer than those of the smaller ones.

As the laser power increases, the exciton-exciton interaction starts and new exciton energy state forms in $Zn_xCd_{1-x}Te$ nanoalloys. Their DAS showed that the fraction of incorporated Zn diversifies the electronic structure of the nanoalloys and creates new decay pathways. Exciton dynamics are both composition- and size-dependent. In small nanoalloys exciton-exciton interaction is repulsive and highly intense compared to the larger nanoalloys. Exciton-exciton interactions in the Zn-rich nanoalloys as reflected in their DAS are more dominant than the Zn-poor nanoalloys. The change in the shape of the PL peaks and the FWHM proves that $Zn_xCd_{1-x}Te$ nanoalloys have type I confinement regime. The positions of the PL maxima of the nanoalloys showed blue-shifting with the laser power due to stronger exciton-exciton interactions. For the small size nanoalloys, the laser power continuously tuned peak positions to the lower wavelength and this showed that the exciton-exciton interactions were repulsive. As the size of nanoalloys becomes larger, the tuning to the blue-region was lowered because the excitons diffuse more freely throughout larger crystals and it reduces the exciton-exciton interactions.

The relaxation dynamics showed a fast decay ($\tau_1 < 50$ ps), which is dependent on excitation intensity, a slow decay ($\tau_2 \sim 400-700$ ps), and band edge transition ($\tau_3 \sim$ tens of ns). The slow decay was attributed to the electron-hole recombination. The intensity-dependent, fast-decay component was assigned to exciton-exciton annihilation or photoionization/Auger recombination. Experimentally it is not easy to distinguish them.

CHAPTER 5

EXCITON DYNAMICS OF CdTe AND CdTe/CdS COLLOIDAL NANACRYSTALS

5.1. Introduction

Time-resolved studies play a prominent role in understanding of the optical properties of the nanocrystals. The time range of the non-radiative relaxation processes of excitons and the energy transfer processes vary between femtoseconds and picoseconds, respectively. The lifetime of the radiative recombination of the excitons is in the nanosecond scale. Exciton dynamics provide unique information both on the nature of optical transitions and on the local environment of an optically active species (Klimov V. 2000).

The decay kinetics of the photoluminescence provides information on the nature of excited states, the quality of NCs, the competition between the radiative and non-radiative recombination processes, and the interactions between nanocrystals. Both the radiative and non-radiative decay processes influence the decay kinetics of excitons in NCs. An important non-radiative relaxation process is trapping of an exciton at a defect or an impurity zone in the NC or on the surface of it. Photoexcitation creates highly excited excitons in the NCs that may follow several competing relaxation pathways to reach the lowest excited state. The relaxation of high-energy exciton to the band edges takes place by the interaction with phonons. The time of the phonon relaxation processes is much faster (varies from 100 fs to 10 ps) than the time for the radiative and non-radiative recombination processes (Fischer et al. 2005 and Klimov V. 2000).

Ghislotti *et al.* analyzed photoluminescence spectra of CdTe nanocrystals and the study revealed the excitonic character of the radiative emission, as well as providing evidence for the important role played by nonradiative combination (Ghislotti et al. 1999). PL of the NCs showed bi-exponential decays with time constants in the order of 30-60 and 200-300 ps, respectively. The short decay assigned as surface recombination and defect-assisted recombination. On the other hand the longer time decay was ascribed to bound exciton recombination.

Kobayashi and his coworkers studied on carrier multiplication in tetradecylphosphonic acid (TDPA) CdTe quantum dots by picosecond single-photon timing spectroscopy (Kobayashi et al. 2009). They reported that the carrier multiplication occurs only by sending a photon having an energy of at least $2.5 E_g$ of CdTe and they reported that the value was close to that of CdSe QDs.

Exciton formation and exciton multiplication thresholds in the quantum dots shows band gap dependent properties. Threshold energy for single and multi-exciton formation can be found by changing the laser power, and excitation wavelength of laser. Efficient multi-exciton generation upon excitation with the photons is competed by hot carrier relaxation. Since nanoparticles having high dielectric constant they have long radiative lifetime (on the orders of tens of ns), it will be possible to create more than one exciton by applying proper laser power and pump intensity (Klimov V. 2000).

5.2. Time-Resolved Measurements of CdTe Core and CdTe/CdS Core/Shell Nanocrystals

Time-resolved fluorescence measurements CdTe and CdTe/CdS nanocrystals have been carried out by the Streak camera system. The set-up of the system is shown in Figure 4.1 and described in section 4.2 in detail.

During the analysis 100 μ l colloidal solutions of the NCs were diluted with proper amount of ultra-pure distilled water and they were put in the quartz cuvette. The cuvette was placed into the sample holder. The measurements were performed without stirring. Spot size of the laser beam was 100 μ m. The spectral interval varied from 470 nm to 730 nm. The sweep-range of the streak camera was 2 ns. Streak camera images of the NCs were measured upon excitation with 400-nm laser light. Laser power changed from 1 mW to 100 mW during measurement. The streak camera images have been corrected for the instrumental curvature. Then the images have been globally analyzed.

The NCs have been excited above their band gap with the photons having an energy of 3.1 eV (400nm) by changing photon fluence from $j_p=10^{15}$ to 10^{17} photon/cm² using ND filters. Energy density and photon density play a role to determine the number of formed excitons upon exciations in the NCs. As the number of photon fluence (laser power) increased, the PL intensity of each NC increased.

Photophysical parameters of analyzed CdTe core and CdTe/CdS core shell nanocrystals are listed in Table 5.1. Transmission electronic microscopy shows that thiol-capped NCs are spherical. Steady state absorption spectrum shows that they are in strongly quantum-confined regime and they have size-dependent band gap energy. The size values were obtained by DLS measurements. The synthesis and characterization of the NCs have been explained in Chapter 3. Stock solutions of the NCs have been analyzed. Dilution factor was determined as 1/100 as in the analysis of $Zn_xCd_{1-x}Te$ colloidal nanoalloys. During the measurement of CdTe core and CdTe/CdS core/shell NCs with the laser power of 100 mW, cut of filter of 12.5% was used to prevent the oversaturation of detector.

Table 5.1. Photophysical parameters of analyzed CdTe core and CdTe/CdS core/shell nanocrystals and their size

Nanoparticles	λ_{abs} (nm)	λ_{PL} (nm)	QY (%)	Size (by DLS) (nm)
CdTe	511	535	13	2.2
CdTe	529	554	17	4.1
CdTe	551	585	25	5.1
CdTe/CdS	507	536	17	2.3
CdTe/CdS	528	557	26	4.1
CdTe/CdS	539	566	37	4.6
CdTe/CdS	543	575	34	5.3

Figure 5.1 and Figure 5.2 show the streak camera images of CdTe ($\lambda_{PL}=554$ nm) and CdTe/CdS ($\lambda_{PL}=557$ nm) NCs excited under different laser power, respectively. Each NC has the highest emission intensity at $t=0$ ps (rising time) and the PL intensity decreases exponentially. Streak camera images of the all NCs, listed in Table 5.1, do not differ much from each other. PL intensity of the NCs at each laser power is represented by colors from red (high) to blue (low). Laser power intensity dependence of PL signals for CdTe and CdTe/CdS NCs behaves similarly. PL intensity was found to be power dependent. As the laser power increases from 1 mW to 100 mW the line width (FWHM) widens in all NCs.

CdTe PL λ_{max} 554 nm, size 4.1 nm

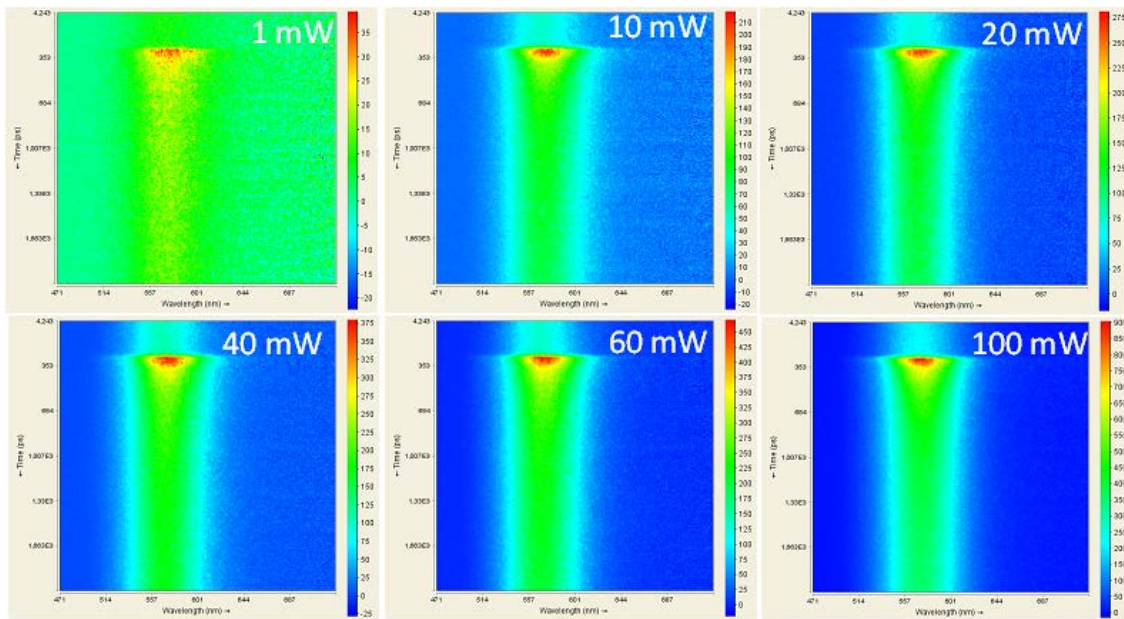


Figure 5.1. Streak camera images of CdTe (PL λ_{max} : 554 nm) nanocrystals excited with different laser powers: 1 mW to 100 mW, from upper left to lower right respectively. Fluorescence intensity of nanocrystals is represented by colors from red (high) to blue (low). Size of the nanocrystals is 4.1 nm.

CdTe/CdS PL λ_{max} 557 nm, size 4.1 nm

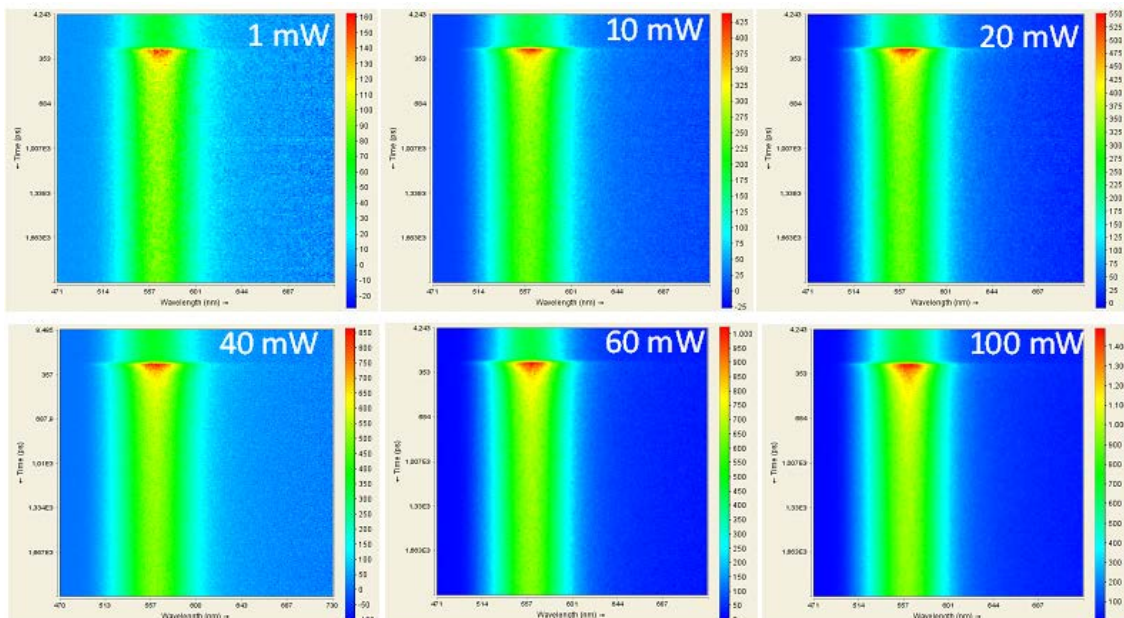


Figure 5.2. Streak camera images of CdTe/CdS (PL λ_{max} : 557 nm) nanocrystals excited with different laser powers: 1 mW to 100 mW, from upper left to lower right, respectively. Fluorescence intensity of nanocrystals is represented by colors from red (high) to blue (low).

Figure 5.3 represents change in the PL intensity of the NCs with respect to the laser power. In case of CdTe NCs, the increase in the PL intensity with the laser power is not linear as a whole (Figure 5.3a). Up to 10 mW laser power, the change in the amplitude of the PL intensity is linear. Threshold energy for the deviation from linearity is 10 mW for the all CdTe NCs. Between 20-60 mW, the emission intensity of 2.2 nm and 4.1 nm sized CdTe NCs is saturated. This excitation intensity dependence was explained by nonlinear exciton-exciton annihilation or Auger photoionization. The variation of output intensity (I_{out}) relative to input intensity (I_{in}) is less than one with excitation between 20-60 mW laser powers. The PL intensity of 5.1 nm CdTe NCs is still increasing under excitation 10 mW laser power but the increase is not as much as the increase in the smaller size CdTe NCs. The I_{out}/I_{in} of 5.1 nm-sized CdTe NCs have a negative deviation after 60 mW laser power while I_{out}/I_{in} of 2.2 and 4.1 nm-sized CdTe have positive deviation (Figure 5.3a). For larger size CdTe NCs the trap states become saturated under high fluency of photons, exciton-exciton annihilation starts. In smaller size CdTe NCs exciton-exciton interaction was more dominant compared to the larger size CdTe NCs. Because diffusion of excitons are restricted in the smaller CdTe NCs. Exciton confinement in the 2.1 nm and 4.1 nm-sized CdTe NCs is very strong. That is why the small size nanocrystals are exposed to exciton-exciton interaction.

The PL intensity of CdTe/CdS NCs increases with laser power. The extent of the increase varies from NC to NC. The change in the emission intensity of CdTe/CdS NCs with laser power is depicted in Figure 5.3b. As a whole the PL intensity of the NCs increase with the power of laser. Between 20-40 mW, the emission intensity of 2.3 nm, 4.1 nm, and 5.3 nm sized CdTe/CdS NCs become saturated. Further increase in laser power results in increase in the PL intensity. As the size of the CdTe/CdS NCs increases, the PL intensity shows deviation from linearity under laser power of 40 mW (Figure 5.3b). The results indicate that core/shell NCs show strong linear optical properties due to strong quantum confinement effect than CdTe. Threshold energy for the positive deviation of I_{out}/I_{in} is 60 mW for larger size CdTe/CdS NCs. In 4.6 nm- and 5.1 nm-sized CdTe/CdS NCs, the slope of the change of I_{out}/I_{in} is higher than 1. The observed difference in the optical response at low and high laser power indicated a change in the confinement regime. In larger size CdTe/CdS NCs is confinement type is Type II in which the electron-hole is confined into the core and shell individually. The Type II confinement is shown in Figure 4.9. The optical gain is obtained in the smaller size CdTe NCs, on the contrary in CdTe/CdS the gain is achieved in larger size NCs.

When the CdS shell is added, the confinement energy of conduction band electrons decrease as these carriers delocalize throughout the CdTe core and CdS shell. Valence band holes remain confined to the CdTe core due to the large valence band offset between the CdTe and CdS nanocrystals.

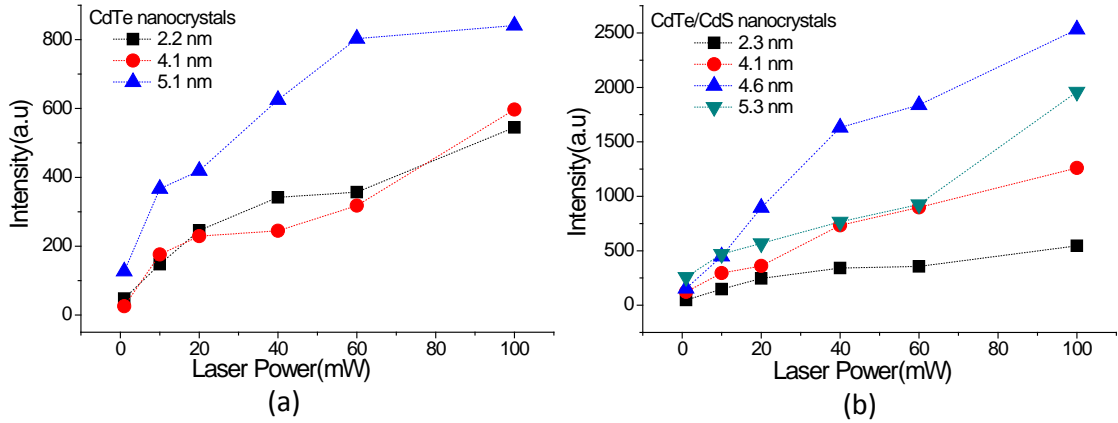


Figure 5.3. The dependence of emission intensity of (a) CdTe and (b) CdTe/CdS nanocrystals on the laser power.

All dynamic phenomena of excitons reflect on the PL spectra. From the PL spectra in Figure 5.4, it can be seen that line width became wide in all NCs. There is no much change in shape of peak of core/shell NCs. For the small size CdTe NCs (2.2 nm and 4.1 nm) PL intensity rather increases after excitation with 60 mW laser power. It is very significant in the PL spectra. As the size of CdTe NCs increases to 5.1 nm, probability of exciton-exciton interaction gets lower due to free wandering of excitons throughout the CdTe nanocrystals. On the contrary, dominant increase is obtained in the bigger size CdTe/CdS core/shell NCs. The NCs having a size of 4.1 and 4.6 nm show similar behavior. But as the size increases from 4.6 to 5.3 nm, the change in PL intensity with laser power is highly pronounced due to the increase in the degree of confinement and the change in the type of confinement.

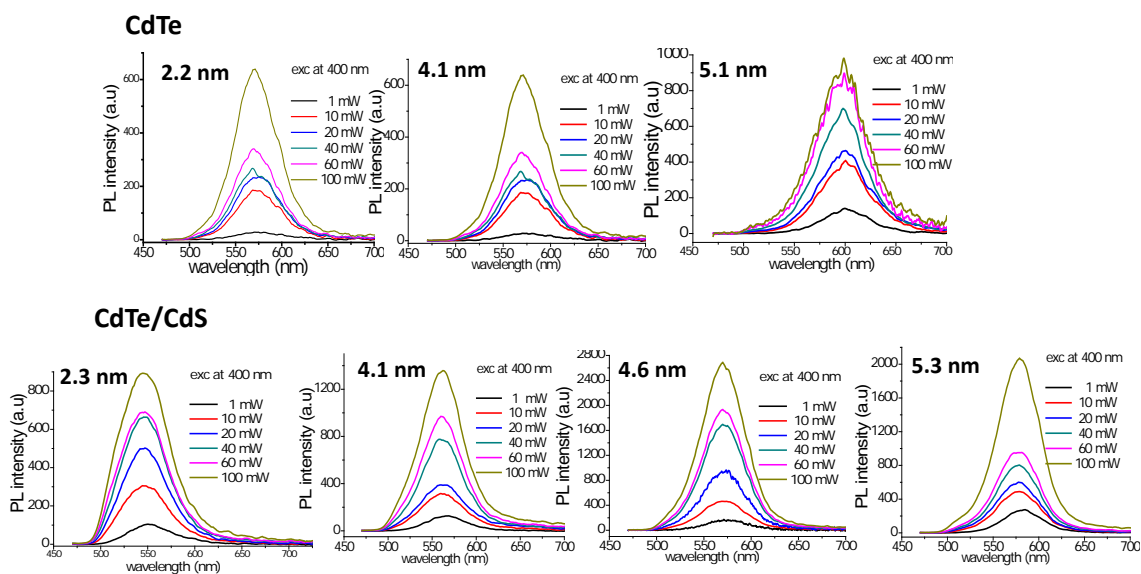


Figure 5.4. The PL emission spectra of different size CdTe core and CdTe/CdS core/shell NCs at initiation time obtained under different laser power, correspondingly from low to high, of 1 to 100mW.

The positions of PL maxima of the NCs show shifting with the laser power. The change in the PL maxima with the laser power is the evidence of exciton-exciton interaction. Figure 5.5 illustrates the change in PL peak position of CdTe core and CdTe/CdS core/shell NCs with the power of laser. Generally, the PL peaks of CdTe NCs shifts to the blue-region. For the small size CdTe NCs, the laser power continuously tunes the PL peak positions (approximately 10 nm shifting) to the lower wavelength and the exciton-exciton interactions are repulsive interactions. As the size of the CdTe NCs gets larger, the tuning was lowered (approximately 5 nm). This is the result of the reduction in confinement of the excitons due to the size effect. The degree of shifting shows that the exciton-exciton interaction is dominant in the smaller size CdTe NCs. The degree of shifting in $Zn_xCd_{1-x}Te$ nanoalloys was higher than 10 nm (Figure 4.11). Exciton-exciton interaction in the $Zn_xCd_{1-x}Te$ nanoalloys is strong compared to CdTe binary NCs.

In the small size CdTe/CdS core/shell NCs, PL maxima continuously shifts to the blue region up to a laser power of 60 mW. On the other hand, in larger size CdTe/CdS core/shell NCs (5.3 nm) the shifting tends to the red region under an excitation of 40 mW laser power. It shows that the exciton-exciton interaction become attractive in the larger size CdTe/CdS NCs under high power of the laser.

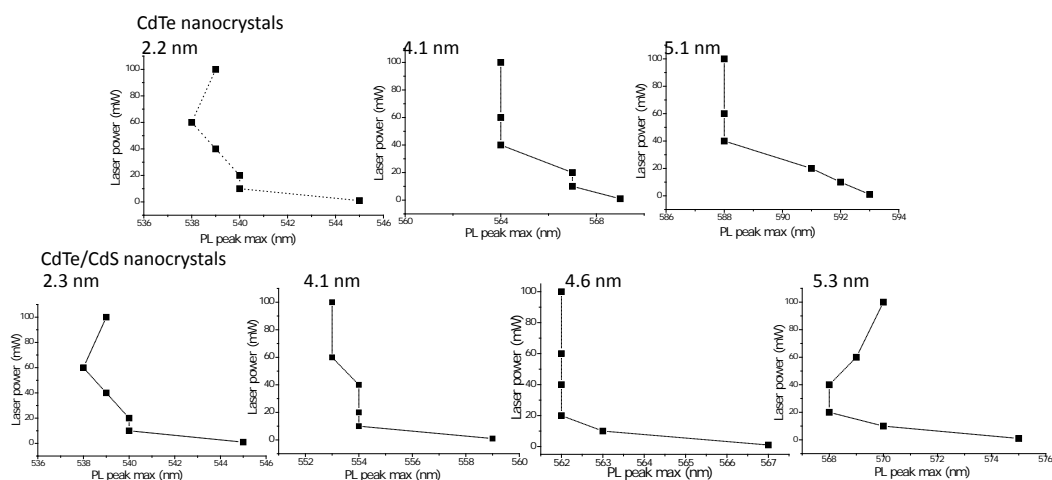


Figure 5.5. The change in PL peak position of CdTe core and CdTe/CdS core/shell NCs with the power of laser correspondingly from low to high, of 1 to 100 mW at initiation time ($t=0$ ps).

The streak images of the CdTe and CdTe/CdS NCs were analyzed globally with Glotran software. The analyses showed that CdTe and CdTe/CdS NCs possess multiexponential decay. Decays are represented by the decay-associated spectra (DAS). The corresponding DAS of CdTe and CdTe/CdS NCs, their contribution, and their spectral positions are similar under excitation of different laser power.

The relaxation dynamics show a fast decay (DAS1) ($\tau_1 < 80$ ps), which is dependent on the laser power, a slow decay (DAS2) ($\tau_2 \sim 400$ -800 ps), and band edge transition (DAS3) ($\tau_3 \sim$ tens of ns). The slow decay is attributed to the electron-hole recombination of surfactant or solvent trapped electrons as suggested literature (Zhang et al. 2003, Wu, and Zhang 2009, Yan et al. 2011). The intensity-dependent, fast decay component is assigned to exciton-exciton annihilation or photoionization / Auger recombination and experimentally it is difficult to distinguish between exciton-exciton annihilation and Auger recombination.

The decay associated spectra of the 2.2 nm-sized CdTe is seen in Figure 5.6 and represent the emission of state with three decay lifetime. Through DAS it was seen that the NCs showed three-exponential decays (3 similar decay processes). Each color in the DAS spectra represents different processes; fastest process (DAS1: black line), fast process (DAS2: red line), and long process (DAS3: blue line). Each individual spectrum represents one-state and one-process. The DAS1 has the highest contribution at each power of the laser for all CdTe and CdTe/CdS NCs. As the laser power increases the

contribution of DAS1 increases with respect to DAS2 and DAS3 and for each laser power DAS2 and DAS3 have similar contribution.

CdTe PL λ_{\max} 557 nm, size 2.2 nm

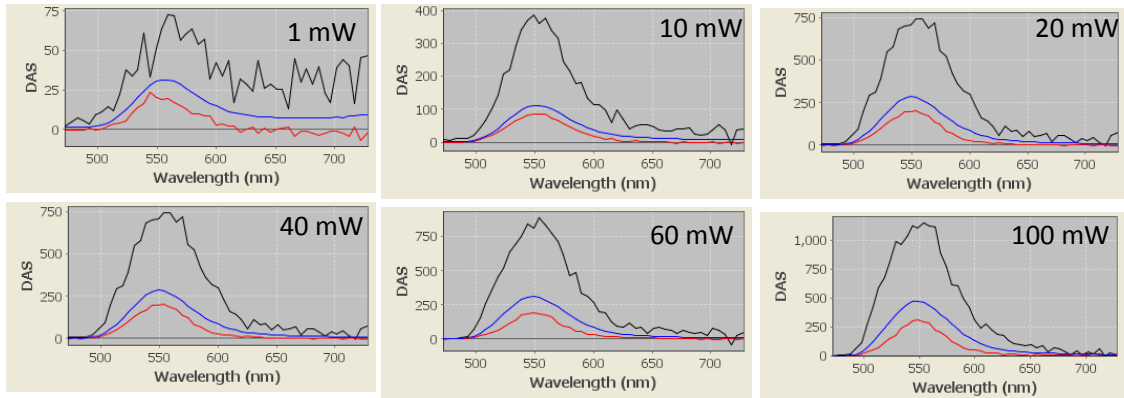


Figure 5.6. Decay-associated spectra of 2.2 nm-sized CdTe nanocrystals under excitation of different laser power obtained by global analysis.

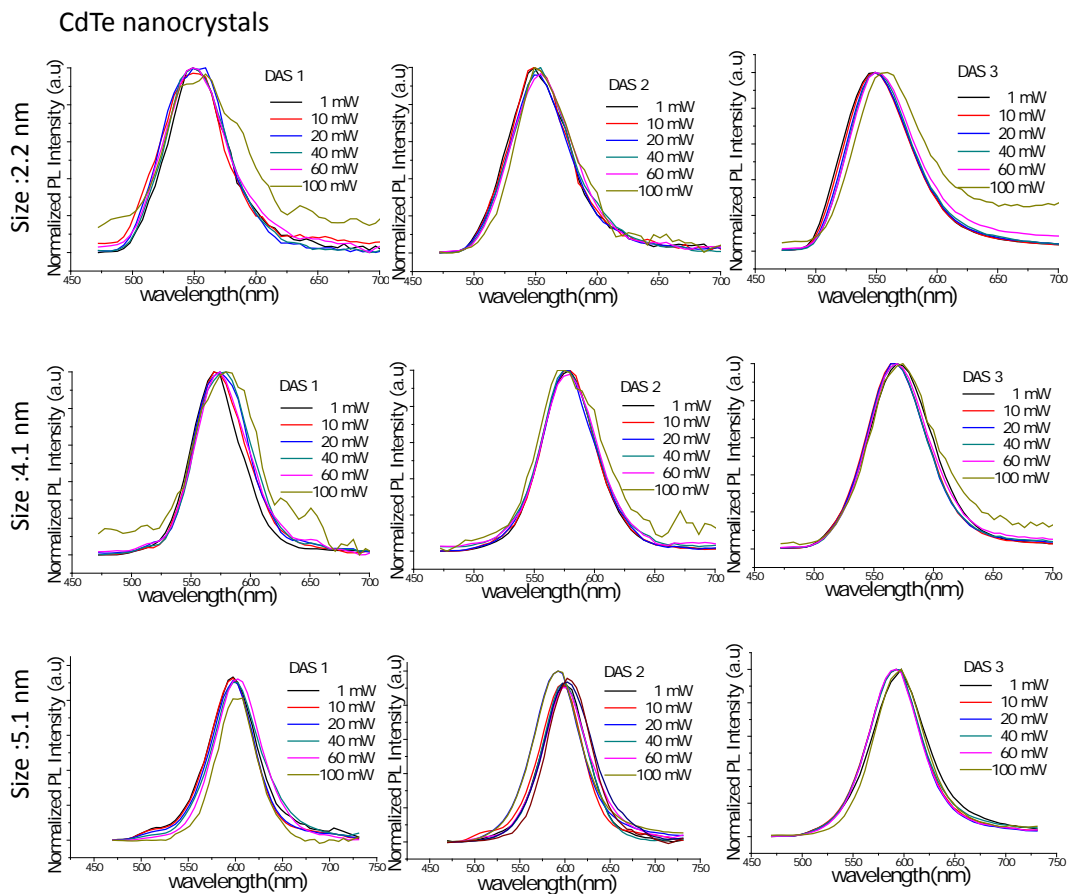


Figure 5.7. Normalized decay-associated spectra of CdTe nanocrystals obtained by global analysis.

CdTe/CdS nanocrystals

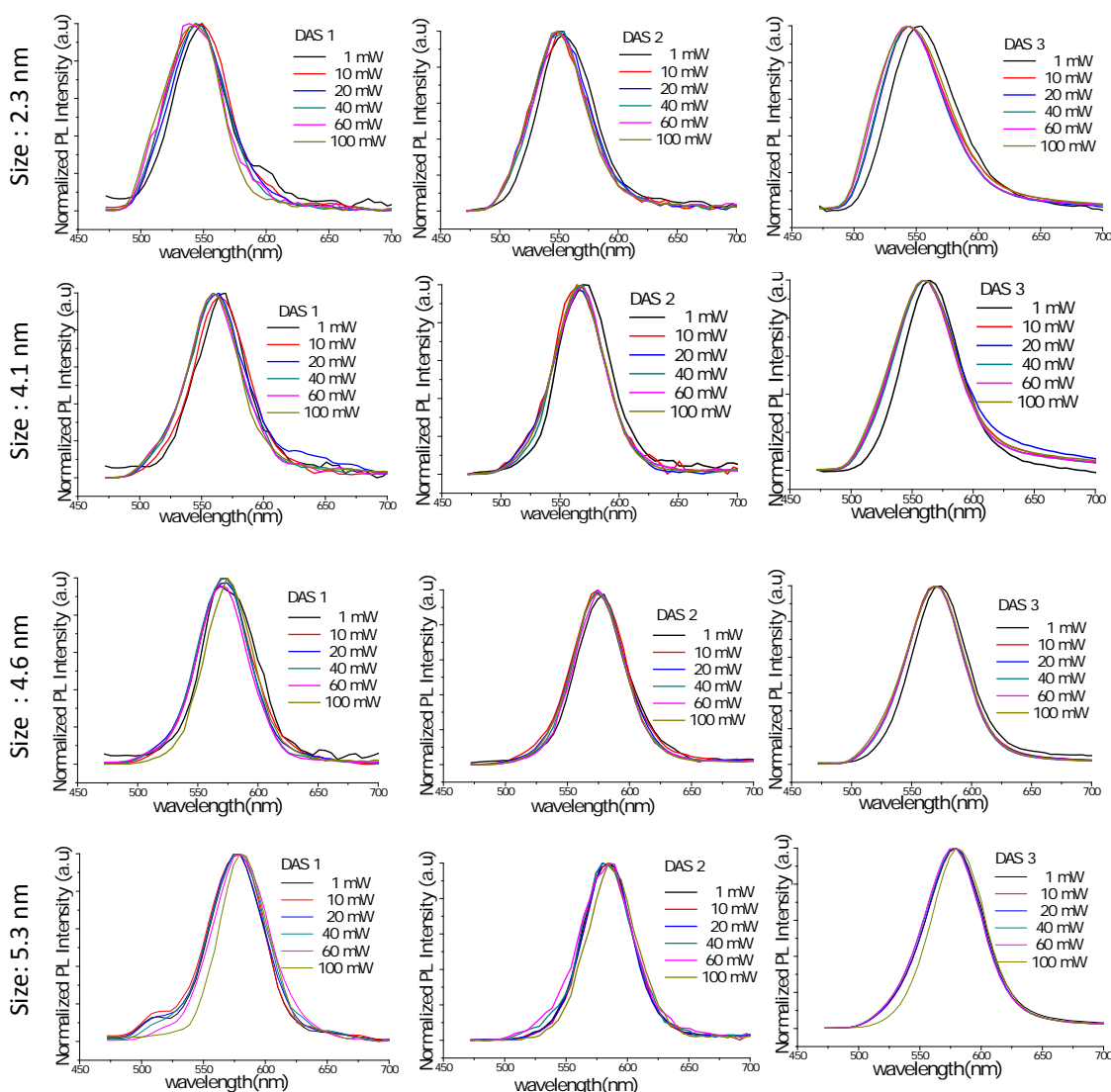


Figure 5.8. Normalized decay-associated spectra of CdTe/CdS nanocrystals obtained by global analysis.

The amplitude of the fast component increases faster than the slower component with the increasing laser power. The power-dependent fast component was then assigned to exciton-exciton annihilation, as suggested previously (Zheng, and Kwok 1994). The slower decays were attributed to trapping and the recombination of trapped carriers. The DAS of the CdTe and CdTe/CdS NCs are size-dependent and represent the emission of state with three decay lifetime. Figure 5.7 and Figure 5.8 shows the DAS of CdTe and CdTe/CdS NCs, respectively. But all DAS have similar Gaussian shape. In all NCs PL peak maxima are at the same position.

The decay associated spectra of the $Zn_xCd_{1-x}Te$ nanoalloys were completely different than those of the CdTe and CdTe/CdS type NCs. The differences indicate that Zn incorporation creates new electronic state for the decay processes and enhance exciton-exciton interaction in nanoalloys compared to binary NCs. The exciton-exciton interaction in the $Zn_xCd_{1-x}Te$ nanoalloys populates two-exciton state and the energy of the state is higher than that of one-exciton state. On the contrary, in the small size CdTe and big size CdTe/CdS nanocrystals, the two-exciton state has same energy with the one-exciton state. That is why the spectral position of the DAS approximately is seen at the same wavelength.

Average decay times for all decay processes and their corresponding amplitudes are listed in Table 5.2. The τ_{av} of the CdTe and CdTe/CdS NCs increases with their size. Coating of the CdTe core with the CdS shell also prolongs the lifetime. The overall relatively slow decay (DAS3) in the NCs except 5.3 nm-sized CdTe/CdS NCs within ns time is consistent with their strong fluorescence and high QY, indicating an efficient radiative relaxation process.

Table 5.2. Average decay lifetime with their respective amplitude of nanocrystals.

NCs(size)	A1 (%)	Average t1(ns)	A2 (%)	Average t2(ns)	A3 (%)	Average t3(ns)	t_{av} (ns)
CdTe (2.2 nm)	10.4	0.03	32.6	0.39	57.0	21.8	21.6
CdTe (4.1 nm)	2.9	0.08	35.4	0.57	61.7	26.84	26.5
CdTe (5.1 nm)	8.2	0.04	55.6	0.79	36.2	39.04	37.9
CdTe /CdS (2.3 nm)	7.5	0.03	35.8	0.40	56.7	36.8	36.5
CdTe /CdS (4.1 nm)	11.7	0.06	38.1	0.51	50.2	49.16	48.8
CdTe /CdS (4.6 nm)	7.5	0.05	38.6	0.47	53.8	64.15	63.8
CdTe /CdS (5.3 nm)	13.6	0.05	52.2	0.45	34.3	58.31	57.6

5.3. Conclusion

Colloidally-synthesized thiol-capped CdTe core, CdTe/CdS core/shell NCs have been analyzed in terms of their exciton relaxation dynamics and exciton-exciton interactions by time-resolved fluorescence spectroscopy using streak camera system. The NCs were excited at 400 nm and laser powers have been changed from 1 to 100

mW. With the laser powers, 100 μm spot size and 400 nm excitation wavelength, the photon fluence are changed from $j_p=3.22 \times 10^{15}$ to 3.2×10^{17} photon/ cm^2s per laser pulse, respectively. The decay signals of the particles show multiexponential behavior. The amplitude and lifetime values of the fast and slow processes were obtained by global analysis method. Time-resolved PL decays both showed exciton lifetimes in the tens of picosecond scale for fast processes and in tens of nanosecond scale for slow ones.

The detected PL signal and obtained DAS are affected by the power of laser, size and composition of the NCs. The changes in PL peak position, band width, and peak shape show that there are multiexciton generation in the NCs. $I_{\text{output}}/I_{\text{input}}$ in the small size CdTe and big size CdTe/CdS NCs is more than 1. Exciton confinement is strong in the small size CdTe, so there are more exciton-exciton interactions. However smaller sized CdTe/CdS NCs have less exciton-exciton interactions compared to small size NCs. On the contrary as the size of the CdTe/CdS NCs increases, the interaction becomes dominant. In CdTe NCs under excitation of high laser power the exciton exciton interaction is repulsive. The interaction is attractive in the larger size CdTe/CdS NCs under high laser power.

As the laser power increases exciton-exciton interaction starts in the NCs. Their decay associated spectra showed the NCs show multiexponential decays. The positions of PL maxima of the NCs show shifting with laser power due to exciton-exciton interaction. CdTe/CdS excitonic life time is longer than that of CdTe and the change in bandwidth of PL peak is not as much as in the CdTe, the CdTe/CdS NCs show Type II confinement regime.

The relaxation dynamics show a fast decay (DAS1) ($\tau_1 < \text{than } 80 \text{ ps}$), which is dependent on the laser power, a slow decay (DAS2) ($\tau_2 \sim 400\text{-}800 \text{ ps}$), and band edge transition (DAS3) ($\tau_3 \sim \text{tens of ns}$). The DAS3 is attributed to the electron-hole recombination. The intensity-dependent, fast decay component (DAS1) is assigned to exciton-exciton annihilation or photoionization / Auger recombination.

CHAPTER 6

CONCLUSION

Thiol capped CdTe core and CdTe/CdS core/shell NCs were preferred to study due to their efficient solubility in water without losing their photostability. They were synthesized successfully by using one-pot approach at relatively low temperature. The synthesis of the CdTe NCs was carried out under N₂ atmosphere in two steps. In order to get NCs of high quality, some optimization studies were performed. During the optimization the ratio of reactants, amount of solvent, pH, and reflux time were changed. It was found that the relative amount of TGA to Cd precursor plays a pivotal role in the quality of synthesis. The mole ratio of TGA to Cd was adjusted to 6.05:3.12 as it was the optimum ratio for synthesizing monodisperse spherical NCs. The pH of the solution was adjusted to 11.0-11.5 because at this pH interval the most possible Cd species have no / less adsorption site onto NCs. Therefore NCs grows monodispersly with high quantum yield. The CdTe core NCs were synthesized in both 55 ml and 110 ml of water. In concentrated (55 ml) medium, the growth of NCs was very fast and the QY of the NCs was very low. The concentration affects the ion diffusion. The NCs synthesized in 110 ml distilled water have QY 25%. To reach certain size NCs, reaction time was prolonged. The absorption and emission peaks of CdTe NCs continuously shifted to higher wavelengths with a prolonged reaction time. The shifts to longer wavelengths are due to quantum confinement. Optimized synthesis provides thiol capped CdTe NCs with bright emission tunable from 520 nm to 640 nm. The NCs show long decay times up to 26.4 ns.

The CdTe core was coated with CdS shell. The coating CdTe by a CdS shell was done by the injection of thiourea to the crude solution of CdTe during the growth. Amount of thiourea was changed relative to amount of Te. The coating enhanced the optical properties of the CdTe NCs. The highest quantum yield of 45% was obtained when the mole ratio of Te:S was 1:10. The excitonic lifetime of CdTe/CdS core/shell NCs is higher than that of CdTe and the core/shell NCs shows up to 79.4 ns PL decay. Thiol-capped NCs are water dispersible and quantized growth of NCs can be achievable by controlling the reaction time. All the NPs are reproducible with high quality.

Accounts on the synthetic chemistry of $Zn_xCd_{1-x}Te$ nanoalloys were very limited and we developed a new way to synthesize highly luminescent colloidal $Zn_xCd_{1-x}Te$ ternary nanoalloy. The one-pot approach was applied at low temperature compared to organometallic-hot injection technique. Ternary thiol-capped $Zn_xCd_{1-x}Te$ nanoalloy have been synthesized by changing the respective mole ratio of metal ($Zn/Zn+Cd$) in precursors from 0.04 to 0.92. During the synthesis total amount of metal precursors was kept constant at 3.12 mmol and the respective mole ratios of Zn/Cd in the precursor mixture were changed. It was modulated from 0.12 to 0.65. The fractions of incorporated Zn in the nanoalloys were verified by ICP-AES. The size and composition tunable optical properties of the $Zn_xCd_{1-x}Te$ nanoalloys were characterized.

The photophysical parameters of the nanoalloys are affected by final mole ratio of Zn^{2+} to Cd^{2+} inside the nanolloy structure. The PL peak positions, the quantum efficiency, and internal structure are affected by the replacement of Zn in Cd position in the crystal. The steady-state spectroscopic analyses of the nanoalloys show that composition-tunable $Zn_xCd_{1-x}Te$ nanoalloys exhibit highly luminescent properties with high quantum yield (up to 53%). The QY of nanoalloys could be improved by coating with CdS shell or by annealing for suitable time. These processes enhanced the QY more than 10%.

Photoluminescence of the nanoalloy is tunable from 520 to 620 nm by either the size or the alloy composition. The size of the nanoalloy is varied from 2.0 ± 0.8 to 9.5 ± 2.4 nm, determined by DLS measurements. DLS measurements showed that the size distribution of the nanoalloys is highly monodisperse and TEM images confirmed the size and size distribution of the nanoalloys. We suggest that the composition of the nanoalloy is modulated by adjusting the amount of metal precursors and the alloying process depends on the reactivity of precursor toward Te anions. The Cd -rich homogeneous nanoalloys are formed when the initial mixture of the metal precursor contains lower amount of Zn . The Zn -rich nanoalloys are formed at high $Zn/Zn+Cd$ mole ratio in the precursor solution. It was noted that the reactions with lower Zn precursors were reproducible and controllable. The nanoalloys obtained from low amount of initial ($Zn/Zn+Cd$) mole ratio have narrow spectral width, (FWHM: 40-55 nm), whereas the nanoalloys synthesized from higher amount of ($Zn/Zn+Cd$) initial mole ratio have wide spectral width, (FWHM: ~ 72 nm). All nanoalloys have zinc blend cubic structure and they have composition- and size- dependent band gap energies.

It is noted that the magnitude of the quantum yield is lowered when the size is increased to 10 nm and number of incorporated Zn is increased, the larger surface area and uncoordinated Zn may introduce surface defects reducing the radiative rate constant which correlates QY values.

Colloidally-synthesized $Zn_xCd_{1-x}Te$ nanoalloys have been analyzed in terms of their exciton relaxation dynamics and exciton-exciton interactions by time-resolved fluorescence spectroscopy using streak camera system. The nanoalloys were excited at 400 nm and laser powers have been changed from 1 to 100 mW. With the laser powers, 100 μm spot size and 400 nm excitation wavelength, the photon fluence are changed from $j_p=3.2 \times 10^{15}$ to 3.2×10^{17} photon/cm²s per laser pulse, respectively. Under the high-power laser excitation multistates formed, multi-transition and multi-processes took place. The decay signals of the nanoalloys showed multiexponential behavior. The amplitude and lifetime values of the fast and slow processes have been obtained by the global analysis method. Time-resolved photoluminescence decays both showed exciton lifetimes in the tens of picoseconds scale for fast processes and in tens of nanosecond scale for slow processes.

The detected PL signal and obtained DAS were affected by the power of laser, size and composition of the nanoalloys. The changes in the PL peak position, the band width, and the peak shape indicated that multiexciton was generated in the $Zn_xCd_{1-x}Te$ nanoalloys under excitation with high laser power. Fluorescence intensity of the nanoalloys increased with the laser power. The increase in the PL intensity was highly dominant when laser power was increased from 80 mW to 100 mW. At 100 mW the output intensity was high. The nanoalloys of smaller sizes (4.5 ± 1.4 nm) have more excitons, so there are more exciton-exciton interactions. However the bigger-sized (9.5 ± 2.4 nm) nanoalloys have less excitons therefore there are less exciton-exciton interactions. The one-exciton-lifetime of the bigger nanoalloys is longer than those of the smaller nanoalloys.

As the laser power increases, the exciton-exciton interaction starts and new exciton energy state forms in $Zn_xCd_{1-x}Te$ nanoalloys. Their DAS showed that the fraction of incorporated Zn diversifies the electronic structure of the nanoalloys and creates new decay pathways. Exciton dynamics are both composition- and size-dependent. The exciton-exciton interaction is repulsive in small nanoalloys and it is highly intense with respect to larger ones. Exciton-exciton interactions in the Zn-rich nanoalloys as reflected in their DAS are more dominant than the Zn-poor nanoalloys.

The change in the shape of the PL peaks and the FWHM proves that $Zn_xCd_{1-x}Te$ nanoalloys have type I confinement regime. The positions of the PL maxima of the nanoalloys showed blue-shifting with the laser power due to the stronger exciton-exciton interactions. For the small size nanoalloys, the laser power continuously tuned the peak positions to the lower wavelength and it showed that the exciton-exciton interactions were repulsive. As the size of the nanoalloys becomes larger, the tuning to the blue region was lowered because the excitons diffuse more freely throughout larger crystals and it reduces the exciton-exciton interactions.

The relaxation dynamics showed a fast decay ($\tau_1 < 50$ ps), which is dependent on excitation intensity, a slow decay ($\tau_2 \sim 400-700$ ps), and band edge transition ($\tau_3 \sim$ tens of ns). The slow decay was attributed to the electron-hole recombination. The intensity-dependent, fast decay component was assigned to exciton-exciton annihilation or photoionization/Auger recombination. It is not easy to distinguish them experimentally.

Colloidally-synthesized thiol-capped CdTe core, CdTe/CdS core/shell NCs have been analyzed in terms of their exciton relaxation dynamics and exciton-exciton interactions by time-resolved fluorescence spectroscopy using streak camera system. The NCs were excited at 400 nm and laser powers have been changed from 1 to 100 mW. With the laser powers of 100 μm spot size and 400 nm excitation wavelength, the photon fluence are changed from $j_p = 3.22 \times 10^{15}$ to 3.2×10^{17} photon/cm²s per laser pulse, respectively. The decay signals of the particles show multiexponential behavior. The amplitude and lifetime values of the fast and slow processes have been obtained by global analysis method. Time-resolved PL decays both showed exciton lifetimes in the tens of ps scale for fast processes and in tens of ns scale for slow processes.

The detected PL signal and obtained DAS are affected by the power of laser, size and composition of the NCs. The changes in PL peak position, band width, and peak shape show that there are multiexciton generation in the NCs. I_{output}/I_{input} in the small size CdTe and big size CdTe/CdS NCs is more than 1. Exciton confinement is strong in the small size CdTe, so there are more exciton-exciton interactions. However smaller sized CdTe/CdS NCs have less exciton-exciton interactions compared to small size NCs. On the contrary as the size of the CdTe/CdS NCs increases, the interaction becomes dominant. In CdTe NCs under excitation of high laser power the exciton exciton interaction is repulsive. The interaction is attractive in the larger size CdTe/CdS NCs under high laser power.

As laser power increases exciton-exciton interaction starts in the NCs. Their DAS showed the NCs show multiexponential decays. The positions of PL maxima of the NCs show shifting with laser power due to exciton-exciton interaction. CdTe/CdS excitonic lifetime is longer than that of CdTe and the change in bandwidth of PL peak is not as much as in the CdTe, the CdTe/CdS NCs show Type II confinement regime.

The relaxation dynamics show a fast decay (DAS1) ($\tau_1 < \text{than } 80 \text{ ps}$), which is dependent on the laser power, a slow decay (DAS2) ($\tau_2 \sim 400\text{-}800 \text{ ps}$), and band edge transition (DAS3) ($\tau_3 \sim \text{tens of ns}$). The DAS3 is linked to the electron-hole recombination. The intensity-dependent, fast-decay component (DAS1) is attributed to exciton-exciton annihilation or photoionization / Auger recombination.

REFERENCES

- Abu Bakar, N., Ali Umar, A., Mat Salleh, M., Yahaya, M., Majlis, B. Y. 2009. " Highly Red Luminescence Properties from Ternary ZnCdTe Quantum Dots." *Second International Conference on Smart Materials and Nanotechnology in Engineering Proc. of SPIE Vol. 7493, 74935W*, CCC code: 0277-786X/09/\$18 · doi: 10.1117/12.839808
- Allen, P. M., and Bawendi, M. G. 2008. "Ternary I-III-VI Quantum Dots luminescent in the red to near-infrared. " *Journal of the American Chemical Society* 130 (29):9240.
- Alivisatos, A. P. 1996. " Semiconductor clusters, NCs, and Quantum Dots." *Science* no. 271 (5251):933-937. doi: 10.1126/science.271.5251.933.
- Alivisatos, A. P. 1999. "Semiconductor Nanocrystals as fluorescent biological labels." *Abstracts of Papers of the American Chemical Society* no. 218:U296-U296.
- Bae, W. K., Char, K., Hur, H., and Lee, S. 2008. "Single-step synthesis of Quantum Dots with chemical composition gradients." *Chemistry of Materials* no. 20 (2):531-539. doi: 10.1021/cm070754d.
- Baierlein, R. 2001. "The elusive chemical potential." *American Journal of Physics* 69 (4):423-434.
- Bailey, R. E. Smith, A. M., Nie, S. 2004. "Review: Quantum dots in biology and medicine." *Physica E* 25, 1–12.
- Bailey, R. E. and Nie, S. 2003. "Alloyed Semiconductor Quantum Dots: Tuning the Optical properties without Changing the Particle Size." *J. Am. Chem. Soc.* 125, 7100-7106.
- Beard, M. C. and Ellingson, R. J. 2008. "Multiple exciton generation in semiconductor Nanocrystals: Toward efficient solar energy conversion." *Laser & Photon. Rev.* 2, No. 5, 377–399.
- Brown, I. D. 1988. "What factors determine cation coordination numbers?" *Acta Cryst.* B44, 545-553, doi:10.1107/S0108768188007712.
- Bruchez, M., Moronne, P. G., Weiss, S., and Alivisatos, A. P. 1998. "Semiconductor Nanocrystals as fluorescent biological labels." *Science* no. 281 (5385):2013-2016. doi: 10.1126/science.281.5385.2013.
- Brumer, M., Kigel, A., Amirav, L., Sashchiuk, A., Solomesch, O., Tessler, N., and Lifshitz, E. 2005. "PbSe/PbS and PbSe/PbSe_xS_{1-x} core/shell Nanoparticles."

- Advanced Functional Materials* no. 15 (7):1111-1116. doi: 10.1002/adfm.200400620.
- Brust, M., Walker, M., Bethell, D., Schiffrin, D. J., and Whyman, R. 1994. "Synthesis of Thiol-Derivatized Gold Nanoparticles in a 2-Phase Liquid-Liquid System." *Journal of the Chemical Society-Chemical Communications* (7):801-802.
- Bullen, C. R.; Mulvaey, P. 2004. "Nucleation and Growth Kinetics of CdSe Nanocrystals in Octadecene." *Nano Lett.* 2004, 4, 2303-2307.
- Califano, M., Franceschetti, A., Zunger, A. 2005. "Temperature dependence of excitonic radiative decay in CdSe quantum dots: the role of surface hole traps." *Nano Letters* 5: 2360–2364
- Cheng, Y., Wang, Y. S., Bao, F., and Chen, D. Q. 2006. "Shape control of monodisperse CdS Nanocrystals: Hexagon and pyramid." *Journal of Physical Chemistry B* no. 110 (19):9448-9451. doi: 10.1021/jp0612073.
- Chin, P. T. K., Donega, C. D. M., Bavel, S. S., Meskers, S. C. J., Sommerdijk, N., and Janssen, R. A. J. 2007. "Highly luminescent CdTe/CdSe colloidal heteronanocrystals with temperature-dependent emission color." *Journal of the American Chemical Society* no. 129 (48):14880-14886. doi: 10.1021/ja0738071.
- Colvin, V. L., Schlamp, M. C., and Alivisatos, A. P. 1994. "Light-Emitting Diodes Made from Cadmium Selenide Nanocrystals and A Semiconducting Polymer." *Nature* no. 370 (6488):354-357. doi: 10.1038/370354a0.
- Dabbousi, B. O., RodriguezViejo, J., Mikulec, F. V., Heine, J. R., Mattoussi, H., Ober, R., Jensen, K.F., and Bawendi, M. G. 1997. "(CdSe)ZnS core-shell Quantum Dots: Synthesis and characterization of a size series of highly luminescent nanocrystallites." *Journal of Physical Chemistry B* no. 101 (46):9463-9475. doi: 10.1021/jp971091y.
- Dagott 2009. Solid State II Instructor: Dr. Dagott An Introduction to Quantum Dots: Confinement, Synthesis, Artificial Atoms and Applications. John Sinclair University of Tennessee. April 9.
- Donega, C. D., Hickey, S. G., Wuister, S. F., Vanmaekelbergh, D., Meijerink, A. 2003. "Single-Step Synthesis to Control the Photoluminescence Quantum Yield and Size Dispersion of CdSe Nanocrystals." *J Phys Chem B*, 107, 489-496.
- Donega, C. D. 2011. "Synthesis and properties of colloidal heteronanocrystals." *Chemical Society Reviews* no. 40 (3):1512-1546. doi: 10.1039/c0cs00055h.
- Efros, Al. L., and Efros, A. L. 1982. "Pioneering Effort." *Sov. Phys. Semicond.* 16: 772.
- Efros, A. L. 1992. "Luminescence Polarization of CdSe." *Phys. Rev. B* 46, 7448-7458.

- Ekimov, A. I., Efros, A. L., Ivanov, M. G., Onushchenko, A. A., and Shumilov, S. K. 1989. "Donor-like Exciton in Zero Dimension Semiconductor Structures." *Solid State Communications* no.69 (5):565-568. doi: 10.1016/0038-1098(89)90242-1.
- Erokhin, V., Carrara, S., Amenitch, H., Bernstorff, S., and Nicolini, C. 1998. "Semiconductor Nanoparticles for quantum devices." *Nanotechnology* no. 9 (3):158-161. doi: 10.1088/0957-4484/9/3/004.
- Farrow, B., and Kamat, P. V. 2009. "CdSe Quantum Dot Sensitized Solar Cells Shuttling Electrons Through Stacked Carbon Nanocups." *Journal of the American Chemical Society* 131 (31):11124-11131.
- Fery-Forgues, S. and Lavabre, D. 1999. "Are Fluorescence Quantum Yields So Tricky to Measure? A Demonstration Using Familiar Stationery Products." *Journal of Chemical Education* no. 76 (9):1260. doi: 10.1021/ed076p1260.
- Feynman, Richard. P. 1960. "There is a plenty room at the bottom." *Journal of Microelectromechanical Systems (1992)* no. 1:60-66.
- Fisher, B., Caruge, J. M., Zehnder, D., Bawendi, M. 2005. "Room-temperature ordered photon emission from multiexciton states in single CdSe core-shell nanocrystals." *Physical Review Letters* 94: 087403.
- Fitzmorris, B. C., Larsen, G. K., Wheeler, D. A., Zhao, Y., and Zhang, J. Z. 2012. "Ultrafast Charge Transfer Dynamics in Polycrystalline CdSe/TiO₂ Nanorods Prepared by Oblique Angle Codeposition." *Journal of Physical Chemistry C* 116 (8):5033-5041.
- Franceschetti, A., and Zunger, A. 1997. "Direct pseudopotential calculation of exciton Coulomb and exchange energies in semiconductor Quantum Dots." *Physical Review Letters* no. 78 (5):915-918. doi: 10.1103/PhysRevLett.78.915.
- Gao, Y. N., Talgorn, E., Aerts, M., Trinh, M. T., Schins, J. M., Houtepen, A. J., and Siebbeles, L. D. A. 2011. "Enhanced Hot-Carrier Cooling and Ultrafast Spectral Diffusion in Strongly Coupled PbSe Quantum-Dot Solids." *Nano Letters* 11 (12):5471-5476.
- Gaponik, N., Talapin, D.V., Rogach, A.L., Hoppe, K., Shevchenko, E. V., Kornowski, A., Eychmüller, A., and Weller, H. 2002. "Thiol-Capping of CdTe Nanocrystals: An Alternative to Organometallic Synthetic Routes." *Journal Physical Chemistry B* 106: 7177-7185.
- Gholami-Kalijia, S., Saievar-Iranizada, E., Dehghania, Z., Majles-Arab M.H. 2011. "Influence of synthesis temperature on linear and nonlinear optical properties of water soluble luminescent Cd_{1-x}Zn_xTe nanocrystals." *Physics Procedia* 19 (2011) 403–407. doi:10.1016/j.phpro.2011.06.182.

- Ghislotti, G., Ielmini, D., Riedo, E., Martinelli, M., Dellagiovanna, M. 1999. "Picosecond time-resolved luminescence studies of recombination processes in CdTe." *Solid State Communications* 111, 211–216.
- Gratzel, M. 1989. In: Serpone, N., Pelizzetti, E. (Eds.), *Photocatalysis: Fundamentals and Applications*. Wiley/ Interscience, New York, pp. 123–157.
- Green, M., and O'Brien, P. 2004. "The synthesis of III-V semiconductor Nanoparticles using indium and gallium diorganophosphides as single-molecular precursors." *Journal of Materials Chemistry* no. 14 (4):629-636. doi: 10.1039/b304000n.
- Gu, Z. Y., Zou, L., Fang, Z., Zhu, W. H., and Zhong, X. H. 2008. "One-pot synthesis of highly luminescent CdTe/CdS core/shell Nanocrystals in aqueous phase." *Nanotechnology* no. 19 (13). doi: 13560410.1088/0957-4484/19/13/135604.
- Henglein, A. 1989. "Small-Particle Research Physicochemical Properties of Extremely Small Colloidal Metal and Semiconductor Particles." *Chemical Reviews* no. 89 (8):1861-1873. doi: 10.1021/cr00098a010.
- Hines, M. A. and Guyot-Sionnest, P. 1996. "Synthesis and characterization of strongly luminescing ZnS-capped CdSe Nanocrystals." *Journal of Physical Chemistry* vol. 100, no. 2, pp. 468– 471.
- Huffaker, D. L., Park, G., Zou, Z., Shchekin, O. B., and Deppe, D. G. 1998. "1.3 μm room-temperature GaAs-based quantum-dot laser." *Applied Physics Letters* no. 73 (18):2564-2566. doi: 10.1063/1.122534.
- Ivanov, S. A., Nanda, J., Piryatinski, A., Achermann, M., Balet, L. P., Bezel, I. V., Anikeeva, P. O., Tretiak, S., Klimov, V. I. 2004. "Light Amplification Using Inverted Core/Shell Nanocrystals: Towards Lasing in the Single-Exciton Regime." *J. Phys. Chem. B* 108, 10625-10630.
- Jamieson, T., Bakhshi, R., Petrova, D., Pocock, R., Imani, M., and Seifalian, A. M. 2007. "Biological applications of Quantum Dots." *Biomaterials* no. 28 (31):4717-4732. doi: 10.1016/j.biomaterials.2007.07.014.
- Jang, E., Jun, S., and Pu, L. 2003. "High quality CdSeS Nanocrystals synthesized by facile single injection process and their electroluminescence." *Chemical Communications* (24):2964-2965. doi: 10.1039/b310853h.
- Jiang, L. and Zhu, Y. J. 2010. "A General Solvothermal Route to the Synthesis of CoTe, Ag₂Te/Ag, and CdTe Nanostructures with Varied Morphologies." *European Journal of Inorganic Chemistry* (8):1238-1243 doi: 10.1002/ejic.200900960.
- Jin, C. Q., Zhong, W., Zhang, X., Deng, Y., Au, C. T., and Du, Y. W. 2009. "Synthesis and Wavelength-Tunable Luminescence Property of Wurtzite Zn_xCd_{1-x}S Nanostructures." *Crystal Growth & Design* no. 9 (11):4602-4606. doi: 10.1021/cg9009724.

- Jones, M., Nedeljkovic, J., Ellingson, R.J., Nozik, A.J., and Rumbles, G. 2003. "Photoenhancement of luminescence in colloidal CdSe quantum dot solutions." *Journal of Physical Chemistry B*, vol. 107, no. 41, pp. 11346–11352.
- Kagan, C. R., Murray, C. B., Nirmal, M., and Bawendi, M. G. 1996. "Electronic energy transfer in CdSe quantum dot solids (vol 76, pg 1517, 1996)." *Physical Review Letters* no. 76 (16):3043-3043. doi: 10.1103/PhysRevLett.76.3043.2.
- Kambhampati, P. 2011. "Hot Exciton Relaxation Dynamics in Semiconductor Quantum Dots: Radiationless Transitions on the Nanoscale." *Journal of Physical Chemistry C* 115 (45):22089-22109.
- Kemling J. W. 2007. Advances in Lasing from Colloidal Quantum Dots Literature Seminar.
- Khatei, J., Pendyala, N. B., and Rao, K.S.R.K. 2011. "Solvothelmal synthesis of Hg_{1-x}Cd_xTe nanostructures-Their structural and optical properties." *Journal of Alloys and Compounds* no. 509 (13):4632-4635. doi: 10.1016/j.jallcom.2011.01.134.
- Kim, S., Fisher, B., Eisler, H.-J., Bawendi, M. G. 2003. "Type-II Quantum Dots: CdTe/CdSe(Core/Shell) and CdSe/ZnTe(Core/Shell) Heterostructures." *J. Am. Chem.Soc.* 125, 11466.
- Kim, M. R., Park, S. Y., and Jang, D. J. 2010. "Composition Variation and Thermal Treatment of Zn_xCd_{1-x}S Alloy Nanoparticles to Exhibit Controlled and Efficient Luminescence." *Journal of Physical Chemistry C* no. 114 (14):6452-6457. doi: 10.1021/jp100834f.
- Klimov, V. I., Mikhailovsky, A. A., Xu, S., Malko, A., Hollingsworth, J. A., Leatherdale, C. A., Eisler, H. J., and Bawendi, M. G. 2000. "Optical gain and stimulated emission in nanocrystal Quantum Dots." *Science* no. 290 (5490):314-317. doi: 10.1126/science.290.5490.314.
- Klimov V 2000. "Optical nonlinearities and ultrafast carrier dynamics in semiconductor nanocrystals." *Journal of Physical Chemistry B* 104: 6112–6123.
- Klimov V.I. 2004. "High-Efficiency Carrier Multiplication in Semiconductor Nanocrystals: Implications for Solar Energy Conversion". *Softmatter Nanotechnology*.
- Klimov, V. I. 2006. "Mechanisms for photogeneration and recombination of multiexcitons in semiconductor Nanocrystals: Implications for lasing and solar energy conversion." *Journal of Physical Chemistry B* 110 (34):16827-16845.
- Klimov, V. I., Ivanov,S. A., Nanda, J., Achermann,M., Bezel,I. , McGuire, J. A., and Piryatinski, A. 2007. "Single-exciton optical gain in semiconductor Nanocrystals." *Nature* 447 (7143):441-446.

- Knowles, K. E., Frederick, M. T., Tice, D. B., Morris-Cohen, A. J., and Weiss, E.A. 2012. "Colloidal Quantum Dots: Think Outside the Particle-in-a-Box." *Journal of Physical Chemistry Letters* 3 (1):18-26.
- Kobayashi, Y., Nishimura, T., Yamaguchi, H., and Tamai, N. 2011. "Effect of Surface Defects on Auger Recombination in Colloidal CdS Quantum Dots." *Journal of Physical Chemistry Letters* 2 (9):1051-1055.
- Kobayashi, Y., Udagawa, T., and Tamai, N. 2009. "Carrier Multiplication in CdTe Quantum Dots by Single-photon Timing Spectroscopy." *Chemistry Letters* Vol.38, No.8.
- Kortan, A. R., Hull, R., Opila, R. L., Bawendi, M. G., Steigerwald, M. L., Carroll, P. J., and Brus, L. E. 1990. "Nucleation and Growth of CdSe on ZnS Quantum Crystallite Seeds, and Vice Versa, In Inverse Micelle Media." *Journal of the American Chemical Society* no. 112 (4):1327-1332. doi: 10.1021/ja00160a005.
- Kraus, R. M., Lagoudakis, P. G., Rogach, A. L., Talapin, D. V., Weller, H., Lupton, J. M., and Feldmann, J. 2007. "Room-temperature exciton storage in elongated semiconductor Nanocrystals." *Physical Review Letters* no. 98 (1). doi: 10.1103/PhysRevLett.98.017401.
- Lakowicz, J. R. 2006. "*Principles of Fluorescence Spectroscopy*" 3rd ed. Vol. 13. New York: Springer Science+Business Media.
- Lee, H., Holloway, P. H., and Yang, H. 2006. "Synthesis and characterization of colloidal ternary ZnCdSe semiconductor nanorods." *Journal of Chemical Physics* no. 125 (16). doi: 10.1063/1.2363181.
- Lesnyak, V., Lutich, A., Gaponik, N., Grabolle, M., Plotnikov, A., Resch-Genger, U., and Eychmuller, A. 2009. "One-pot aqueous synthesis of high quality near infrared emitting Cd_{1-x}Hg_xTe Nanocrystals." *Journal of Materials Chemistry* no. 19 (48):9147-9152. doi: 10.1039/b913200g.
- Lesnyak, V., Plotnikov, A., Gaponik, N., and Eychmuller, A. 2008. "Toward efficient blue-emitting thiol-capped Zn_{1-x}Cd_xSe Nanocrystals." *Journal of Materials Chemistry* no. 18 (42):5142-5146. doi: 10.1039/b811859k.
- Li, W. W., Liu, J., Sun, K., Dou, H. J., and Tao, K. 2010. "Highly fluorescent water soluble Cd_xZn_{1-x}Te alloyed QDs prepared in aqueous solution: one-step synthesis and the alloy effect of Zn." *Journal of Materials Chemistry* no. 20 (11):2133-2138. doi: 10.1039/b921686c.
- Li, Y. C., Ye, M. F., Yang, C. H., Li, X. H., and Li, Y. F. 2005. "Composition- and shape-controlled synthesis and optical properties of Zn_xCd_{1-x}S alloyed Nanocrystals." *Advanced Functional Materials* no. 15 (3):433-441. doi: 10.1002/adfm.200400320.

- Liang, W. Y. 1970. "Physics Education is an international journal, provided by the Institute of Physics (IOP)." *Phys. Educ.* 5 226-228.
- Liu, B. G., He, C. Y., Jin, M. X., Ding, D. J., and Gao, C. X. 2011. "Time-resolved ultrafast carrier dynamics in CdTe Quantum Dots under high pressure." *Physica Status Solidi B-Basic Solid State Physics* no. 248 (5):1102-1105. doi: 10.1002/pssb.201000605.
- Love, J. C., Estroff, L. A., Kriebel, J. K., Nuzzo, R. G., and Whitesides, G. M. 2005. "Self-Assembled Monolayers of Thiolates on Metals as a Form of Nanotechnology." *Chemical Reviews* no. 105 (4):1103-1170. doi: 10.1021/cr0300789.
- Madelung, O. 1996. "Semiconductors-Basic Data " 2nd rev. ed. Springer-Verlag ISBN 3-540-60883-4.
- Maly, P., Trojanek, F., Miyoshi, T., Yamanaka, K., Luterova, K., Pelant, I., and Nemeč, P. 2002. "Ultrafast carrier dynamics in CdSe nanocrystalline films on crystalline silicon substrate." *Thin Solid Films* 403:462-466.
- Mandal, A., and Tamai, N. 2008. "Influence of acid on luminescence properties of thioglycolic acid-capped CdTe quantum dots." *Journal of Physical Chemistry C* 112 (22):8244-8250.
- Manna, L., Milliron, D. J., Meisel, A. E., Scher, C., Alivisatos, A. P. 2003. "Controlled Growth of Tetrapod-branched Inorganic Nanocrystals." *Nature materials* 2, 285.
- Mekis, I., Talapin, D. V., Kornowski, A., Haase, M., Weller, H. 2003. "One-pot synthesis of Highly Luminescent CdSe/ CdS core shell Nanocrystals via Organometallic and 'greener' Chemical Approaches." *Journal of Physical Chemistry B* 107, 7454.
- Miaja-Avila, L., Tritsch, J. R., Wolcott, A., Chan, W. L., Nelson, C. A., and Zhu, X. Y. 2012. "Direct Mapping of Hot-Electron Relaxation and Multiplication Dynamics in PbSe Quantum Dots." *Nano Letters* 12 (3):1588-1591.
- Michalet, X., Pinaud, F. F., Bentolila, L. A., Tsay, J. M., Doose, S., Li, J. J., Sundaresan, G., Wu, M., Gambhir, S. S., and Weiss, S. 2005. "Quantum Dots for live cells, in vivo imaging, and diagnostics." *Science* no. 307 (5709):538-544. doi: 10.1126/science.1104274.
- Murray, C. B., Norris, D. J., and Bawendi, M. G. 1993. "Synthesis and Characterization of Nearly Monodisperse CdE (S = S, Se, Te) Semiconductor Nanocrystallites." *Journal of the American Chemical Society* no. 115 (19):8706-8715. doi: 10.1021/ja00072a025.

- Murray, C. B., Kagan, C. R., and Bawendi, M. G. 1994. "Synthesis and Manipulation of Nearly Monodisperse II-VI Semiconductor Nanocrystallites." *Abstracts of Papers of the American Chemical Society* no. 208:300-Inor.
- Nie, S. M., Xing, Y., Kim, G. J., and Simons, J. W. 2007. "Nanotechnology applications in cancer." *Annual Review of Biomedical Engineering* no. 9:257-288.
- Nonoguchi, Y., Nakashima, T., and Kawai, T. 2007. "Size- and temperature-dependent emission properties of zinc-blende CdTe Nanocrystals in ionic liquid." *Journal of Physical Chemistry C* no. 111 (32):11811-11815. doi: 10.1021/jp073152q.
- Nozik, A. J. 2001. "Spectroscopy and hot electron relaxation dynamics in semiconductor quantum wells and Quantum Dots." *Annual Review of Physical Chemistry* 52:193-231.
- Ouyang, J. Y., Ratcliffe, C. I., Kingston, D., Wilkinson, B., Kuijper, J., Wu, X. H., Ripmeester, J. A., and Yu, K. 2008. "Gradiently alloyed $Zn_xCd_{1-x}S$ colloidal photoluminescent Quantum Dots synthesized via a noninjection one-pot approach." *Journal of Physical Chemistry C* no. 112 (13):4908-4919. doi: 10.1021/jp710852q.
- Pan, D. C., Jiang, S. C., An, L. J., and Jiang, B. Z. 2004. "Controllable synthesis of highly luminescent and monodisperse CdS Nanocrystals by a two-phase approach under mild conditions." *Advanced Materials* no. 16 (12):982-+. doi: 10.1002/adma.200400010.
- Pan, D. C., Wang, Q., Pang, J. B., Jiang, S. C., Ji, X. L. and An, L. J. 2006. "Semiconductor "nano-onions" with multifold alternating CdS/CdSe or CdSe/CdS structure." *Chemistry of Materials* no. 18 (18):4253-4258. doi: 10.1021/cm0601032.
- Pan, D. C., Wang, Q., Jiang, S. C., Ji, X. L., and An, L. J. 2007. "Low-temperature synthesis of oil-soluble CdSe, CdS, and CdSe/CdS core - Shell Nanocrystals by using various water-soluble anion precursors." *Journal of Physical Chemistry C* no. 111 (15):5661-5666. doi: 10.1021/jp0678047.
- Peng, H., Zhang, L., Soeller, J. C., and Travas-Sejdic, J. 2007. "Preparation of water-soluble CdTe/CdS core/shell Quantum Dots with enhanced photostability." *Journal of Luminescence* no. 127 (2):721-726. doi: 10.1016/j.jlumin. 2007. 04. 007.
- Pelouch, W. S., Ellingson, R. J., Powers, P. E., Tang, C. L., Szmyd, D. M., and Nozik, A. J. 1992. "Comparison of Hot-Carrier Relaxation In Quantum-Wells and Bulk GaAs at High Carrier Densities." *Physical Review B* 45 (3):1450-1453.
- Pesika, N. S., Stebe, K. J., and Searson, P. C.. 2003. "Relationship between absorbance spectra and particle size distributions for quantum-sized nanocrystals." *Journal of Physical Chemistry B* 107 (38):10412-10415.

- Qian, H., Dong, C., Peng, J., Qiu, X., Xu, Y. and Ren, J. 2007. "High-quality and water-soluble near-infrared photoluminescent CdHgTe/CdS Quantum Dots prepared by adjusting size and composition." *Journal of Physical Chemistry C* no. 111 (45):16852-16857. doi: 10.1021/jp074961c.
- Rajesh, C A., Lad, D., Ghangrekar, A., Mahamunia, S. 2008. "Exciton recombination dynamics in zinc selenide quantum dots." *Solid State Communications* 148, 435-439.
- Ramsden, J. J. and Grätzel, M. 1984. "Photoluminescence of small cadmium sulphide particles." *J. Chem. Soc., Faraday Trans. I*, 80, No. 14, 919-933.
- Rawalekar, S., Kaniyankandy, S., Verma, S., and Ghosh, H. N. 2010. "Ultrafast Charge Carrier Relaxation and Charge Transfer Dynamics of CdTe/CdS Core-Shell Quantum Dots as Studied by Femtosecond Transient Absorption Spectroscopy." *Journal of Physical Chemistry C* 114 (3):1460-1466.
- Regulacio, M. D., and Han, M. Y. 2010. "Composition-Tunable Alloyed Semiconductor Nanocrystals." *Accounts of Chemical Research* no. 43 (5):621-630. doi: 10.1021/ar900242r.
- Reiss, P., Carayon, S., Bleuse, J., and Pron, A. 2003. "Low polydispersity core/shell Nanocrystals of CdSe/ZnSe and CdSe/ZnSe/ZnS type: preparation and optical studies." *Synthetic Metals* no. 139 (3):649-652. doi: 10.1016/s0379-6779(03)00335-7.
- Rogach, A. L., Franzl, T., Klar, T. A., Feldmann, J., Gaponik, N., Lesnyak, V., Shavel, A., Eychmuller, A., Rakovich, Y.P., and Donegan, J. F. 2007. "Aqueous synthesis of thiol-capped CdTe Nanocrystals: State-of-the-art." *Journal of Physical Chemistry C* no. 111 (40):14628-14637. doi: 10.1021/jp072463y.
- Rozale, H., Lazreg, A., Chahed, A., and Ruterana, P. 2009. "Structural, electronic and optical properties of the wide-gap $Zn_{1-x}Cd_xTe$ ternary alloys." *Superlattices and Microstructures* no. 46 (4):554-562. doi: 10.1016/j.spmi.2009.07.026.
- Saba, M., Minniberger, S., Quochi, F., Roither, J., Marceddu, M., Gocalinska, A., Kovalenko, M. V., Talapin, D. V., Heiss, W., Mura, A., and Bongiovanni, G. 2009. "Exciton-Exciton Interaction and Optical Gain in Colloidal CdSe/CdS Dot/Rod Nanocrystals." *Advanced Materials* 21 (48):4942.
- Sadhu, S., and Patra, A. 2008. "Synthesis and spectroscopic study of high quality alloy $Cd_xZn_{1-x}S$ Nanocrystals." *Journal of Chemical Sciences* no. 120 (6):557-564. doi: 10.1007/s12039-008-0085-1.
- Sarkar, R., Shaw, A. K., Narayanan, S. S., Rothe, C., Hintschich, S., Monkman, A. and Pal, S. K. 2007. "Size and shape-dependent electron-hole relaxation dynamics in US Nanocrystals." *Optical Materials* no. 29 (11):1310-1320. doi: 10.1016/j.optmat.2006.06.006.

- Schaller, R. D., Pietryga, J. M., and Klimov, V. I. 2007. "Carrier multiplication in InAs nanocrystal Quantum Dots with an onset defined by the energy conservation limit." *Nano Letters* 7 (11):3469-3476.
- Scotognella, F., Miszta, K., Dorfs, D., Zavelani-Rossi, M., Brescia, R., Marras, S., Manna, L., Lanzani, G., and Tassone, F. 2011. "Ultrafast Exciton Dynamics in Colloidal CdSe/CdS Octapod Shaped Nanocrystals." *Journal of Physical Chemistry C* 115 (18):9005-9011.
- Sharma, S. N., Sharma, H., Singh, S., Mehra, R. M., Singh, G., and Shivaprasad, S. M. 2010. "Single pot synthesis of composition tunable CdSe-ZnSe (core-shell) and $Zn_xCd_{1-x}Se$ (ternary alloy) Nanocrystals with high luminescence and stability." *Materials Research Innovations* no. 14 (1):62-67. doi: 10.1179/143307510x12599329343286.
- Shieh, F., Saunders, A. E., and Korgel, B. A. 2005. "General Shape Control of Colloidal CdS, CdSe, CdTe Quantum Rods and Quantum Rod Heterostructures." *Phys. Chem. B* 2 109, 8538.
- Song, R., Liu, Y., and He, L. H. 2008. "Synthesis and characterization of mercaptoacetic acid-modified ZnO nanoparticles." *Solid State Sciences* 10 (11):1563-1567.
- Song, L. X., Duan, J. L., and Zhan, J. H. 2010. "One-pot Microwave Assisted Synthesis of Homogeneously Alloyed $CdSe_xTe_{1-x}$ Nanocrystals with Tunable Photoluminescence." *Materials Letters* no. 64 (16):1843-1845. doi: 10.1016/j.matlet.2010.05.015.
- Steigerwald, M. L., and Sprinkle, C. R. 1987. "Organometallic Synthesis of II-VI Semiconductors .1. Formation and Decomposition of Bis(organotelluro) Mercury and Bis(organotelluro) Cadmium Compounds." *Journal of the American Chemical Society* no. 109 (23):7200-7201. doi: 10.1021/ja00257a055.
- Streetman, Ben G., Banerjee, S. 2000. *Solid State electronic Devices* 5th ed. New Jersey: Prentice Hall. p. 524. ISBN 0-13-025538-6
- Stroyuk, A.L., Kryukov, A.I. S., Kuchmii, Y., and Pokhodenko, V. D. 2005. "Quantum Size Effects In The Photonics Of Semiconductor Nanoparticles." *Theoretical and Experimental Chemistry*, Vol. 41, No. 2.
- Talpin, D. V., Mekis, I., Gotzinger, S., Kornowski, A., Benson, O., and Weller, H. 2004. "CdSe/CdS/ZnS and CdSe/ZnSe/ZnS core-shell-shell Nanocrystals." *Journal of Physical Chemistry B* no. 108 (49):18826-18831. doi: 10.1021/jp046481g.
- Tit, N., Obaidat, I. M., and Alawadhi, H. 2009. "Absence of the bowing character in the common-anion II-VI ternary alloys." *Journal of Alloys and Compounds* 481 (1-2):340-344.

- Trindade, T., O'Brien, P., and Pickett, N. L. 2001. "Nanocrystalline semiconductors: Synthesis, properties, and perspectives." *Chemistry of Materials* no. 13 (11):3843-3858. doi: 10.1021/cm000843p.
- Viswanatha, R., Sapra, S., Saha-Dasgupta, T., and Sarma, D.D. 2005. "Electronic structure of and quantum size effect in III-V and II-VI semiconducting Nanocrystals using a realistic tight binding approach." *Physical Review B* 72 (4).
- Viale Y., Gilliot, P., Cre'gut, O., Likforman, J. P., Ho'nerlage, B., Levy, R., Besombes L., Marshal, L., Kheng, K., Mariette, H. 2003. "Excitonic dynamics in CdTe/ZnTe quantum dots." *Materials Science and Engineering*, B101, 55-59.
- Wang, Q., Pan, D.C., Jiang, S.C., Ji, X.L., An, L.J., and Jiang, B.Z. 2006. "A solvothermal route to size- and shape-controlled CdSe and CdTe Nanocrystals." *Journal of Crystal Growth* no. 286 (1):83-90. doi: 10.1016/j.jcrysgr.2005.05.083.
- Wang, Y., Hou, Y. B., Tang, A., Feng, B., Li, Y., Liu, J., and Teng, F. 2007. "Synthesis and optical properties of composition-tunable and water-soluble $Zn_xCd_{1-x}Te$ alloyed Nanocrystals." *Journal of Crystal Growth* no. 308 (1):19-25. doi: 10.1016/j.jcrysgr.2007.07.045.
- Wang, X.F., Xie, P.B., Zhao, F.L., and Wang, H.Z. 2009. "Time-Resolved Photoluminescence of Stimulated Emission from ZnO Nanoparticles." *Spectroscopy and Spectral Analysis* 29 (6):1459-1462.
- Wu, X. C., Wang, R. Y., Zou, B. S., Wu, P. F., Wang, L., Xu, J. R., and Huang, W. 1997. "The effects of different interfacial environments on the optical nonlinearity of nanometer-sized CdO organosol." *Applied Physics Letters* no. 71 (15):2097-2099. doi: 10.1063/1.120424.
- Wu, F., Zhang J. Z. 2009. "Charge Carrier Dynamics of Nanoparticles." Department of Chemistry and Biochemistry, University of California–Santa Cruz, Santa Cruz, California, U.S.A. , 804-818, Taylor & Francis Group, LLC.
- Xu, S. H., Wang, C. L., Xu, Q. Y., Zhang, H. S., Li, R. Q., Shao, H. B., Lei, W., and Cui, Y. P. 2010. "Key Roles of Solution pH and Ligands in the Synthesis of Aqueous ZnTe Nanocrystals." *Chemistry of Materials* no. 22 (21):5838-5844. doi: 10.1021/cm101844j.
- van Stokkum, I. H. M., van Oort, B., van Mourik, F. Gobets, B. and van Amerongen, H. 2008. "(Sub)-Picosecond Spectral Evolution of Fluorescence Studied with a Synchroscan Streak-Camera System and Target Analysis." Thijs J. Aartsma and Jörg Matysik (eds): *Biophysical Techniques in Photosynthesis II*, pp. 223–240. Springer.

- Yagi, I., Mikami, K., Ebina, K., Okamura, M., and Uosaki, K. 2006. "Size-dependent carrier dynamics in CdS Nanoparticles by femtosecond visible-pump/IR-probe measurements." *Journal of Physical Chemistry B* no. 110 (29):14192-14197. doi: 10.1021/jp061073t.
- Yan, Y., Chen, G., and Van Patten, P. G. 2011. "Ultrafast Exciton Dynamics in CdTe NCs and Core/Shell CdTe/CdS Nanocrystals." *Journal of Physical Chemistry C* 115 (46):22717-22728.
- Yin, S., Huang, F., Zhang, J., Zheng, J., and Lin, Z. 2011. "The Effects of Particle Concentration and Surface Charge on the Oriented Attachment Growth Kinetics of CdTe Nanocrystals in H₂O." *J.Phys.Chem.C* 115:10357–10364.
- Yuan, Z., Yang, P., and Cao, Y. 2012. "Time-Resolved PL Spectroscopy Evaluation of CdTe and CdTe/CdS Quantum Dots." *International Scholarly Research Network ISRN Spectroscopy*, Volume 2012, Article ID 894385, 8 pages, doi:10.5402/2012/894385
- Zheng, J.P., Kwok, H.S. 1994. "Exciton and biexciton recombination in semiconductor nanocrystals." *Appl. Phys. Lett.* 65 (9), 1151–1153.
- Zhang, H., Zhou, Z., Yang, B., and Gao, M. Y. 2003. "The influence of carboxyl groups on the photoluminescence of mercaptocarboxylic acid-stabilized CdTe Nanoparticles." *Journal of Physical Chemistry B* no. 107 (1):8-13. doi: 10.1021/jp025910c.
- Zhang, J. Z. 1997. "Ultrafast studies of electron dynamics in semiconductor and metal colloidal Nanoparticles: Effects of size and surface." *Accounts of Chemical Research* no. 30 (10):423-429. doi: 10.1021/ar960178j.
- Zhong, H., Nagy, M., Jones, M., and Scholes, G. D. 2009. "Electronic States and Exciton Fine Structure in Colloidal CdTe Nanocrystals." *Journal of Physical Chemistry C* no. 113 (24):10465-10470. doi: 10.1021/jp901995c.
- Zhong, X. H., Feng, Y.Y., Knoll, W., and Han, M.Y. 2003. "Alloyed Zn_xCd_{1-x}S Nanocrystals with highly narrow luminescence spectral width." *Journal of the American Chemical Society* no. 125 (44):13559-13563. doi: 10.1021/ja036683a.
- Zhong, X. H., Han, M.Y., Dong, Z. L., White, T. J., and Knoll, W.. 2003. "Composition-tunable Zn_xCd_{1-x}Se Nanocrystals with high luminescence and stability." *Journal of the American Chemical Society* no. 125 (28):8589-8594. doi: 10.1021/ja035096m.

Leyla ERAL DOĞAN

Date of Birth: 03 September 1977

Place of Birth: Karabük / Turkey

Citizenship: Turkish

Education :

İzmir Institute of Technology, İzmir, TR

PhD, Faculty of Science, Department of Chemistry, (2006-2012)

Thesis: Synthesis and Control of Exciton Dynamics in CdTe, CdTe/CdS and Zn_xCd_{1-x}Te Colloidal Nanocrystals

İzmir Institute of Technology, İzmir, TR

MSc, Faculty of Science, Department of Chemistry, (2003-2006)

Thesis: Hydrothermal Synthesis and Characterization of Transition Metal (Mn and V) Oxides Containing Phosphates

Middle East Technical University, Ankara, TR

BSc, Faculty of Arts and Science, Department of Chemistry, (1994-1999)

Conferences:

“Exciton Relaxation Dynamics in Alloyed Zn_{1-x}Cd_xTe Quantum Dots” The 8th National Conference on Nanoscience and Nanotechnology, Ankara, June 2012.

“Synthesis of Zn_xCd_{1-x}S Alloy Nanocrystals and Their Composition Tunable Spectroscopic Properties” The 7th National Conference on Nanoscience and Nanotechnology, İstanbul, June 2011.

“Composition Tunable Spectroscopic Properties of Zn_xCd_{1-x}Te Ternary Colloidal Quantum Dots” The 6th National Conference on Nanoscience and Nanotechnology, İzmir, June 2010.

“Conjugation of Thioglycolic Acid (TGA) Capped CdTe/CdS Water Dispersible Quantum Dot (QD) with Anti-c-erbB2 for Targeted Cell Imaging” 7th Aegean Analytical Chemistry Days, Izmir, September 2012.

“Synthesis of High-Quality Water Soluble CdTe and CdTe/CdS Nanocrystals” The 5th National Conference on Nanoscience and Nanotechnology, Eskisehir, 2009.

“Synthesis and Characterization of Colloidal NIR-Emitting HgCdTe Nanoparticles” The 8th National Conference on Nanoscience and Nanotechnology, Ankara, June 2012.

“Synthesis and characterization of Gd doped CdTe nanoparticles” The 8th National Conference on Nanoscience and Nanotechnology, Ankara, June 2012.

“Hydrothermal Synthesis and Structure Characterization of Strontium Manganese Phosphate (Sr₂MnP₃O₁₁)” XIXth National Chemistry Conferences, Kusadası, 2005

Publications:

“Crystal Structure of Divalentmanganese(III)tetraoxophosphateheptaoxidiphosphate, Sr₂Mn[PO₄][P₂O₇].” Leyla Dogan & Mehtap Emirdag Eanes. Z. Kristallogr. NCS 222.